UNIVERSITY OF OKLAHOMA

GRADUATE COLLEGE

INVESTIGATION OF APERTURE LEVEL SPATIAL AND FREQUENCY FILTERING ON RADAR AND COMMUNICATION SYSTEM PERFORMANCE

A THESIS

SUBMITTED TO THE GRADUATE FACULTY

in partial fulfillment of the requirements for the

Degree of

MASTER OF SCIENCE

By

MARIEL AVALOS ALVARADO
Norman, Oklahoma
2024

INVESTIGATION OF APERTURE LEVEL SPATIAL AND FREQUENCY FILTERING ON RADAR AND COMMUNICATION SYSTEM PERFORMANCE

A THESIS APPROVED FOR THE
SCHOOL OF ELECTRICAL AND COMPUTER ENGINEERING

BY THE COMMITTEE CONSISTING OF

Dr. Jessica Ruyle

Dr. Justin Metcalf

Dr. Nathan Goodman

Acknowledgments

First and foremost, I would like to express my deepest gratitude to my academic advisor, Dr. Jessica Ruyle, for her invaluable guidance, expertise, and unwavering support. Beyond being an exceptional mentor, Dr. Ruyle is an extraordinary person whose kindness and dedication have not only shaped my growth as a researcher but also made this journey an immensely fulfilling experience. I am especially grateful for the opportunities you have helped me access and for all the lessons you have taught me to grow as a professional.

I would also like to acknowledge the support of my research team, whose collaboration and insights have been essential for the completion of this project. Especially to Rosalind Agasti, who trusted me with her reconfigurable antennas and has been a great support and friend. And, to Adrian Bauer, for helping me with the far-field chamber and the antenna characterization process. Although they were not part of our research group, I would like to thank Shane Flandermeyer and Rylee Mattingly, who generously allowed me access to their equipment and helped me with their expertise throughout the research process.

I am forever thankful for the unconditional support of my family. To my mom, Pilar Alvarado, and my brothers, Alex and Andre Rodriguez, your belief in me has been a source of constant strength, and I could not have come this far without it. I would also like to thank Khuda Burdi for being my rock and best friend throughout this journey. Your constant support, especially during moments of self-doubt, helped me stay grounded and focused. I am incredibly grateful to have had all of you by my side through every challenge.

Finally, to my friends, here and back in Peru, thank you for your encouragement, laughter,

and the much-needed moments of relaxation. Your friendship has consistently reminded me of the value of maintaining balance and finding joy in the midst of hard work. This thesis would not have been possible without the collective support of all these incredible people, to whom I will be forever grateful.

Table of Contents

List of Figures

List of Tables

Abstract

Dynamic spectrum access (DSA) and cognitive radio (CR) systems, built on software-defined radio (SDR) platforms, enable adaptive spectrum use and reconfiguration. Reconfigurable and filtering antennas play a crucial role in DSA, reducing the need for extra filtering circuits and rejecting out-of-band (OOB) signals. However, a comprehensive analysis of their role in SDR-based DSA system performance is yet to be conducted. This work introduces a novel SDR-based test system emulating frequency-variant interference, evaluating traditional broadband, reconfigurable, and filtering antennas by measuring received interference power and signal-to-interference plus noise ratio (SINR) in congested environments. The study shows that reconfigurable filtering antennas enhance OOB interference rejection and offer superior performance in size, weight, and power (SWaP) constrained environments, highlighting their potential for improved system-level performance in congested spectrum scenarios.

Chapter 1

Introduction

As wireless communication systems continue to evolve, the demand for efficient and flexible use of the radio frequency (RF) spectrum has grown significantly. Antennas are key factors in wireless system performance, and as such, their effect on emerging technologies aimed at optimizing spectrum utilization should be analyzed. For instance, reconfigurable antennas and software-defined radio (SDR) platforms are key enablers of dynamic spectrum access (DSA) solutions. However, a comprehensive analysis of their combined performance has yet to be conducted. This chapter presents an overview of the role antennas play in RF systems, introduces the concept of DSA technologies, and reviews the current literature on the impact of reconfigurable antennas on system performance. The chapter concludes with an outline of the thesis structure.

1.1 Antennas in Radio Frequency (RF) Systems

Antennas play a crucial role in wireless communication systems, converting signals bounded within a circuit into propagating electromagnetic (EM) waves and vice versa [1]. The ability of antennas to focus power in a particular region of space and to receive or transmit such power within a certain frequency range makes them the first filtering stage of the system in both the spatial and frequency domains. Therefore, selecting the appropriate antenna according to available radio frequency front-end (RFFE) components and system applications is a complex task and a critical step in any wireless system-level design.

The operational requirements of an antenna in the spatial and frequency domains can vary drastically based on the system's specific application. For example, consider a simple wireless communication system and a weather radar system. Antennas for communication systems usually require low spatial filtering to ensure continuous connectivity between base stations and end-users. These antennas are often classified as *omnidirectional*, meaning they radiate and receive equally in all directions within a given plane [2]. In contrast, weather radar applications require high spatial resolution to accurately classify and track hydrometeors. Therefore, weather radar antennas are directional and often classified as *pencil beam* antennas with strict co-polarized beam matching and cross-polarization level requirements [3]. Pencil beam antennas focus most of the power in a small volume of space, attenuating signals received from all other directions. Fig. 1.1 illustrates how these requirements translate to the antenna's radiation pattern, providing a graphic representation of the spatial filtering concept.

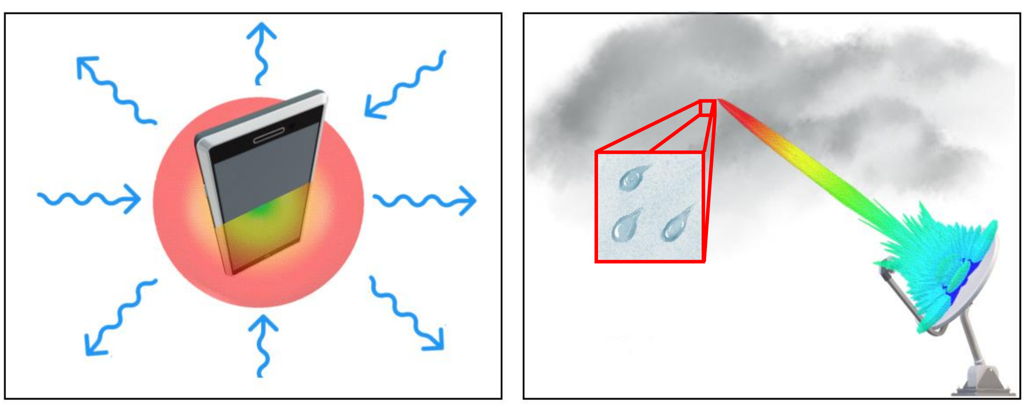

(a) (b)

Figure 1.1: Comparison of radiation pattern characteristics based on spatial filtering requirements for (a) an omnidirectional antenna used in communication systems with low spatial filtering, and (b) a pencil beam antenna used in weather radar applications where high spatial filtering is required. The 3D models used in this figure are from Microsoft PowerPoint.

In the frequency domain, antenna requirements depend on the information to be transmitted rather than the direction of transmission. To transmit useful information over large distances, most RF wireless systems use some form of modulation, which allows the signal to have information embedded in parameters like frequency or phase. This signal is generated in what is called *baseband*. Baseband signals are usually low frequency and are not optimal for transmission, since such a low frequency will require very large antennas [4]. Therefore, before over-the-air transmission, the modulated signal is upconverted to a desired carrier frequency and amplified.

Consequently, the antenna's operating frequency must match that carrier frequency, and its bandwidth must be sufficient for the modulated signal. Ideally, signals outside the desired bandwidth should be attenuated by the antenna. However, since the antenna's impedance matching alone is not enough to reject out-of-band signals, most wireless communication systems use broadband antennas followed by filter banks [5]. In recent decades, reconfigurable filters, reconfigurable antennas, and filtering antennas have been proposed as alternative solutions and will be further discussed in Chapter 2. Reconfigurable architectures offer enhanced adaptability, allowing both antennas and filters to dynamically adjust to changing environment conditions [6]. This adaptability improves interference rejection and provides more efficient spectrum use, ultimately enhancing the overall performance and flexibility of wireless systems.

An example of a block diagram for a radar or communication system receiver is shown in Fig. 1.2. Its main objective is to receive, filter, and amplify the signal at the carrier frequency, and then downconvert its components to baseband for further digital signal processing [7]. Both downconversion and upconversion processes can be performed in multiple stages, generating an *intermediate* frequency. The receiver hardware in an RF system may consist of antennas, low-noise amplifiers (LNAs), mixers, local oscillators (LOs), and filters like band-pass filters (BPFs).

RFFE refers to all the components involved in the carrier signal reception, considering the antenna as the system aperture level. The BPF and LNA right after the antenna can exchange positions depending on the system's environment and priorities. For example, in a high-gain interference environment, it is preferable to place the filter directly after the antenna, whereas in a low signal-to-noise ratio (SNR) environment, amplification is desired first. Additionally, according to the system's adaptability requirements, some RFFE components must be tunable. Note that Fig. 1.2 represents a traditional RF receiver, but depending on the platform available to implement the system, the receiver could require more or fewer hardware components.

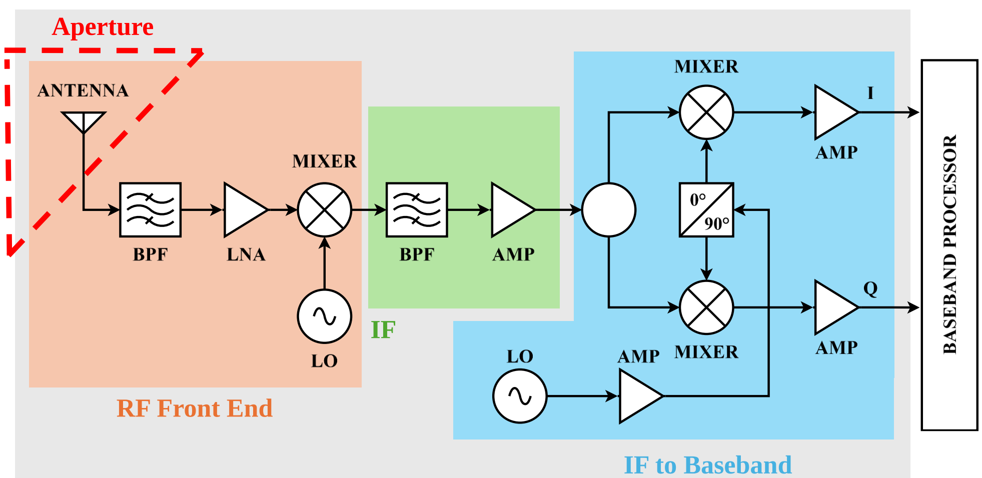

Figure 1.2: Example of a receiver chain block diagram based on a superheterodyne receiver for wireless communications. Adapted from [7].

Additionally, all system components must meet size, weight, and power (SWaP) requirements. SWaP limitations are primarily defined by the system platform, such as shipboard, airborne, terrestrial, or hand-carried systems. Over the years, there has been growing demand for smaller and more portable wireless devices, such as smartphones and integrated Internet of Things (IoT) sensors. Along with advances in semiconductor technology and integration techniques like System-on-Chip (SoC), RF companies now aim to integrate radio frequency front-end (RFFE) components into a single chipset to reduce production costs and minimize overall dimensions [8]. Consequently, RFFE architectures must have a smaller footprint and minimal power consumption [9, 10]. The system application and SWaP constraints will form the baseline for various trade-offs to maximize overall system performance.

1.2 Dynamic Spectrum Access Technologies

The traditional spectrum allocation grants licensed or primary users (PU) exclusive access to a fixed spectrum band. Unfortunately, with the increase in wireless communication devices and services, both licensed and unlicensed frequency bands are overcrowded and can degrade system performance [11, 12]. A technique used to overcome this issue is known as dynamic spectrum access (DSA) and involves the real-time adjustment of spectrum utilization according to spectrum availability and system objectives [13].

Two basic components of DSA solutions are spectrum opportunity identification and spectrum opportunity exploitation [14]. In other words, the system must accurately identify and track idle frequency bands in both time and space, to later use that information to decide whether and how a transmission should occur. The technologies that enable DSA are cognitive radio (CR) technologies, which are commonly implemented on software-defined radio (SDR) platforms [12, 15]. DSA systems can also be implemented with a centralized database, similar to the approach used in the Citizens Broadband Radio Service (CBRS) band [16]. In this setup, a Spectrum Access System (SAS) database coordinates frequency allocation and monitors spectrum usage across devices in real-time, ensuring compliance with regulatory requirements and optimizing spectrum utilization across users.

A CR is defined as a context-aware, intelligent radio capable of autonomous reconfiguration by learning from and adapting to the communication environment [14, 15]. SDR platforms implement radio functionalities by replacing traditional fixed hardware with software-defined operations, facilitating the adaptive functionality that characterizes CRs

[13]. Figure 1.3 illustrates the relationship between these concepts in a real wireless system architecture.

Different DSA strategies can be employed to optimize spectrum usage. One example is the hierarchical access model, where secondary users (SUs) are allowed to transmit in licensed spectrum bands as long as the interference perceived by the primary users (PUs) is limited. The main DSA models in this category are the interweave and underlay models [14], as shown in Fig. 1.4. In the interweave DSA model, also called opportunistic spectrum access, the cognitive radio uses a *sensing* antenna to search for spectrum holes or white spaces in the temporal, spatial, and/or frequency domain. Then, a *communicating* antenna tunes its operating frequency accordingly, allowing SUs to transmit without any power constraints in the selected bands [12, 17].

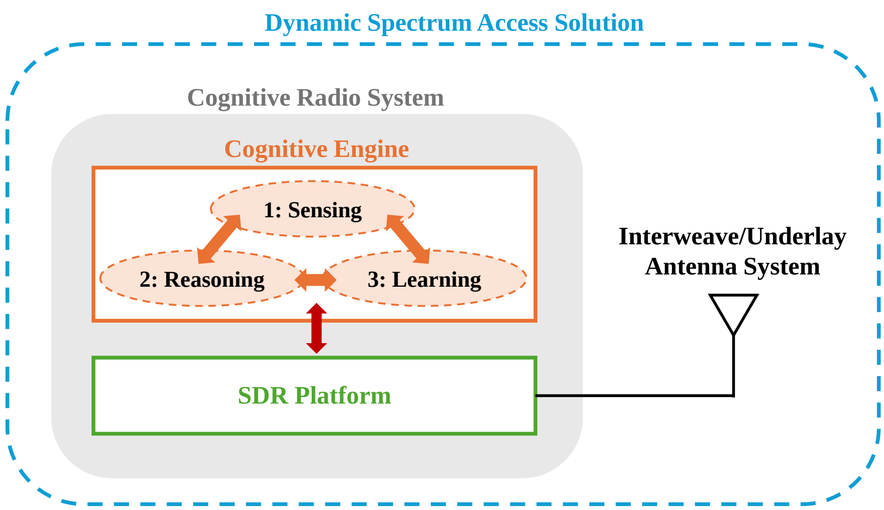

Figure 1.3: Relationship of dynamic spectrum access (DSA), cognitive radio (CR), and software-defined radio (SDR) technologies within a real wireless system. Adapted from [17].

On the other hand, an underlay DSA model allows secondary users (SUs) to transmit continuously within an allowed interference level, usually set to maintain primary user (PU) performance [12, 17]. This strategy requires a wideband antenna capable of tuning its notch frequency based on the PUs' activity, as both users will share the available spectrum bands.

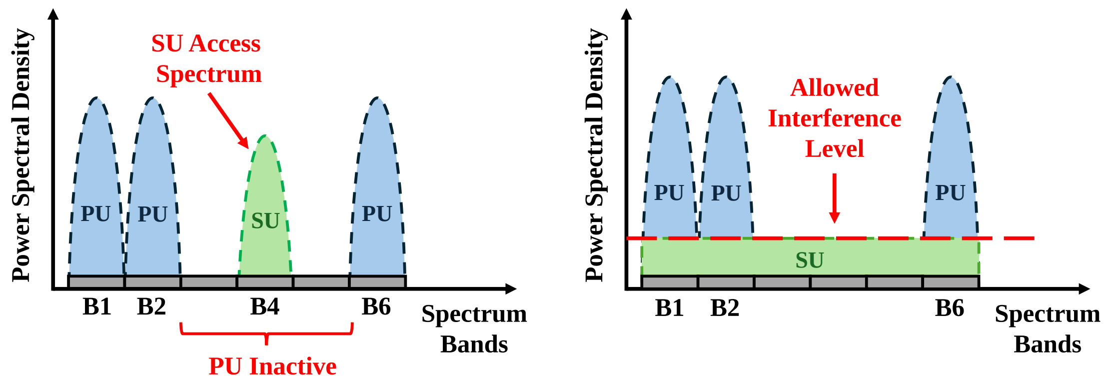

(a) Interweave (b) Underlay

Figure 1.4: DSA hierarchical access models: (a) the interweave model, and (b) the underlay model. Both models seek to provide spectrum access to secondary users (SU) while prioritizing primary users (PUs) performance. Adapted from [12, 17].

As a result of these different approaches, different RFFE requirements need to be met. Previous sections in this chapter highlighted how the antenna requirements vary according to the wireless system application. Therefore, to overcome spectrum congestion through DSA or CR solutions, additional antenna reconfigurability characteristics will be required [6].

1.3 Literature Review of Reconfigurable Antenna Analysis on System Performance

Recent advances in antenna design for CR systems have emphasized the importance of reconfigurability and filtering properties to enhance system performance. This subsection reviews literature specifically focused on studies that assess system-level performance with reconfigurable antennas in SDR and CR applications. By concentrating on how these integrated systems are evaluated, this review aims to summarize the methodologies and metrics used to analyze overall system effectiveness, rather than isolated reconfigurable antenna performance.

Tawk [17] proposed two multiple-input multiple-output (MIMO) systems for the previously discussed interweave and underlay DSA models. The interweave antenna system consists of two pairs of antennas. Fig. 1.5a shows the fabricated reconfigurable filtenna (filtering antenna) and sensing antenna. The radiating elements are a modified printed monopole and two half-elliptically shaped patches for each case. Fig. 1.5b illustrates the frequency response corresponding to the reconfigurable bandpass filter integrated into the antenna's feeding line. In this case, reconfigurability was achieved using PIN diodes at the edges of the main T-shaped slot of the filter. Similarly, Fig. 1.5c shows the fabricated underlay MIMO antenna system, and since underlay models generally require wideband antennas, a band-reject filter was integrated into the modified printed dipole. Fig. 1.5d displays the frequency response and its tuning according to the PIN diodes.

Both antenna systems were evaluated based on key parameters such as reflection coefficient, coupling, radiation patterns, and efficiency. The system performance was measured only at the antenna MIMO system level and not in combination with an SDR platform. The main metrics were the envelope correlation coefficient (ECC), used to determine whether the antenna elements received uncorrelated signals and mean effective gain (MEG).

Kantemur [18] proposed a compact antenna design with an 11.5:1 bandwidth, capable of operating between 430 MHz and 5 GHz. The design incorporates a UWB antenna with two independent paths and a varactor-based matching network, providing substantial operational flexibility in the 430 MHz to 1 GHz range. The antenna's performance was evaluated using S_{11}, radiation patterns at different frequency points, efficiency, and gain. The antenna's performance in a CR system was tested with a Universal Software Radio Peripheral (USRP) by National Instruments, using the proposed UWB antenna as a receiver antenna and a log-periodic antenna as the transmitter. Quadrature Phase Shift Keying (QPSK) modulated signals were used to calculate the bit error rate (BER) and the signal-to-noise ratio (SNR) per bit.

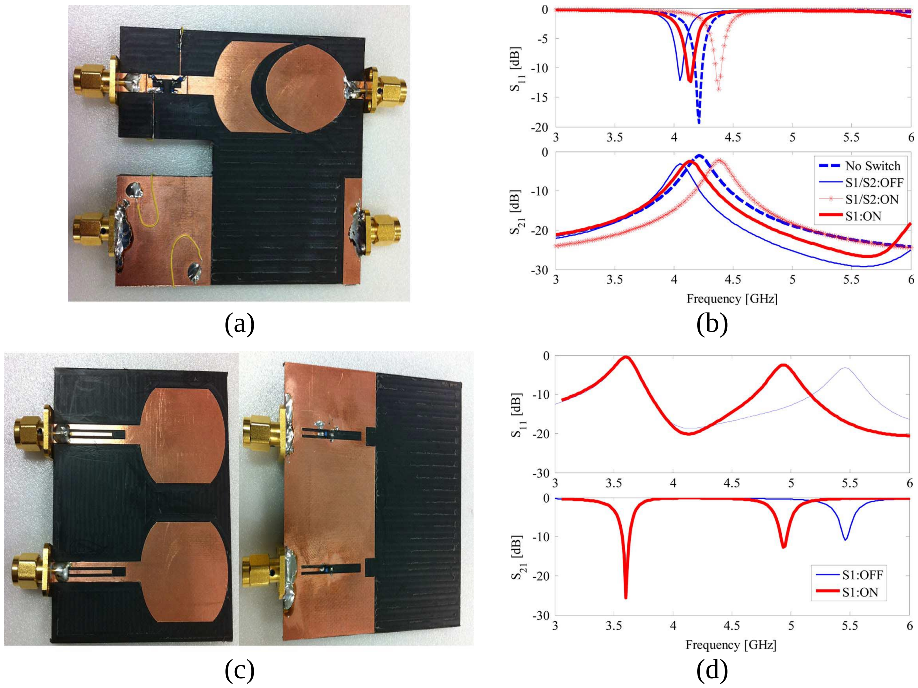

Figure 1.5: MIMO interweave and underlay reconfigurable antenna and their tunning mechanisms frequency response, as presented in [17]. The fabricated (a) interweave antenna system uses a reconfigurable band-pass filter to tune its operating frequency. The (c) underlay antenna system elements consist of a broadband antenna with an integrated reconfigurable band-reject filter. The frequency response for both filters can be seen in (b) and (d), respectively.

Similarly, Ibrahim [19] proposed a filtenna integrating a monopole rectangular patch with a BPF that uses two coupled defected ground structure (DGS) resonators with varactor diodes, along with two coupled microstrip lines ending in two stubs. The antenna operates in the frequency band from 1.3 GHz to 3 GHz, and the varactor can tune the antenna's resonant frequency from 2.7 GHz to 2 GHz. The antenna's performance was evaluated using the S_{11} response. For the system performance analysis, a BladeRF was used as the SDR platform. The proposed filtenna was employed for spectrum sensing as a single unit. To simulate a CR scenario, six QPSK-modulated signals were transmitted using a standard monopole antenna at six different carrier frequencies. The power spectral density (PSD) received by the filtenna demonstrated its out-of-band (OOB) rejection capabilities. Additionally, for a single QPSK signal at a defined carrier frequency, the BER was found to be zero.

Henthorn [20] proposed a filtenna consisting of a multi-layer frequency selective surface (FSS) integrated into a cavity-backed waveguide with monopole feeding. The filtenna is tunable from 1.44 GHz to 1.94 GHz due to a four-layer reconfigurable bandpass FSS embedded with varactor diodes. The SDR platform concept is extended by using a direct RF sampling approach. The receiver's RF front-end consists of the filtenna, an LNA, and a LeCroy WaveMaster 813Zi-A oscilloscope for analog-to-digital conversion (ADC). The digital back-end is implemented in LabVIEW, operating on a National Instruments PXIe8135. The receiver's performance is characterized both independently and in terms of out-of-band (OOB) blocking and adjacent channel selectivity (ACS) performance. The error vector magnitude (EVM) and block error rate (BLER) were calculated based on 144-bit QPSK-modulated signals.

The experimental setups used for the system-level performance analyses in [18, 19, 20] are shown in Fig. 1.6. Table 1.1 compares the reviewed literature and outlines the main differences with the work that will be presented in this thesis.

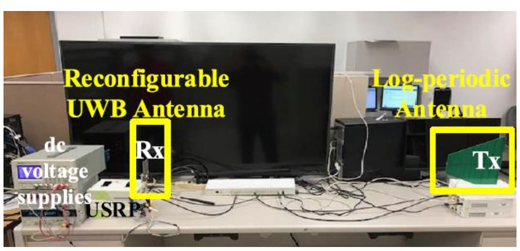

(a)

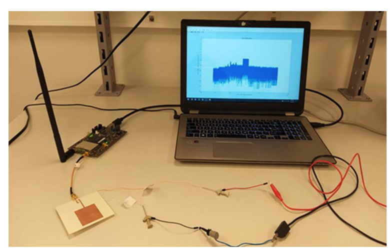

(b)

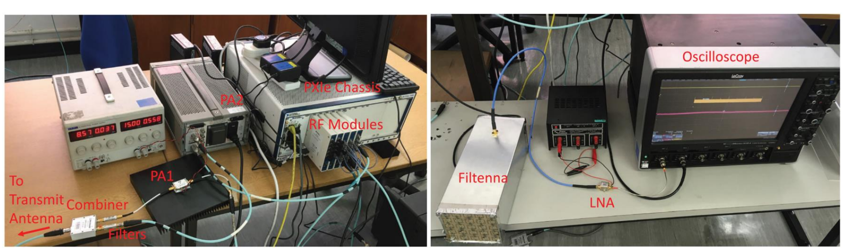

(c)

Figure 1.6: Experimental setups for the system-level performance analysis in the reviewed literature. Available hardware and measurement environment images from (a) [18], (b) [19], and (c) [20].

In summary, Tawk [17] focused on MIMO antenna systems with reconfigurable filtering properties, demonstrating their potential in CR applications but only evaluated performance at the antenna level. Similarly, Kantemur [18] proposed a compact wideband antenna design with significant operational flexibility; however, the system's performance was tested in a basic USRP setup, leaving room for more comprehensive evaluations in congested environments. Likewise, Ibrahim [19] introduced a filtenna for spectrum sensing with out-of-band rejection capabilities, but its performance was measured under a limited test scenario without actual interference signals. Henthorn [20] further advanced reconfigurable antenna system-level analysis by integrating a reconfigurable antenna with a direct RF sampling SDR platform. However, the testing primarily focused on OOB blocking and ACS using a single frequency-invariant continuous wave (CW) interferer, without addressing complex spectrum conditions.

Table 1.1: Literature review comparison on reconfigurable antenna analysis in CR system-level performance

Ref.	**Center Frequency**	**System Performance Metrics**	**SDR Platform**	**Modulation**	**Interferer Presence**	**Antenna Comparison**
[17]	4.21 GHz	ECC MEG	N/A	N/A	No	No
[18]	715 MHz 3 GHz	BER SNR per Bit	USRP	QPSK	No	No
[19]	2.15 GHz	Spectrum sensing PSD BER	BladeRF	QPSK	No	No
[20]	1.69 GHz	EVM BLER	Direct RF sampling (Oscilloscope + PXIe)	QPSK CW	Yes	No
This work	2.3 GHz	OOB Received Power SINR	USRP	QPSK	Yes	Yes

Overall, as shown in Fig. 1.6, the system-level performance analyses in these papers were conducted in uncontrolled and non-isolated environments, making them susceptible to external interference or perturbations that could affect the results. Thus, while these studies contribute to reconfigurable antenna research at the system level, they highlight the need for more rigorous evaluations in controlled and congested spectrum conditions to accurately assess the capabilities of reconfigurable antennas in CR systems.

1.4 Thesis Outline

The objective of this thesis is to investigate the impact of antenna choices on system performance, specifically focusing on the performance trade-offs required for applications involving frequency filtering and reconfigurability at the aperture level. The current literature shows that the few papers integrating reconfigurable antennas with SDR platforms and performing system-level performance analysis have several shortcomings. This work addresses these issues, building on the research done in [21], by simulating a congested spectrum environment with an SDR-based testbed that allows for the comparison of various antenna designs in a controlled test environment. By incorporating these elements, this research provides a comprehensive assessment of antenna performance under pseudo-real-world conditions, improving the overall evaluation of antenna selection for congested spectrum scenarios, and a more rigorous evaluation of CR system performance.

The fundamental design theory of reconfigurable and filtering antennas is presented in Chapter 2, including the different tuning techniques used to achieve reconfigurability. Furthermore, SDR platform architectures are discussed, with a focus on USRP technologies and the tools required to implement software capabilities. Additionally, wireless system performance metrics are covered to properly assess the findings of this work.

Chapter 3 introduces the definition of a congested spectrum environment in the presence of frequency-variant interference. The proposed SDR-based testbed system is described in detail, along with the system architecture used to emulate the congested spectrum environment conditions and allow for receiver antenna comparison. All the antenna, hardware, and software characteristics used for the measurements are specified. The control loop for the measurements and setup of the far-field anechoic chamber are presented.

In Chapter 4, the results for four different types of receiving antennas using the congested spectrum SDR-based testbed are presented and discussed. The results include received interference power both in and out of the band, receiver filtering performance, signal-to-interference plus noise ratio (SINR), and packet error rate (PER). The filtering capabilities of the SDR platform were also independently tested and used as a reference for antenna comparison. A discussion of the findings for system-level implications that the results yield is presented at the end of this chapter.

Chapter 5 concludes with a summary of the work presented in this thesis, highlighting the main scientific contributions. Additional future work is proposed to extend the analysis metrics used to evaluate system performance, providing an even broader picture of antenna selection implications for CR systems.

Lastly, Appendix A expands on the spatial filtering capabilities of antennas at the aperture level. It presents the optimization of an X-band reflector antenna for sea clutter rejection, analyzing the effects of different components in reflector antenna design on the radiation pattern. The design was used alongside a MATLAB simulation to achieve the best sea clutter rejection for the intended elevation angles. The results and trade-offs identified for this specific application are discussed, and conclusions are drawn.

Chapter 2

Reconfigurable Technology Literature Review

The demand for enhanced performance, flexibility, and adaptability in modern wireless systems has driven significant advancements in antenna technology. This chapter provides an overview of key concepts essential to understanding reconfigurable antennas, frequency-filtering antennas, and their role in modern communication systems. Reconfigurable antennas offer dynamic adaptability, which is vital in versatile wireless applications. In addition to this, frequency-filtering antennas enhance signal channel selectivity. The integration of these antenna technologies with SDR platforms, which enable real-time control and reconfiguration of radio functions, further optimizes system performance. Additionally, fundamental wireless communication concepts will be discussed to contextualize their significance in such systems.

2.1 Reconfigurable Antennas

Reconfigurable antennas have emerged as a critical component in modern wireless communication systems, offering the ability to dynamically adapt to changing operational requirements. This section explores the fundamental aspects of reconfigurable antennas, beginning with a clear definition of their unique characteristics and capabilities. The various tuning techniques to achieve said reconfigurability are discussed, highlighting their advantages and disadvantages under certain conditions or application contexts. Finally, practical applications of reconfigurable antennas across diverse wireless systems will be overviewed.

2.1.1 Reconfigurable Properties

Reconfigurable antennas achieve adaptability by altering their radiated fields through a controlled redistribution of antenna currents or adjustments to radiating edges [22]. Therefore, a reconfigurable antenna is one that can change its key properties such as frequency, radiation pattern, and polarization, or a combination of these. Fig. 2.1 shows the reconfigurability in each of these aspects.

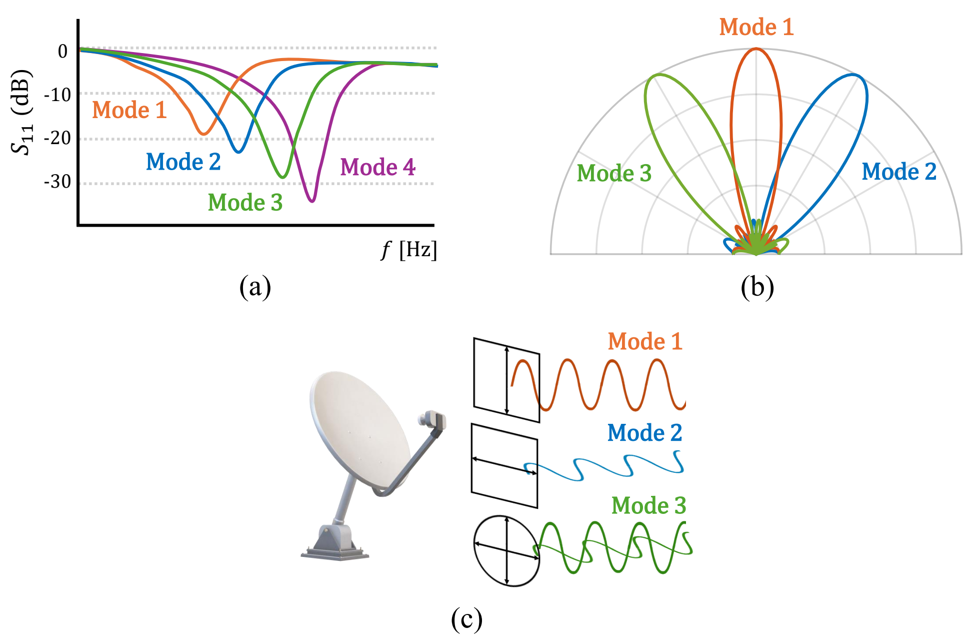

Figure 2.1: Main reconfiguration properties for reconfigurable antennas: (a) Frequency reconfigurability is shown by the change in operating frequency in the S_{11} response according to the operating mode. (b) Radiation pattern reconfigurability is achieved by changing the antenna's main beam direction. (c) Polarization reconfigurability allows for the change in polarization types like linear vertically polarized, linear horizontally polarized, circularly polarized, etc. Adapted from [23].

Frequency reconfigurability refers to the change of operating or notch frequency by hopping through different frequency bands, as shown in the S_{11} response in Fig. 2.1(a). Radiation pattern reconfigurability is the ability to modify the radiation pattern shape, direction, and/or gain. Fig. 2.1(b) shows an example of radiation pattern reconfiguration by changing the main beam direction. Lastly, polarization reconfigurability refers to the antenna's ability to change from certain polarization to another. For example, from linear horizontal polarization to linear vertical polarization, or from linear to circular polarization, as illustrated in Fig. 2.1(c).

These properties make reconfigurable antennas highly versatile and capable of dynamically adapting to varying environmental conditions or system demands [24]. The ability to reconfigure an antenna without physical reconstruction is particularly valuable in modern deployed RF systems. However, several considerations are essential for successfully achieving reconfigurability. First, the specific reconfiguration property or properties should be defined according to the application. Then, it is important to consider the different radiating elements of the antenna structure and determine which reconfiguration technique will best minimize potential negative effects on the antenna's radiation pattern or impedance characteristics.

2.1.2 Reconfiguration Techniques

The reconfiguration techniques used to achieve a change in the previously discussed properties can be divided into four major categories: electrical, optical, mechanical, and material change [22, 25]. As shown in Fig. 2.2, each category uses different components or techniques. These techniques present different working principles and integration considerations, which translate into different switching speeds, isolation characteristics, loss, etc.

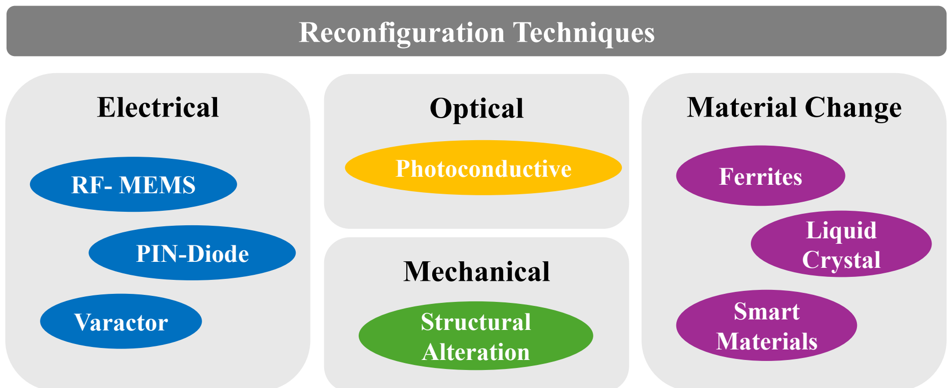

Figure 2.2: Major categories of reconfiguration techniques based on their operating principles. Adapted from [24].

Electrical reconfiguration techniques involve using switches to connect or disconnect specific geometries from the antenna or feeding line, redistributing currents across the antenna volume [22, 26]. Common elements used include radio frequency micro-electromechanical systems (RF-MEMS), positive-intrinsic-negative (PIN) diodes, and tunable varactors.

RF-MEMS switches create short or open circuits in RF circuits through mechanical movement. Designs vary based on signal path (series or parallel), actuation mechanism (electrostatic, magnetostatic, piezoelectric, or thermal), contact type (ohmic or capacitive), and structure (cantilever or bridge) [24, 25, 27]. They offer low loss, minimal power consumption, high isolation, and linearity [26], but have relatively slow switching speeds of 1-200 microseconds [22]. Fig. 2.3(a) shows the reconfigurable annular slot antenna proposed in [26], which uses RF-MEMS actuators strategically located within the antenna geometry and microstrip feed line to achieve two reconfigurable frequencies of operation with center frequencies at 2.4 GHz and 5.2 GHz.

PIN diodes function as variable resistors at RF and microwave frequencies, depending on their biasing state. When forward biased (‘ON’), they exhibit low impedance, allowing signal transmission, while in reverse bias (‘OFF’), they present high impedance, reflecting most of the signal energy [28]. They offer low cost, high power handling, fast switching (1-100 nsec), good isolation, and low insertion loss. However, biasing circuits can complicate the design, potentially degrading antenna performance [29]. Additionally, they require a constant DC current from a driver [22]. Fig. 2.3(b) shows the frequency and pattern reconfigurable V-shaped printed antenna from [30], which operates at two frequency bands. The frequency variation is achieved by extending each antenna arm, with PIN diodes used to select either arm. The antenna steers its gain pattern left or right depending on the active arm.

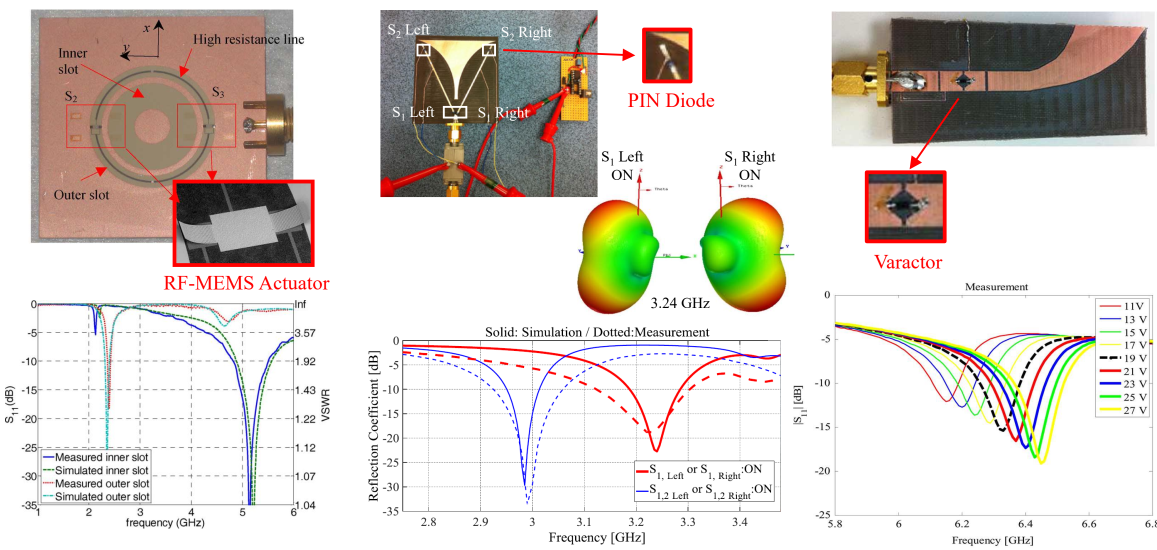

(a) (b) (c)

Figure 2.3: Reconfigurable antenna designs that include electrical reconfiguration techniques: (a) Reconfigurable annular slot antenna with integrated RF-MEMS [26], (b) frequency and pattern reconfigurable printed V-shaped antenna using PIN diodes [30], and (c) a varactor-based reconfigurable filtenna [31].

A varactor, or varactor diode, consists of a p-n junction diode that behaves as a variable capacitor under different reverse bias voltages [22, 28]. Unlike PIN diodes, which require a constant current supply, varactors need a direct supply of DC voltage. By adjusting the bias voltage, the capacitance of the varactor changes. This allows antennas to achieve a wide tuning range by integrating a variable capacitance into the antenna structure. Typical capacitance values range from tens to hundreds of pico Farads. Fig. 2.3(c) shows the varactor-based reconfigurable antenna from [31], which integrates a frequency-tunable bandpass filter into the antenna's feeding line. This enables frequency tuning by adjusting the filter capacitance via an integrated varactor, without adding active components or biasing lines on the antenna radiating surface.

Optical reconfiguration techniques use photo-conductive switches. An optical switch is formed when laser light, usually generated from integrated laser diodes, is incident on a semiconductor material like silicon. This results in exciting electrons from the valence to the conduction band thus creating a conductive connection [24]. Their linear behavior and the absence of biasing lines compensate for their lossy aspect and for the integration and power issues [22]. Fig. 2.4(a) shows the narrowband reconfigurable antenna from [32], which uses laser diodes to control photoconductive silicon switches. This eliminates the need for optical fiber cables and allows easier integration into communication systems.

In mechanical reconfiguration, the main radiator of the antenna can be reconfigured mechanically to provide different characteristics, typically using tuning elements like metal screws or movable posts to achieve low losses, good linearity, and relatively high power-handling capacity [25, 33]. However, the performance flexibility of this type of antenna is limited, and controlling the driving actuators can be power-consuming. Although the actuator tuning speed is slower than that of any switching component, it has proven sufficient for most applications [22]. The mechanically reconfigurable patch antenna with polarization diversity presented in [34], shown in Fig. 2.4(b), consists of a fixed L-probe feed and a rotatable patch with truncated corners. The L probe is impedance-matched to patch sizes resonating between 1.0 and 1.8 GHz, and rotating the patch by 90 ° switches the circular polarization between the right-hand and left-hand hands.

Reconfigurable antennas based on material change take advantage of alterations in substrate characteristics using materials such as liquid crystals or ferrites [24]. For instance, liquid crystals are nonlinear materials whose dielectric constant can be modified under different voltage levels by adjusting the orientation of the molecules. In ferrite materials, a static applied electric or magnetic field can change the relative permittivity or permeability of the material. Another approach involves the use of metamaterials and metasurfaces, which are well-known for exhibiting properties unattainable with ordinary materials, such as negative permittivity, permeability, or refractive index [35]. Additionally, metamaterials and frequency selective surfaces (FSS) can function as phase transformation devices when placed in the near-field region for beam-steering applications. In Fig. 2.4(c), a nematic liquid crystal (N-LC) cell is used as a substrate for a microstrip patch antenna to control its resonant frequency using a DC or low-frequency AC bias voltage, as shown in [36].

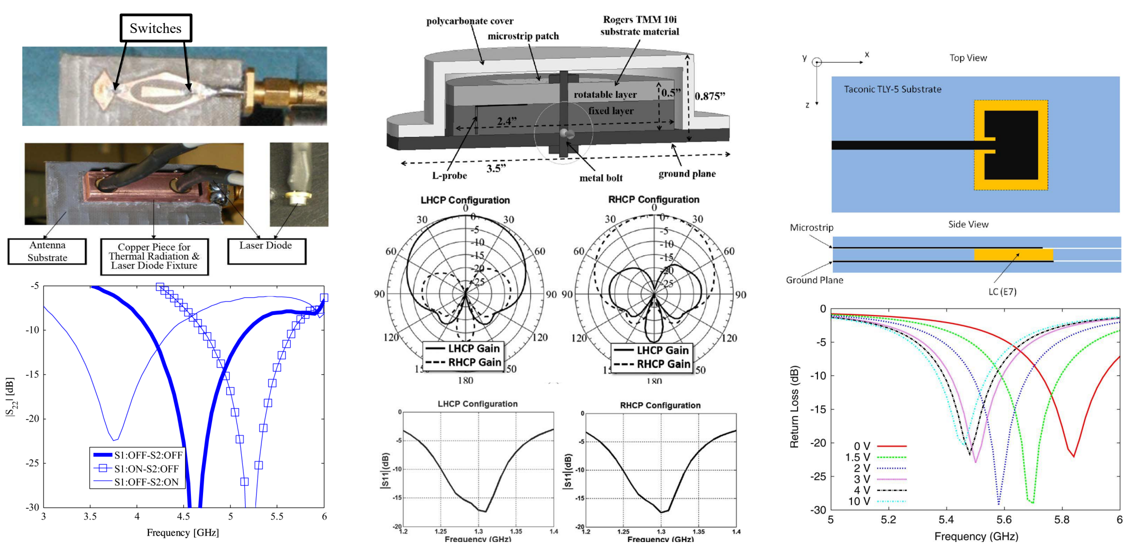

(a) (b) (c)

Figure 2.4: Reconfigurable antenna designs that include optical, mechanical, and material change reconfiguration techniques. (a) Reconfigurable narrowband antenna from [32] which uses laser diodes to control photoconductive silicon switches. (b) Rotatable L-feed patch antenna with polarization diversity presented in [34]. (c) Microstrip patch antenna built in nematic liquid crystal to achieve frequency reconfigurability as presented in [36].

Table 2.1 provides an overview of the advantages and disadvantages of various reconfiguration techniques discussed in this subsection: electrical, optical, mechanical, and material change. Each technique offers unique benefits in terms of tuning flexibility and integration, along with specific limitations in complexity, speed, or implementation.

Table 2.1: Advantages and disadvantages of the discussed reconfiguration techniques. Adapted from [25, 28].

Technique	Advantages	Disadvantages
Electrical Reconfiguration	• Low cost • Ease of implementation • Relatively fast switching	• Requires biasing lines
Optical Reconfiguration	• Fast switching speed • Eliminates biasing lines • Linear behavior	• Lossy behavior • Complex activation mechanism
Mechanical Reconfiguration	• Low cost • No biasing lines • No active elements	• Low switching speed • Requires power source • Limited flexibility
Material Change Reconfiguration	• Low profile • Lighter weight	• Higher cost • Limited applications

2.1.3 Applications

Reconfigurable antennas are integral to various modern communication systems, including cognitive radio (CR), multiple-input multiple-output (MIMO) systems, and space and satellite communications. In CR, these antennas adapt to dynamic spectrum availability, ensuring reliable communication in challenging environments [22]. The integration of reconfigurable antennas into MIMO systems enhances spectral efficiency by allowing simultaneous transmission of multiple data streams. This capability is further improved through radiation pattern and polarization reconfiguration, which offers greater flexibility in selecting patterns and configurations, significantly improving system capacity and performance [24].

Millimeter-wave (mmWave) communication, particularly in the 40-50 GHz and 70-80 GHz frequency ranges, faces challenges related to high path and penetration losses. In this context, reconfigurable antennas play a key role by dynamically adjusting their radiation pattern characteristics to maintain communication links. Their ability to adapt to varying operational environments helps avoid the need for multiple antenna structures, ensuring reliable communication in these emerging frequency bands [35]. Additionally, Fig. 2.5 shows how radiation pattern reconfigurability can be used to improve system performance by directing the main lobe to the communicating users and mitigating interference from other users.

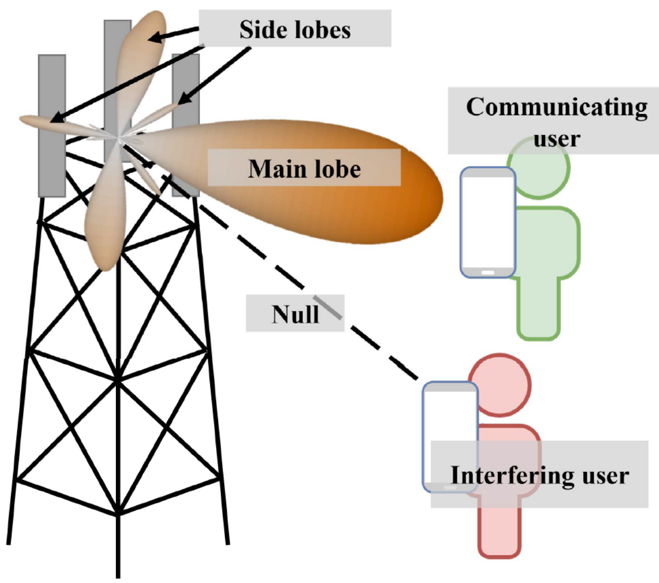

Figure 2.5: Radiation pattern reconfigurable antenna being used to ensure communication between base station and users, as seen in [35].

In satellite and space communications, reconfigurable antennas are crucial for adapting to changing coverage needs and environmental conditions. Satellites often require reconfiguration of their radiation patterns to extend coverage, mitigate signal fading in adverse weather, and maintain high data rates across different frequency bands [24]. The development of small satellites and CubeSats has also driven the demand for agile, deployable antennas. Combining reconfigurable and deployable designs provides a practical solution to meet the increasing communication requirements in space [22].

2.2 Frequency filtering antennas

Frequency-filtering antennas, also known as "filtennas," are specialized antenna systems designed to selectively transmit or receive signals within specific frequency bands. These systems combine filtering and radiation functionalities, which enhance frequency selectivity, in-band gain stability, out-of-band rejection, and overall system efficiency [37, 38]. This section provides an overview of their key characteristics, including common design methods and a range of practical applications across various fields.

2.2.1 Design Methods

In the literature, there are several design methods to implement a filtering antenna. Each offers unique advantages and addresses specific challenges associated with frequency selectivity and system performance. These can be summarized in three main design approaches: cascaded filter antennas, the synthesis method, and the fusion method [38].

The first, traditional approach involves cascading a filter circuit into the antenna structure, either by using a 50 Ω interface or by integrating the filter into the antenna's feeding line [38]. This approach is straightforward and convenient, as the antenna and filter can be individually designed and tuned. For example, a reconfigurable narrowband bandpass filter (BPF) and a broadband antenna can be combined to create a reconfigurable filtenna [31], as illustrated in Fig. 2.6(a). However, any additional transmission lines or interfaces may result in extra insertion loss, and bandwidth mismatches between the two components can cause signal distortions at the band edges [33]. An example of the cascaded method is presented in [17] and shown in Fig. 1.5.

In the synthesis method based on BPF, the antenna functions as both the radiating element and the final resonator in a high-order BPF network [39, 40]. As illustrated in Fig. 2.6(b), the antenna acts as a shunt resistor-inductor-capacitor (RLC) resonator, with

R_L representing the radiation resistance. The other resonator is modeled by a shunt LC resonator, and the coupling between them is represented by a J inverter, resulting in a second-order filter response for this configuration. This approach offers key advantages, including reduced volume and complexity in the RF front-end by eliminating 50-ohm interfaces, which improves overall efficiency [38]. Fig. 2.7(b) shows a filtering patch antenna based on a quarter-wavelength (λ/4) resonator presented in [40]. In this design, the resonant patch radiator is capacitively fed by two inductively coupled λ/4 resonators, achieving a third-order bandpass filtering property.

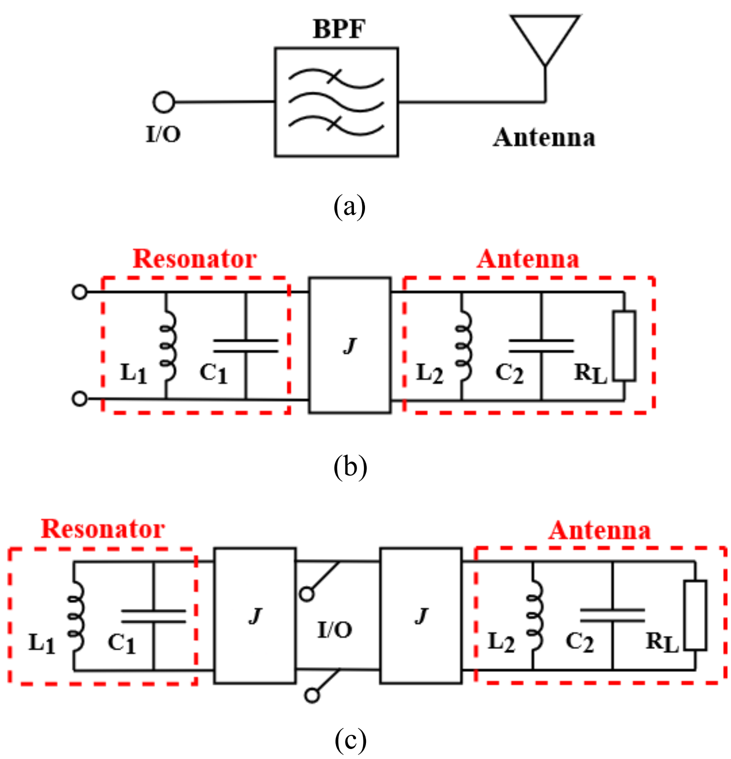

Figure 2.6: Filtering antenna design approaches: (a) cascaded filter antennas, (b) synthesis method based on the couple-resonator filter theory, and (c) fusion method. Adapted from [38].

Lastly, in the fusion method, the filtering function is achieved by introducing simple parasitic elements or resonators into the radiator or feeding circuit [41]. These resonant structures are integrated in parallel with the antenna to generate band-stop functions on either side of the passband, as shown in Fig. 2.6(c) [38]. Radiation nulls can be intentionally designed to control the bandwidth and frequency selectivity of the antenna. A low-profile, omnidirectional triangular patch antenna, axially fed at its center to excite both TM10 and TM11 modes, is presented in [41] and shown in Fig. 2.7. This triangular patch uses a ring slot and shorting vias to merge the modes, creating radiation nulls at both band edges. The result is a compact filtering antenna with a quasi-elliptic bandpass response, achieved without additional filtering circuits.

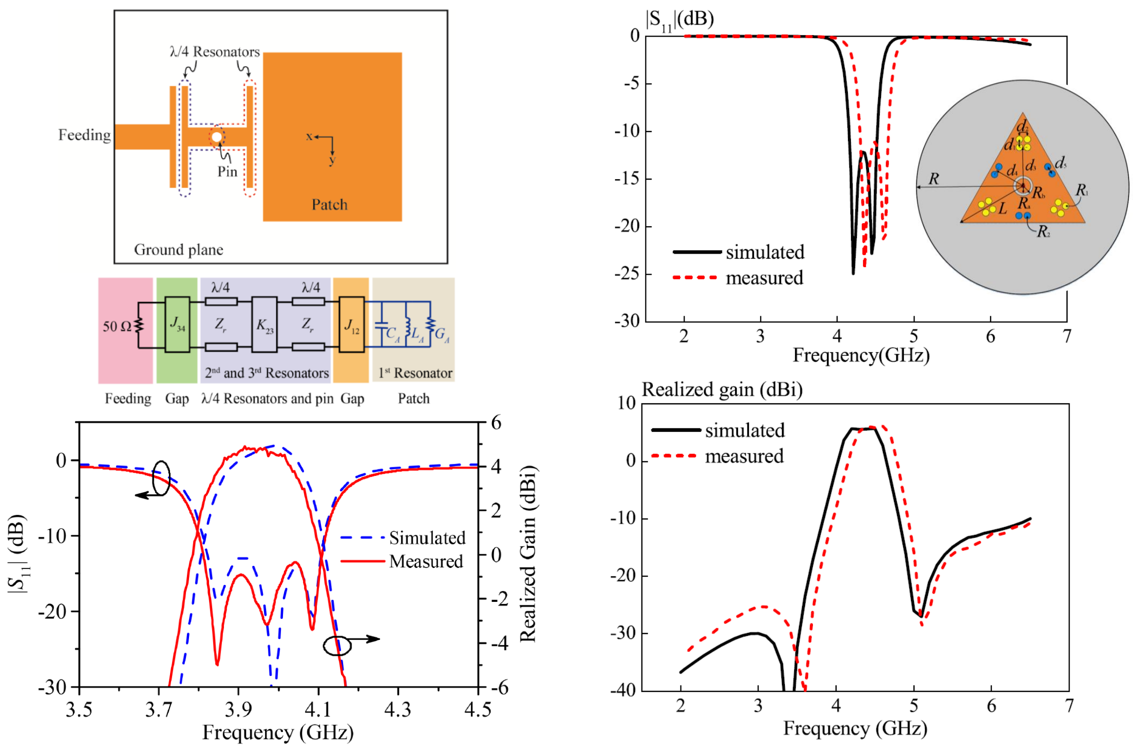

(a) (b)

Figure 2.7: Filtering antenna designs based on the coupled resonator synthesis and fusion approach. (a) Filtering patch antenna based on the coupled resonator synthesis method for a third order bandpass response using the resonating patch and $\lambda/4$-resonators [40]. (b) Filtering triangular patch antenna with a ring slot to generate extra radiation nulls through the fusion method [41]

2.2.2 Applications

RF desensitization, also known as receiver desensitization, occurs when strong adjacent interferer signals induce nonlinear effects in the receiver's input stages [42], resulting in a degradation of signal-to-noise ratio (SNR) that is challenging to model accurately. Additionally, the analog-to-digital converter (ADC) block is vulnerable to these strong interference signals, which can limit its dynamic range or cause saturation. In simpler terms, a receiver that would normally detect weaker signals becomes unable to do so because the strong interfering signals generate spurious emissions within the receiver. These issues underscore the critical role of effective analog filtering in enabling the successful implementation of digital filtering or mitigation techniques.

By selectively transmitting or receiving signals within specific frequency bands, filtering antennas help prevent strong adjacent or out-of-band signals from overwhelming the receiver, thereby reducing the likelihood of desensitization [43]. This capability makes them particularly useful in crowded RF environments, such as cellular networks, wireless communication systems, and radar applications, where interference from nearby signals is a significant concern. Furthermore, the use of filtering antennas in transmitter nodes can reduce the likelihood of the system jamming other nearby systems due to its spectral mask.

Filtering antennas are highly beneficial in CR applications due to their ability to provide precise frequency selectivity while maintaining optimal radiation performance. In cognitive radio systems, the antenna must efficiently switch between multiple frequency bands to sense and adapt to the available spectrum. Filtering antennas, with their integrated bandpass filtering capabilities, help achieve this by enabling seamless transitions between different frequencies without the need for additional external filters. This reduces system complexity, minimizes interference from out-of-band signals, and improves overall spectrum efficiency, making them ideal for dynamic spectrum access in cognitive radio environments.

In MIMO applications, filtering antennas enhance performance by improving isolation between multiple antennas and reducing mutual coupling. Their built-in filtering characteristics suppress unwanted signals and limit interference between closely spaced antennas, resulting in improved SNRs and more reliable communication. Additionally, tunable filtering antennas can be designed to operate across different frequency bands, polarizations, and radiation pattern characteristics, offering the diversity required for advanced MIMO systems. By combining compact size, agility, and reduced interference, filtering antennas play a crucial role in improving the efficiency and performance of both CR and MIMO systems.

2.3 Software-defined Radio (SDR) Platforms

Software-defined radio (SDR) is a radio communication technology that relies on software-defined wireless protocols rather than traditional hardware-based solutions. This enables various features and functionalities, such as updating and upgrading through reprogramming, without needing to replace the underlying hardware [44]. The high demand for SDR is driven by factors like network interoperability, adaptability to future updates and new protocols, and, most importantly, reduced hardware and development costs.

Based on its operational capabilities, an SDR system can be classified as (i) multiband, (ii) multistandard, (iii) multiservice, and/or (iv) multichannel [45]. Multiband systems support multiple frequency bands used by wireless standards. Multistandard systems support more than one standard, enabling operation across different networks. Multiservice systems provide different wireless services, such as telephony, data, or video streaming. Lastly, multichannel systems allow simultaneous support of two or more independent transmission and reception channels.

The following subsections present the fundamental architecture of SDRs and examine the various hardware platforms utilized. An outline of the key components and technologies that enable SDR functionality is presented, highlighting the diverse hardware options available to meet different operational requirements.

2.3.1 Basic Architecture

An ideal SDR architecture consists of three key components: a reconfigurable digital radio, a software-tunable radio with an embedded impedance synthesizer, and software-tunable antenna systems [15]. Together, these units implement a CR system, as illustrated in Fig. 2.8.

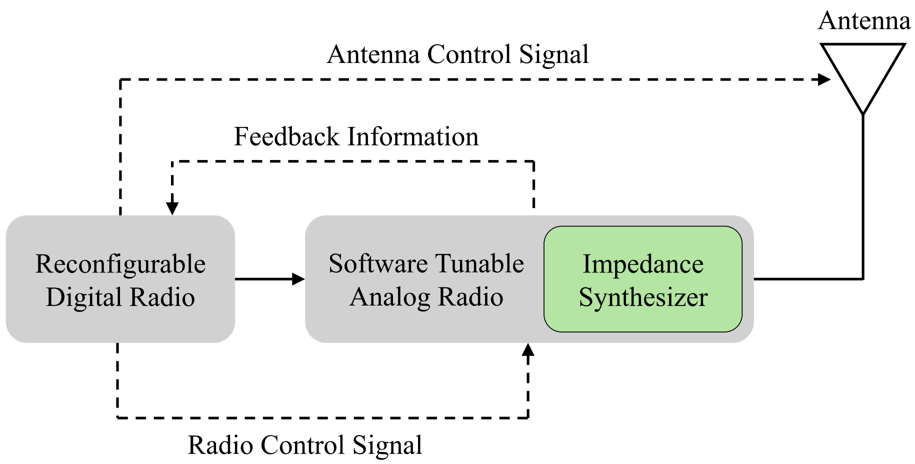

Figure 2.8: An ideal SDR architecture, adapted from [15]. The reconfigurable digital radio unit manages the software tunable analog radio and antenna units according to the system's requirements. The software tunable analog radio unit contains the tunable RF front-end and impedance synthesizer required for the antenna unit optimal performance.

First, the cognitive engine transmits radio configuration parameters (e.g. waveform types, bandwidth, operating center frequency) to the reconfigurable digital radio. The reconfigurable digital radio is responsible for executing digital radio functions, including generating various waveforms, applying optimization algorithms for the software-tunable radio and antenna units. To optimize system performance, the reconfigurable digital radio continuously or periodically monitors and controls the software-tunable radio system based on the system's specifications.

The software-tunable analog front-end must keep up with the system requirements as well, however, it is limited by the components that cannot always be synthesized into the reconfigurable digital radio platform, such as RF filters, combiners/splitters, power amplifiers (PA), low-noise amplifiers (LNA), or data converters. Additionally, the unit includes an impedance synthesizer, a critical subsystem for optimizing the performance of software-tunable antenna systems according to the frequency plan set by the cognitive engine.

Due to current limitations in reconfigurable hardware technology, ideal SDR architectures are rarely achieved, and some compromises must be made for a more practical implementation. Fig. 2.9 shows examples of practical SDR architectures for both the transmitter and receiver sides. The main components of both receiver and transmitter chains can be defined or grouped into antennas, RF front-end, analog-to-digital or digital-to-analog conversion, digital front-end, and signal processing [44]. As previously discussed in Chapter 1, antennas work at the system aperture level. SDR platforms usually use several antennas to cover a wide range of frequencies, ultra-wideband (UWB) antennas, or reconfigurable antennas to achieve multiband operation [17, 18, 19, 20, 21].

In a practical SDR architecture, the RF front end refers to the RF circuitry responsible for transmitting and receiving signals across different operating frequencies, as well as converting signals from the carrier frequency to an intermediate frequency [44]. In the transmission path, the output analog signal from the DAC is up-converted with a certain RF frequency, amplified, and transmitted at a specific carrier frequency via the antenna. In the receiver path, the signal is received by the antenna at the carrier frequency, then amplified through an LNA to reduce the noise level, down-converted, and fed to the ADC. In some architectures, SDRs also control PA and LNA gains [15].

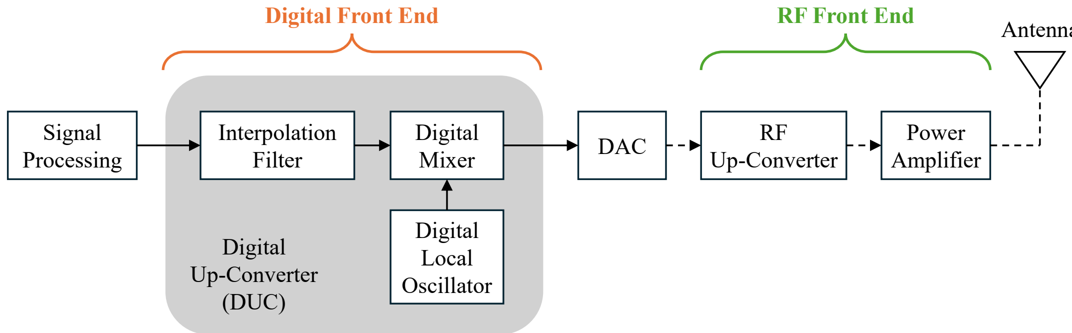

(a)

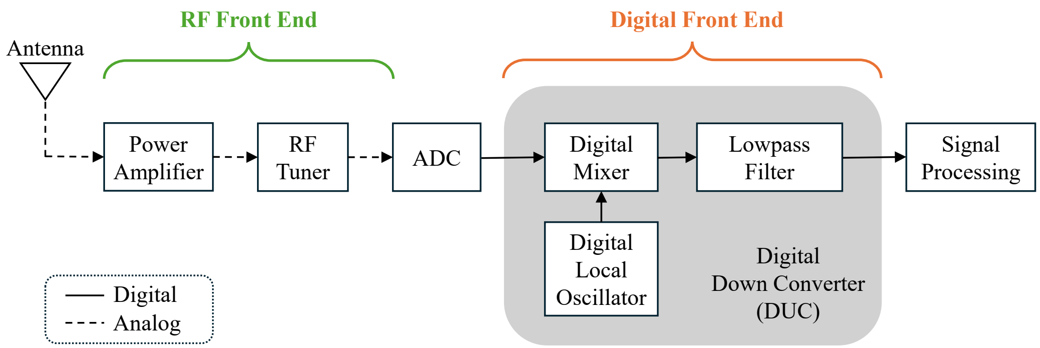

(b)

Figure 2.9: Practical SDR architecture for the (a) transmitter and (b) receiver chain, adapted from [44]. The connections of the digital front end integrated into the SDR platform are denoted by (–), whereas the external RF hardware connections, also referred as RF front end, are shown with (- -).

The DAC converts digitally generated samples into an analog signal suitable for transmission [44]. In contrast, the ADC component converts received continuous-time analog signals into discrete-time, binary-coded signals. Receiver SDRs typically have greater requirements, pushing ADC components to have higher bandwidth and dynamic range, hence, higher resolution [46]. Several performance metrics can be analyzed based on these characteristics, such as the maximum signal-to-noise ratio of the ADC, determined by quantization noise.

The digital front-end is the section that differs significantly from the superheterodyne receiver architecture shown in Fig. 1.2. In an SDR architecture, the IF-to-baseband or vice-versa conversion is performed digitally in both the transmitter and receiver chains. Although, recent advancements in direct RF sampling have enabled the entire carrier-to-baseband downconversion process to be digital or even direct sampling at carrier frequencies [47, 48]. The digital front-end block also synchronizes the sample rate between communication nodes and manages channelization for dual-channel architectures, as well as isolating frequency channels [15].

2.3.2 Reconfigurable Digital Radio Platforms

SDRs are implemented by employing various types of hardware platforms, such as General Purpose Processors (GPPs), Graphics Processing Units (GPUs), Digital Signal Processors (DSPs), and Field Programmable Gate Arrays (FPGAs) [44]. Each with their own set of advantages and disadvantages. However, when selecting the appropriate platform for the SDR application, one must consider their reconfigurability, integration with different layers, development cycle, performance, power consumption, cost, and size [15].

GPPs are commonly used for SDR platforms like Sora [49] and USRP [50]. GPPs are versatile, capable of handling numerous applications by processing binary data streams without needing application-specific circuits, thus reducing costs. However, they are inefficient for real-time high-throughput tasks due to their sequential processing nature. To overcome this, GPUs are added as co-processors to enhance parallel processing power, making the systems more flexible and powerful. Despite these advantages, GPP and GPU-based SDR platforms consume significant power, and their large form factors make real-world deployment difficult.

DSPs, like the TI TMS320C6670 [51] used in the Atomix platform, are specialized microprocessors designed to handle complex arithmetic tasks like modulation, filtering, and encoding. DSPs excel in speed and power efficiency compared to GPPs. However, DSPs struggle with highly parallel and reconfigurable tasks required by modern applications, and programming for such parallelism is challenging. This limitation has led to the exploration of alternative architectures, such as FPGAs and multi-core processors.

FPGAs, used in platforms like Airblue [52] and Xilinx Zynq [53], are programmable hardware circuits that consist of logic, memory, and multiplier blocks. They offer high-speed performance, low power consumption, and flexibility, as they can be reprogrammed for different tasks. FPGAs can be reconfigured within milliseconds, enabling seamless switching between modes in SDR systems. However, using FPGAs requires prior knowledge of the hardware architecture, making it challenging for developers who are more familiar with software design. Despite this, the growing use of high-level synthesis tools is making FPGA adoption more feasible for SDR applications.

Hardware/software co-design integrates FPGA hardware with software methodologies, combining the strengths of processors and dedicated hardware. This hybrid design approach allows SDR platforms to achieve higher performance and real-time processing by accelerating tasks through FPGA fabric. In this model, the general processor handles control functions while specialized processors, such as DSPs, manage signal processing tasks. The co-design approach is ideal for SDR, but it comes with challenges like higher costs due to multiple components on a single board, complex memory sharing between processor and FPGA, and sophisticated interfaces.

2.4 Wireless Systems Concepts

This subsection provides an overview of essential wireless system concepts, focusing on key modulation techniques and performance evaluation criteria. It begins by introducing Quadrature Phase Shift Keying (QPSK) and Orthogonal Frequency Division Multiplexing (OFDM), two widely-used modulation schemes in modern wireless communication systems.

Following this, the discussion shifts to the performance metrics that are critical for assessing the efficiency and reliability of these systems. These concepts lay the groundwork for understanding how wireless communication systems operate and are optimized for various applications.

2.4.1 Quadrature Phase Shift Keying (QPSK) Modulation

Phase Shift Keying (PSK) is a broad class of digital modulation schemes widely used in the communication industry due to its effectiveness in transmitting data. In PSK, the phase of the carrier signal is altered according to the message data, rather than varying its amplitude or frequency. This approach is preferred in digital modulation as it offers greater resilience against signal degradation, providing better protection and reliability during transmission [54, 55].

A traditional approach is binary PSK (BPSK), in which a data bit is represented by a symbol. However, to increase the bandwidth efficiency, M-ary PSK modulation is often used, where $n = \log_2 M$ data bits are presented in one symbol [56]. A M-ary PSK signal of duration T can be defined as

$$s_i(t) = A\cos(2\pi f_c t + \theta_i), \quad 0 \leq t \leq T, \quad i = 1, 2, ..., M \tag{2.1}$$

where

$$\theta_i = \frac{(2i-1)\pi}{M}. \tag{2.2}$$

Considering the the orthogonal basis functions $\phi_1(t)$ and $\phi_2(t)$, the above expression can also be written as

$$s_i(t) = A\cos(\theta_i)\cos(2\pi f_c t) - A\sin(\theta_i)\sin(2\pi f_c t) \tag{2.3}$$

$$s_i(t) = s_{i1}\phi_1(t) + s_{i2}\phi_2(t)\ .$$

In quadrature phase shift keying (QPSK) M = 4, two bits are being transmitted per symbol. There are four possible cases 00, 01, 10, and 11, which correspond to the θ_i phase values $\frac{\pi}{4}$, $\frac{3\pi}{4}$, $-\frac{3\pi}{4}$, and $-\frac{\pi}{4}$. Eq. (2.3) can also be expressed in In-phase $I(t)$ and Quadrature $Q(t)$ components [54], as

$$s(t) = I(t)\cos(2\pi f_c t) + Q(t)\sin(2\pi f_c t)\ . \tag{2.4}$$

In a constellation diagram, QPSK-modulated IQ data is graphically represented as four distinct points positioned around the origin, each indicating the previously mentioned phase angles. The I axis runs horizontally, while the Q axis runs vertically, with each point corresponding to a specific I/Q pair. These points form a square pattern centered on the origin, with each symbol located 90 degrees apart [57]. This visual arrangement provides an intuitive way to monitor phase and amplitude variations, enabling a quick assessment of signal quality and any distortions in the modulated data.

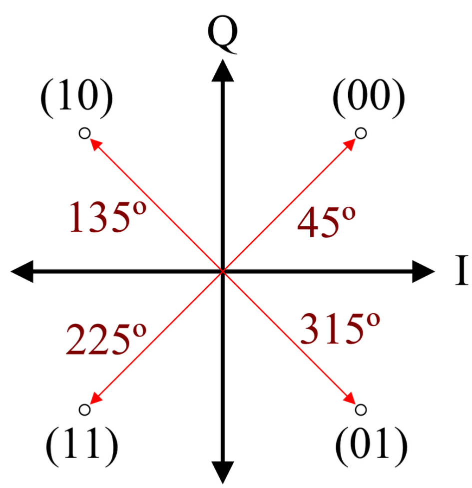

Figure 2.10: Typical constellation diagram for QPSK modulation, as presented in [57]. The IQ pairs are spaced 90°, representing θ_i = 45° ($\frac{\pi}{4}$), 135 ° ($\frac{3\pi}{4}$), 225° ($-\frac{3\pi}{4}$), and 315 ° ($-\frac{\pi}{4}$).

2.4.2 Orthogonal Frequency Division Multiplexing (OFDM) Modulation Scheme

In the digital signal domain, the information is transmitted in bits, or collections of bits called symbols, which are modulated onto the carrier [58]. Considering a simple single-carrier system, as the requirement for higher data rates, hence bandwidths, increases, the duration of one bit or symbol becomes smaller making the system more susceptible to loss of information. Frequency division multiplexing (FDM) accounts for this issue by using modulation by using multiple subcarriers within the same single channel so that the total data rate to be sent in the channel is divided between the various subcarriers.

In orthogonal frequency division multiplexing (OFDM), the information is split between several closely-spaced, narrowband subcarriers with the particularity that they are orthogonal [59]. For a subcarrier in OFDM to be orthogonal, it must be spaced from its adjacent, neighboring subcarrier(s) in such a way that the peak of each adjacent subcarrier falls exactly at its zero crossings [60]. Therefore, the use of multiple subcarriers allows for data to be sent in parallel rather than sequentially, where as the orthogonality between them allows for the subcarriers' spectra to overlap, increasing the spectral efficiency [58]. Additionally, each subcarrier can be modulated with a conventional digital modulation scheme, such as binary PSK, QPSK, quadrature amplitude modulation (QAM), etc. at a low symbol rate.

As previously discussed, OFDM takes advantage of multiple subcarriers to transmit data efficiently. However, to successfully map the received data between frequency and time domain, OFDM systems are implemented in practice using a combination of fast Fourier Transform (FFT) and inverse fast Fourier Transform (IFFT) blocks. [58]. Fig. 2.11 shows a simplified block diagram for the digital implementation of an OFDM system.

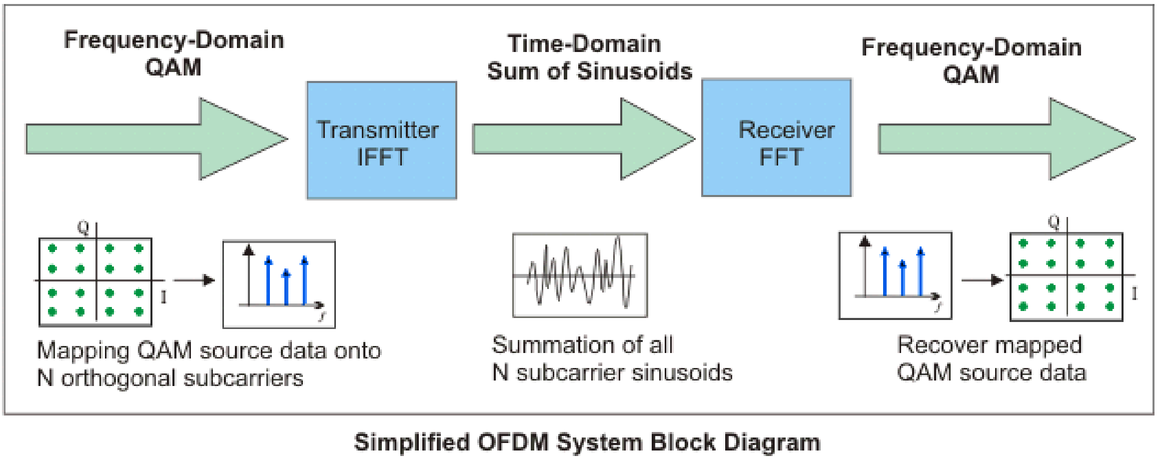

Figure 2.11: Simplified block diagram of an OFDM system digital implementation, as presented in [59].

The input data, consisting of complex numbers representing modulated subcarriers, are grouped and mapped to their respective modulation constellation points based on the chosen modulation scheme. The IFFT (Inverse Fast Fourier Transform) block then converts this frequency-domain data into a time-domain OFDM symbol, which is transmitted as an analog waveform [59]. The IFFT processes N_s source symbols, where N_s corresponds to the number of subcarriers, and each input symbol has a duration of T_s seconds. The symbols represent both amplitude and phase, corresponding to specific subcarriers, and the IFFT output is the sum of these sinusoids.

This process creates a single OFDM symbol from the block of output samples in the time domain. Then, guard intervals are inserted between each of the symbols to prevent inter-symbol interference, thus multiple symbols can be concatenated to create the final OFDM burst signal. After further processing, the time-domain signal is transmitted through the radio channel, and the FFT block at the receiver converts the signal back into the frequency domain to recover the original data. Fig. 2.12 illustrates the main characteristics of an OFDM signal and the just discussed relationship between the frequency and time domains.

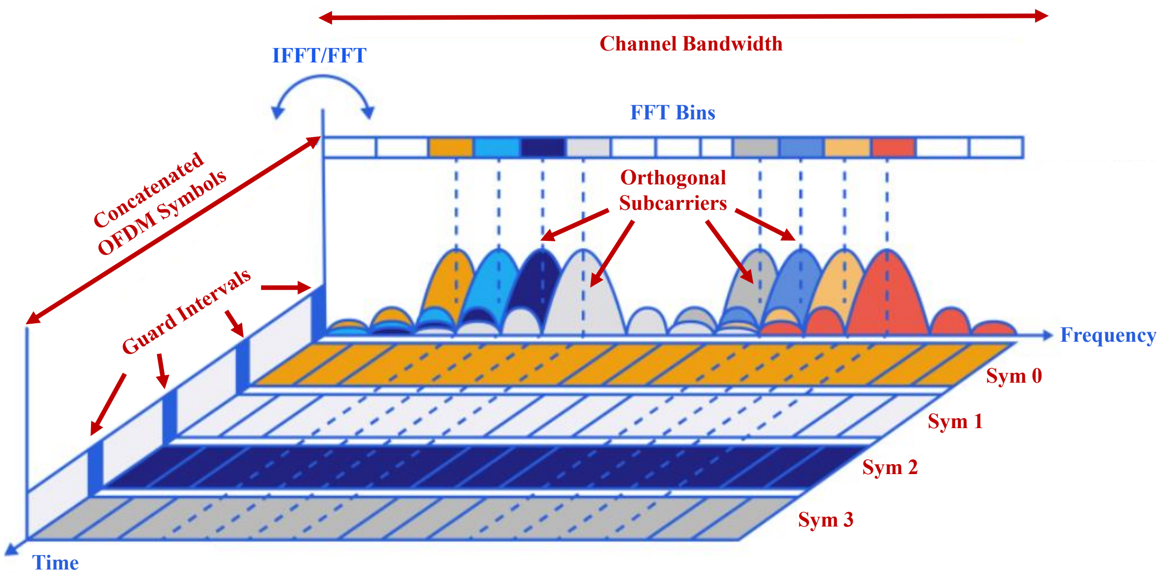

Figure 2.12: Frequency-time continuum showing OFDM symbols being binned, concatenated and transmitted sequentially, adapted from [60, 59].

OFDM offers several advantages in handling multipath distortion, which occurs when a radio signal reflects off obstacles like buildings or trees, causing interference at the receiver. Unlike single-carrier systems where multipath affects the entire signal, in OFDM, only some subcarriers may experience degradation, minimizing data loss and allowing for better recovery through error correction [60]. OFDM's use of FFT and IFFT simplifies implementation and improves spectral efficiency, while its ability to adapt power and modulation makes it ideal for integration with multi-antenna systems. However, OFDM has drawbacks, such as reduced spectral efficiency due to the need for a cyclic prefix and large sidelobes, high peak-to-average power ratio, and synchronization challenges, particularly in cellular networks [61].

2.4.3 Performance Metrics

Performance metrics for wireless systems are essential in evaluating the efficiency, reliability, and overall quality of communication networks. These metrics provide quantifiable measurements that assess how well a system can transmit data, manage interference, and maintain connection stability under various conditions. In this work, these metrics can also be used to evaluate how much the antenna choice for wireless transmitters and receivers can affect the overall system performance. Key performance indicators, such as bandwidth, signal strength, signal-to-noise ratio, and packet error rate, are commonly used to analyze system capabilities so the required standards for different applications are met [62].

Noise in wireless communication refers to any unwanted random disturbances that affect a signal during transmission. Signal-to-noise ratio (SNR) refers to the dimensionless ratio of the signal power P_{sig} to the noise power P_N [63]. This ratio is usually expressed in decibels as

$$SNR\,(dB) = 10\log_{10}\left(\frac{P_s}{P_N}\right)\,. \tag{2.5}$$

Expanding this concept to a spectrum-congested environment, a frequency-variant interferer can be introduced in Eq. (2.5), as follows

$$SINR\,(dB) = 10\log_{10}\left(\frac{P_s}{P_N + P_{I(i)}}\right) \tag{2.6}$$

where $P_{I(i)}$ is the power received from an interferer at a determined carrier frequency i. This magnitude is referred to as signal-to-interferer plus noise ratio (SINR)[64]. SINR measures the strength of the wanted signal compared to the unwanted interference plus noise, critical to maximizing data capacity and throughput for users in communication systems [65].

Furthermore, the SINR level can be associated with the successful reception of information. As previously mentioned, communication systems transmit information in bits. OFDM groups these bits into symbols, and a collection of symbols is referred to as a packet. The packet error rate (PER) metric measures the ratio of received packets with errors to the total number of transmitted packets [66]. For a packet of n bits, PER_n can be defined as

$$PER_n = 1 - (1 - P_b)^n \tag{2.7}$$

where P_b is the bit error rate. Therefore, the PER can be measured based on packets alone or through bit error estimation, depending on the system's capabilities or setup.

2.5 Summary

This chapter provided an overview of the essential concepts for understanding the scope of this work, beginning with reconfigurable antennas, defined as antennas that adjust frequency, radiation pattern, or polarization. Tuning techniques were categorized by principle: electrical, optical, mechanical, and material-based. Reconfigurable frequency-filtering antennas, which combine radiation and frequency functionalities, are especially relevant for CR applications due to their channel selectivity and OOB rejection.

The discussion then covered systems benefiting from these antenna properties, highlighting SDR for its adaptability via software-defined protocols and cognitive algorithms. Common modulation schemes were introduced, with QPSK noted for its efficiency in transmitting two bits per symbol by embedding information in the signal phase. OFDM was also highlighted for its spectrum efficiency through orthogonal subcarriers. Finally, SNR and SINR were highlighted as key metrics for assessing performance in modern wireless systems, while PER serves as a valuable indicator of successfully received information.

Chapter 3

Experimental Setup

As discussed in the previous sections, reconfigurable and reconfigurable filtering antennas enable aperture-level selectivity in congested spectrum environments. However, the limited available literature on reconfigurable antennas integrated into SDR-based systems (see Table 1.1) does not provide a comprehensive analysis of how antenna selection affects system performance in spectrum-congested environments. Consequently, the potential advantages of reconfigurable antennas over traditional broadband antennas may be overlooked from a system perspective.

Therefore, to effectively evaluate the performance of a given antenna type in CR solutions, its integration with an SDR platform and its functionality as a receiver unit must be assessed under realistic spectrum-congested environments. Although several advantages of reconfigurable antennas have been discussed in Chapter 2, this work focuses on frequency tunability as a first approach to assessing reconfigurability performance, with the proposed SDR-based testbed enabling future analysis of polarization and pattern reconfigurability under the same conditions.

This chapter outlines the experimental framework established to achieve said conditions. It begins by defining the scenario and the relevant variables critical to the experiments, particularly to the controlled congested spectrum environment. Then, a detailed description of the system architecture is broken down into key components, such as the antennas under test, hardware specifications, and software configurations employed throughout the measurement process. Finally, the setup for the measurements is discussed, offering a clear description of how the system was spatially arranged. The chapter concludes with a summary, emphasizing the main components and their roles in supporting the experimental objectives.

3.1 Scenario and Variable Definition

This study considers one transmitter (Tx) node, one receiver (Rx) node, and one interference node, with spectrum congestion emulated by introducing a frequency-variant interferer. The Tx and Rx nodes are defined as the main user connection that will be under test.

The information embedded in the signal will be transmitted at a specific data rate, which requires the Tx and Rx nodes to have a certain minimum sampling rate to accurately recover the signal. Both the Tx and Rx nodes are configured to operate at a sampling rate of SR_{Tx} and SR_{Rx}, respectively. In the context of this study, the SR will directly determine the Tx and Rx hardware bandwidths due to the SDR's anti-aliasing filter [67]. The defined receiver bandwidth will be referred to as β_{Rx}, and signals outside this bandwidth will be considered unwanted.

Fig. 3.1 shows a Tx QPSK-modulated signal with a β_{sig} bandwidth transmitted at a center carrier frequency f_{sig}. The performance of the receiver is evaluated in a β_T test bandwidth, larger than the receiver bandwidth β_R allowing for evaluation of the out-of-band (OOB) interference rejection for each antenna type.

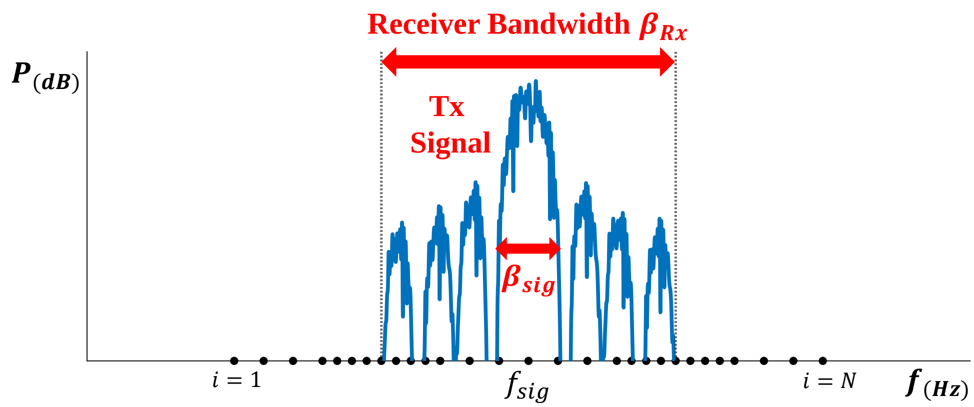

Figure 3.1: Tx signal power in dB over frequency for a QPSK-modulated signal of β_{sig} bandwidth transmitted at a center carrier frequency f_{sig}. The presented power spectrum is shown between the desired receiver bandwidth β_{Rx}.

For the interference node, the transmitted signal could be either a tone (continuous sinusoidal wave at a fixed frequency) or a QPSK-modulated signal. The QPSK-modulated case presents a β_{int} bandwidth, which relates to the Tx signal through the interference-bandwidth-to-signal-bandwidth ratio $BWR = \beta_{int}/\beta_{sig}$. The modulated interferer signal is then upconverted to the interferer carrier frequency $f_{int(i)}$ before transmission. Note that $f_{int(i)}$ varies discretely across a test frequency span ($f_{sig} \pm \beta_T/2$), where $i = 1, 2, ..., N$ and N is the total number of carrier frequencies. Fig. 3.2 illustrates the described interference signal as well as the discrete carrier frequency point. The spacing between the carrier frequencies around the receiver band edges is closer together for a more precise evaluation.

Each of the nodes has a certain gain applied to the transmitted or received signal: the Tx signal gain G_{Tx}, the Rx signal gain G_{Rx} and the interferer signal gain G_{int}. Contemplating a scenario with fixed G_{Tx} and G_{Rx}, the interference level perceived by the main users will be determined by the transmitted power and proximity of the interference node. Nevertheless, in order to emulate channel gain characteristics of the interferer, rather than physically moving the antennas, the interference signal gain G_{int} was varied.

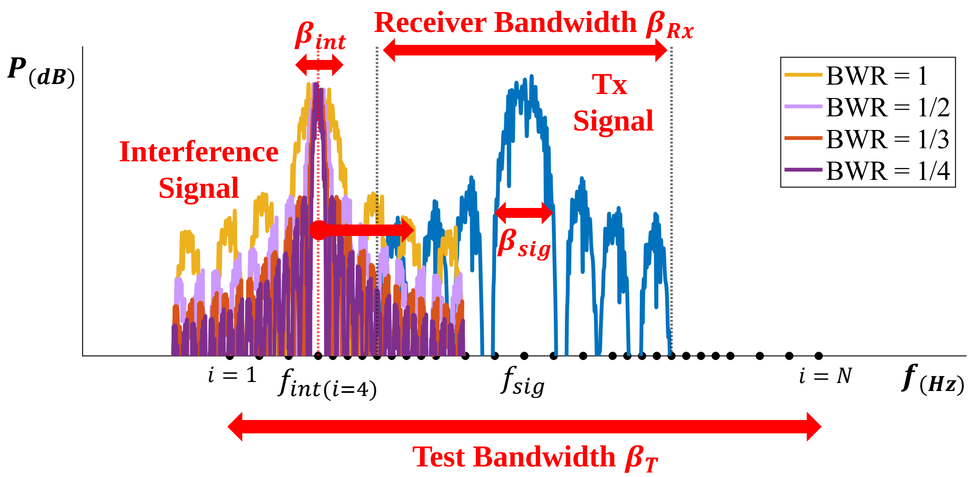

Figure 3.2: Tx and interference signal power in dB over frequency for a QPSK-modulated signal. The interferer signal has a variable bandwidth β_{int} that affects the sidelobe level of the generated signals as shown in the traces for BWR = 1, 1/2, 1/3, 1/4.

The performance analysis presented in this study was conducted around a Tx/Rx center frequency of 2.3 GHz for its wireless communication service [68] and amateur radio applications. Consequently, the signal carrier frequency was f_{sig} = 2.3 GHz for a Tx QPSK-modulated signal with a fixed $\beta_{sig} = 10MHz$ and G_{sig} = 40 dB. The test bandwidth β_T was set to 80 MHz, i.e. the interference carrier frequency $f_{int(i)}$ varies from 2.26 to 2.34 GHz for N = 29 discrete frequency points with varying BWR values of 1, 1/2, 1/3, and 1/4, and G_{int} of 30, 40, 50 and 60 dB. The received interference power $P_{int(i)}$ at 2.3 GHz is measured and averaged for each of the interference carrier frequency points considering a receiver gain G_{Rx} = 40 dB and a receiver bandwidth β_R = 40 MHz.

The congested spectrum variables, along with their descriptions and selected values, are presented in Table 3.1. This analysis aims to evaluate the system's performance under various interference conditions, providing insights into its robustness and adaptability. Additionally, the choice of frequency range aligns with practical scenarios, enhancing the study's relevance to real-world applications.

Table 3.1: Defined variables for the test scenario

Variable	Description	Assigned Value
β_{Rx}	Rx bandwidth	40 MHz
β_{sig}	Tx signal bandwidth for a QPSK-modulated signal	10 MHz
f_{sig}	Tx/Rx signal carrier frequency (center frequency)	2.3 GHz
β_{int}	Interferer signal bandwidth for a QPSK-modulated signal	[10, 5, 3.3, 2.5] MHz
$BWR = \beta_{int}/\beta_{sig}$	Interference-bandwidth-to-signal-bandwidth ratio	[1, 1/2, 1/3, 1/4]
$f_{int(i)}$, $i = 1, 2, ...N$	Interferer signal carrier frequency	N = 29
β_T	Test bandwidth	80 MHz
$f_{sig} \pm \beta_T/2$	Test frequency span	2.26 - 2.34 GHz
G_{sig}	Tx signal gain	40 dB
G_{int}	Interferer signal gain	[30, 40, 50, 60] dB
G_{Rx}	Rx signal gain	40 dB

3.2 System Architecture

The implementation of the discussed scenario was achieved through the integration of different hardware platforms. Figure 3.3 provides an overview of the proposed SDR-based test system designed to emulate the congested spectrum environment scenario. The Tx and interference nodes are situated on one side, whereas the Rx node is positioned on the opposite side. Both sides contain the same three basic components: a controller computer, an SDR platform, and an antenna.

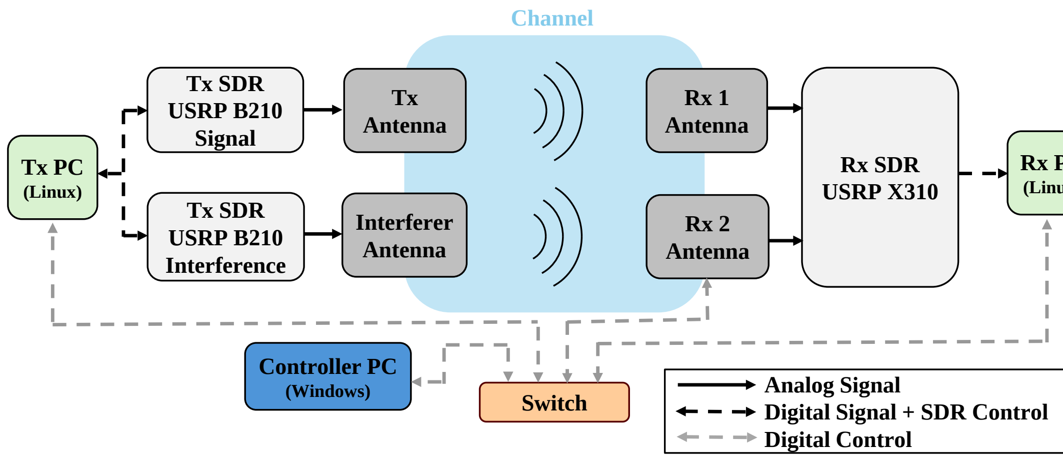

Figure 3.3: SDR-based testbed architecture designed to emulate the congested spectrum environment scenario. The system is divided into two main sides: the Tx-Interferer side and the Rx side. Each side consists of computer, SDR, and antenna blocks that can exchange analog, digital, or digital control information.

One main difference between the two sides is that the Tx and interference antennas are connected to independent SDR platforms, although both are the same model. On the receiver side, however, a dual-channel SDR is used to allow two receiver antennas to be connected to the same platform for comparison. In this case, the Rx_1 antenna remains the same throughout all the measurements as a control indicator.

All components in the SDR-based testbed are connected in some way to each other. The antennas and SDR platforms are directly connected and exchange analog signals. At the same time, the Tx and Rx computers, or PCs, are directly connected to their respective SDRs, allowing for SDR control and digital signal processing. Finally, each computer is connected to a network switch, which allows for a third computer to be introduced as the controller PC, automating the measurement process with server-client functionalities. Additionally, this third computer is also used for the reconfigurable antenna tuning process.

3.2.1 Antenna Specifications

The antennas for the Tx and interference node will remain constant throughout all the measurements. For the Tx antenna, a SATIMO Dual Ridge Horn SH2000 antenna was used. This antenna is rated for a 2 to 32 GHz frequency coverage, and its gain at 2.3 GHz is approximately 2.3 GHz [69]. On the other hand, a vertical antenna by Molex [70] was used for the interference node. The Tx antenna is shown in Fig. 3.4.

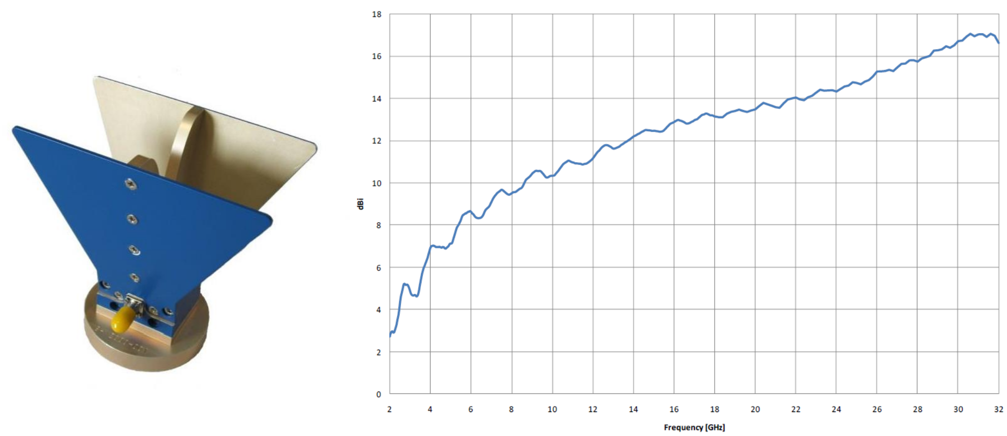

Figure 3.4: SATIMO Dual Ridge Horn SH2000 [69] used as the Tx node antenna (left) and its typical boresight gain over frequency (right).

The SATIMO horn antenna was selected due to its superior performance in gain at the defined center frequency. Several units of the Molex vertical antenna were purchased for this project. As part of the characterization process, the gain of three of these antennas was measured, and the results are shown in Fig. 3.5. It can be observed that all of them are below 0 dB and exhibit oscillation throughout the frequency range of interest in this work. Vertical A was used as the interferer antenna, while Vertical C was selected as one of the receivers and will be referred to as the "Vertical" antenna from now on.

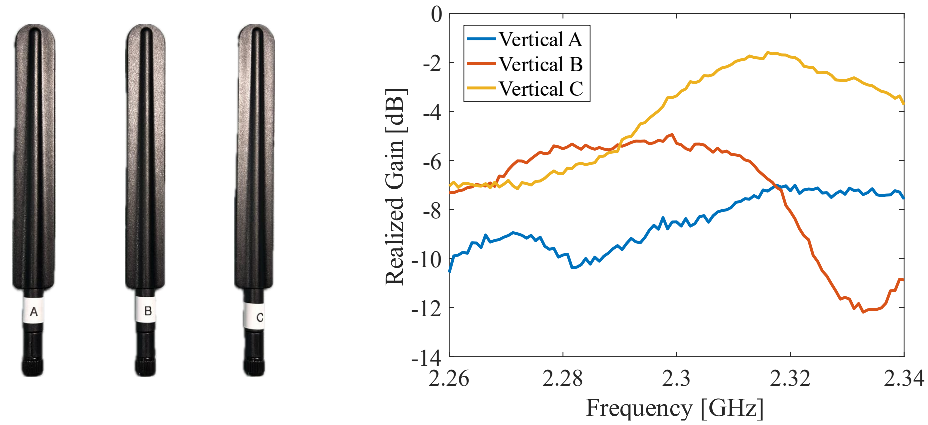

Figure 3.5: Molex vertical antenna [70]gain characterization. Three selected units of the Molex vertical antenna (left) labeled ‘A’, ‘B’ and ‘C’ with their corresponding measured realized gain over the frequency range of interest (right).

Narda-ATM
150-441EM-NF
‘Horn’

Molex Vertical Antenna
‘Vertical’

Cavity-backed Slot
Reconfigurable Antenna
‘Reconfigurable’

Cavity-backed Slot
Reconfigurable Filtenna
‘Filtenna’

Figure 3.6: Receiver antennas under test. From left to right: Narda-ATM wide band horn antenna 150-441EM-NF [71] as ‘Horn’, Molex vertical antenna [70] as ‘Vertical’, SIW cavity-backed slot reconfigurable antenna [72] as ‘Reconfigurable’, and SIW cavity-backed slot reconfigurable filtenna [73] as ‘Filtenna’.

Four different antenna types will be evaluated as receiver antennas, as shown in Fig. 3.6. The “Horn” antenna selected for these measurements is the Narda-ATM wideband horn antenna model 150-441EM-NF [71], with a gain of 13.72 dB at 2.3 GHz. The “Vertical” antenna has already been introduced and characterized. And the “Reconfigurable” antenna is the evanescent-mode substrate integrated waveguide (SIW) cavity-backed slot antenna described in [72].

Reconfigurability is achieved through the loading of a metal post in the center of the SIW cavity. A conductive tuning plate on top of the metal post is moved by an M3-L long-range linear actuator [74], which has a maximum range of 6 mm and is controlled with the provided New Scale Pathway software [75] that allows for 0.5 μm steps. The "Filtenna" operates under the same principle but adds an extra resonator to achieve a second-order filter response, as presented in [73]. The band-pass filter specifications for the "Filtenna" synthesis design were a 1.5% fractional bandwidth, meaning that for a 2.3 GHz center frequency, it would present a 34.5 MHz bandwidth. The tuning mechanism elements, as well as the "Filtenna" structure, are shown in Fig. 3.7.

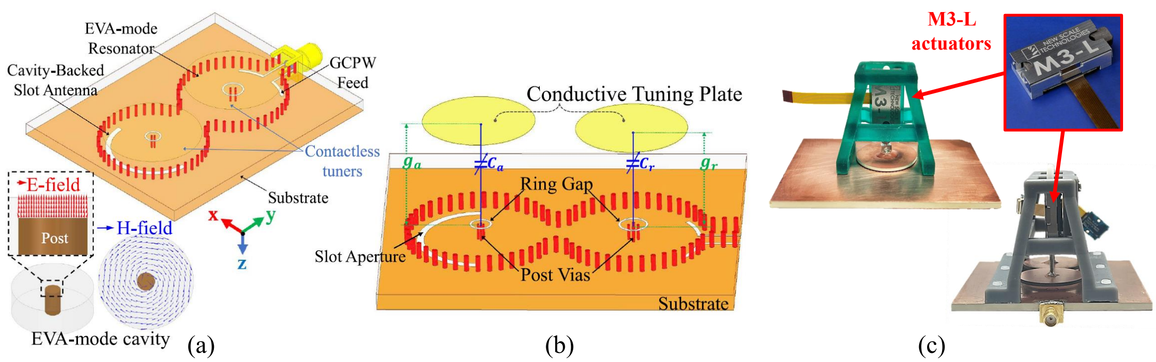

Figure 3.7: 'Filtenna' 3D structure with contactless tuning scheme, adapted from [72] and [73].(a) 3D structure of the 'Filtenna' showing the electric and magnetic fields of the basic evanescent mode cavity. (b) contactless capacitive tuning scheme. (c) The tunning mechanism implemented in both the 'Reconfigurable' antenna and 'Filtenna'.

The intention behind selecting these specific antenna types was to cover a wide range of antenna characteristics, including gain, bandwidth, directivity, and size. Fig. 3.8 shows the measured radiation patterns considering linear vertical polarization for each of the antennas under test at 2.3 GHz. Among the selected antennas the "Horn" presents the most directive radiation pattern in Fig. 3.8(a). On the other hand, the selected "Vertical", "Reconfigurable" and "Filtenna" antennas exhibit rather omnidirectional patterns.

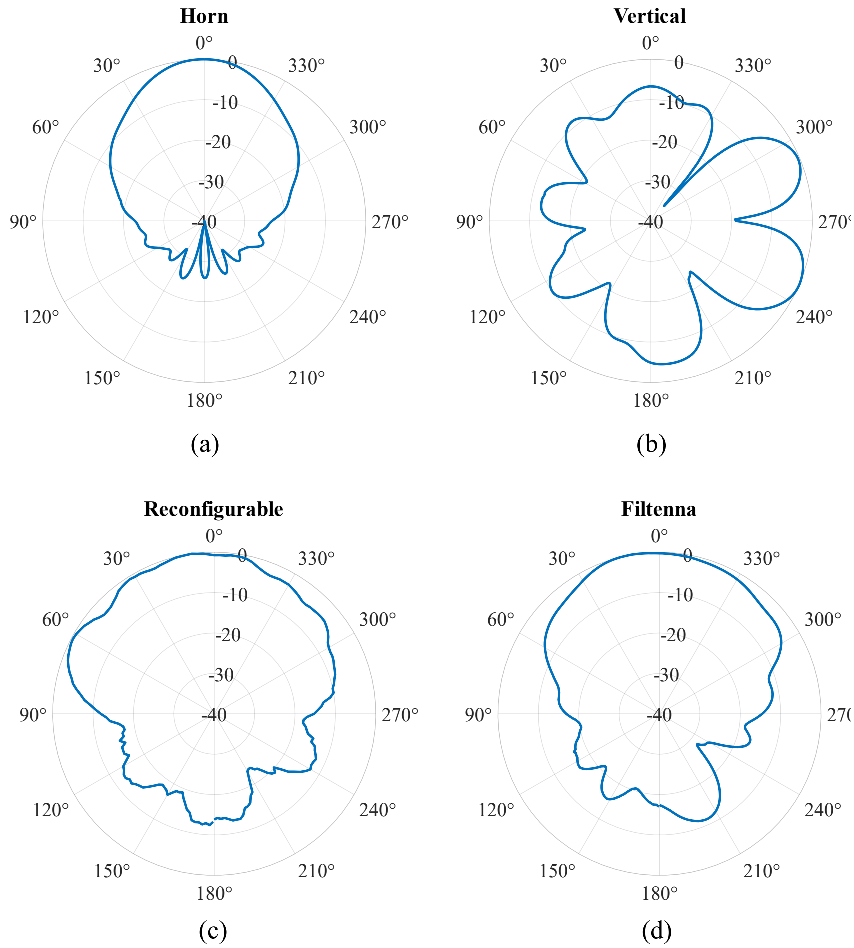

Figure 3.8: Normalized measured radiation patterns for the antennas under test considering linear vertical polarization at 2.3 GHz: (a) “Horn”, (b) “ Vertical”, (c) “Reconfigurable”, and (d) “Filtenna”.

Both the “Horn” and “Vertical” antennas are broadband antennas with almost constant realized gains over the defined test frequency span (2.26 to 2.34 GHz), as seen in Fig. 3.9. The “Reconfigurable” antenna is a narrowband antenna, and as such, it presents a slight improvement in gain within its bandwidth of operation (12 MHz). However, the “Filtenna” response shows the OOB rejection characteristic of the BPF synthesis.

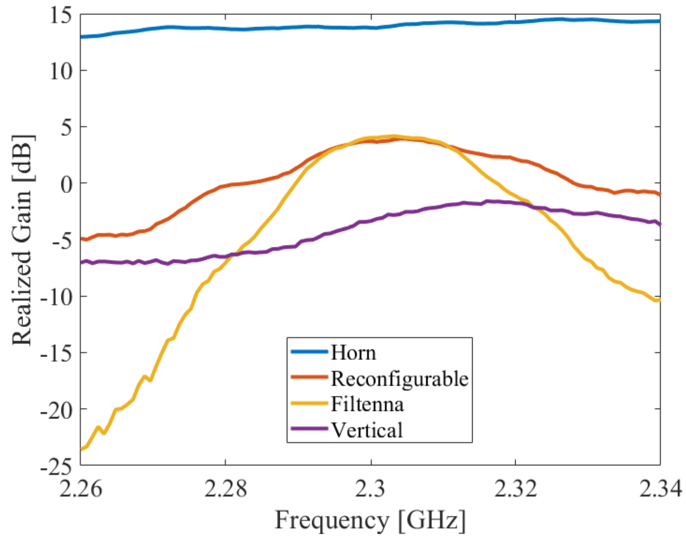

Figure 3.9: Measured realized gain over frequency for each receiver antenna under test: "Horn", "Vertical", "Reconfigurable", and "Filtenna".

The "Horn" can be considered a high-gain antenna, with a gain of 13.72 dB at 2.3 GHz. Almost, 10 dB higher than the "Reconfigurable" and "Filtenna" values. However, its electrical size is also larger, measuring 2.59 $\times$ 3.02 $\times$ 3.47 λ_0, where $\lambda_0 = (3 \times 10^8)/f_{sig}$. Table 3.2 provides a comparison of all the antennas discussed in this section. The main three characteristics are broadside realized gain at 2.3 GHz, -10 dB bandwidth, and size in terms of λ_0. These parameters will be considered in the performance analysis and possible application requirements.

Table 3.2: Antenna Under Test Specifications

Antenna	Gain (dB)	Bandwidth (MHz)*	Size (λ_0) †
Horn	13.72	1500	2.59 x 3.02 x 3.47
Vertical	< 0	980	1.23 x 0.15 x 0.23
Reconfigurable	3.99	12.8	0.37 x 0.39 x 0.38
Filtenna	3.68	17.4	0.41 x 0.64 x 0.40

* The bandwidth specified in this table is the -10 dB return loss bandwidth.
† Guide wavelength, λ_0, is approximately calculated at the center operating frequency f_{sig}.

3.2.2 Hardware Specifications

Once the antennas for each node were defined, the appropriate SDR platform for each node was selected, taking into account the available space and the setup distribution. First, the specifications of each selected SDR platform will be discussed. Then, the connections between the SDR platforms and their respective computers, as well as the interconnectivity among all nodes, will be explained. The hardware limitations of each component and connection will also be addressed.

The Universal Software Radio Peripheral (USRP) is an SDR platform developed by Ettus Research from National Instruments, that combines general purpose processors (GPPs), field-programmable gate arrays (FPGAs), and RF front-ends for rapid prototyping and design [50]. In the proposed architecture, the transmitter signal and interference nodes use USRP B210, while the receiver side uses USRP X310.

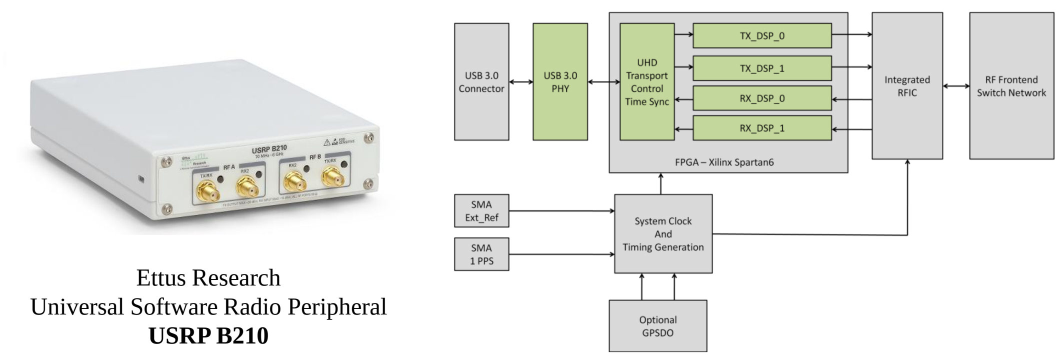

Figure 3.10: Ettus Research USRP B210 block diagram, adapted from [76]

The USRP B210 covers a range of frequencies from 70MHz to 6 GHz, has a Spartan6 XC6SLX150 FPGA, and USB 3.0 connectivity [76]. The USRP B210 offers two receive and two transmit channels, incorporating a larger FPGA, general-purpose input/output (GPIO) ports, and an external power supply. They can stream up to 56 MHz of instantaneous bandwidth in the 1 Tx and 1 Rx configuration, and 30.72 MHz for the 2 Tx and 2 Rx configuration. Equipped with a 12-bit ADC and DAC, allows for 61.44 MS/s. The USRP B210 presents a -20 dBm IIP3 and a receive noise figure $<$ 8 dB. Fig. 3.10 shows the USRP B210 enclosure and its block diagram. The block diagram shows the main FPGA block with its respective Tx and Rx channels, the RF integrated circuit and front-end switch network, as well as the system clock block, USB 3.0, and SMA connections. Additionally, there is an optional GPS disciplined oscillator, that integrates a GPS receiver and a high-quality, stable oscillator.

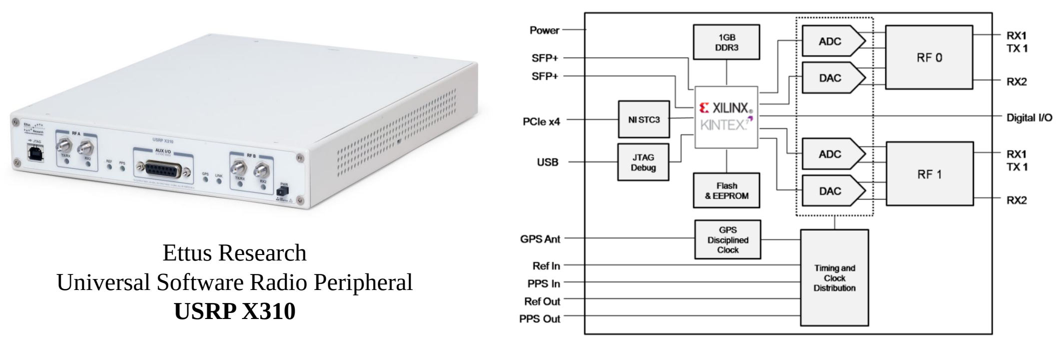

Figure 3.11: Ettus Research USRP X310 block diagram, adapted from [77]

The Ettus Research USRP X310 [77] high-performance, SDR platform that combines two extended bandwidth daughterboard slots covering DC to 6 GHz with up to 160MHz of baseband bandwidth. It presents multiple high-speed interface options like dual 1/10 gigabit Ethernet and a large user-programmable Kintex-7 FPGA. Fig. 3.11 shows the block diagram for the USRP X310. The ADC has a 14-bit resolution with a maximum sampling rate of 200 MS/s, while the DAC has a 16-bit resolution with a maximum sampling rate of 800 MS/s. The receiver IIP3 is 8-13 dBm with a noise figure $<$ 5 dB from 50 MHz to 4 GHz.

According to the available interface options for each USRP model, they were connected to their respective computers. Since the Tx and interferer nodes can be at a greater distance from each other than the two Rx antennas, the USRP B210 model was selected for the transmitter nodes due to its smaller size and unit availability (two units). These are connected to the Tx PC via a USB 3.0 connection, with a maximum speed of 5000 Mbits/s. On the receiver side, the X310 was used since it is larger, and its channels allow for greater capacity using the dual-channel configuration. Additionally, having both antennas on a single SDR platform allows for a fairer comparison. In this case, the 10 Gigabit Ethernet interface was used to connect the USRP X310 to the Rx PC, using an ethernet to USB-C converter. The three PCs were connected with 1 Gigabit Ethernet cables to a network switch. Thus, two networks were defined: one between the Rx PC and the USRP X310, and the other between the three PCs. Fig. 3.12 shows the respective IP addresses assigned for proper communication between devices.

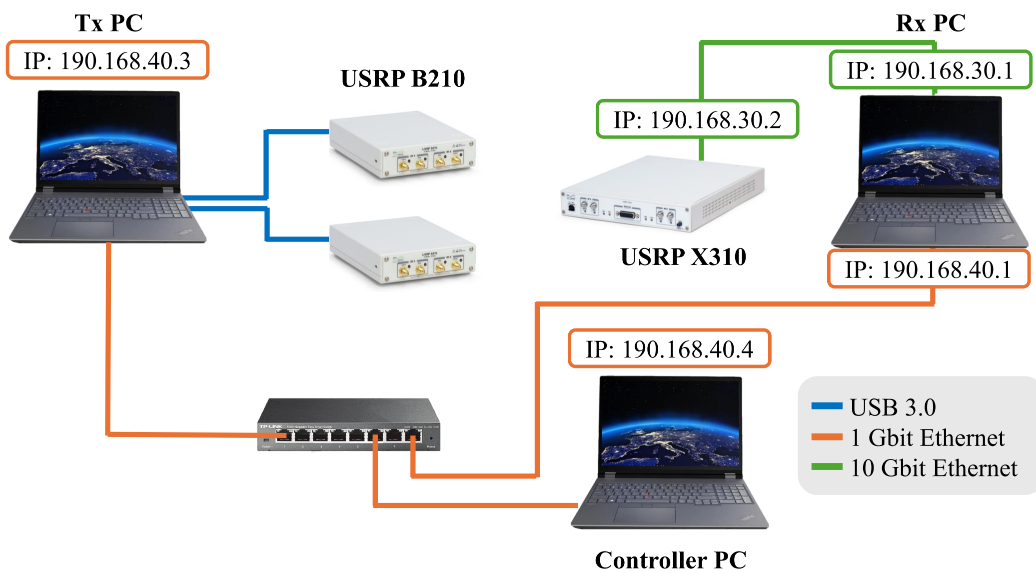

Figure 3.12: Connection diagram between USRP and PC devices. The USRP B210s were connected through USB 3.0, whereas the USRP X310 was connected to the Rx PC to a 10 Gigabit Ethernet link. The Tx, Rx and Controller PCs were connected to a network switch with 1 Gigabit Ethernet cables. IP addresses were assigned for all three computers, and for the particular USRP X310 and Rx PC subnetwork. All computers are represented as [78].

3.2.3 Software Configuration

This subsection presents the tools used to implement SDR functionalities on the USRP platforms, detailing the specific Tx and Rx functionalities and the integration of previously introduced variables. Next, the steps for the proposed measurements are then outlined, followed by the implementation of the automation code.

The SDR properties were implemented in the USRP platform through GNU radio, a free and open-source software toolkit for building software radios [44, 79]. It includes a wide library of signal-processing blocks originally coded in C++, which facilitates interprocess communication and data transfer from the real-time C++ flow graph to Python scripts. Both Linux computers on the transmitter and receiver sides execute GNU Radio flowgraphs. The Tx flowgraph generates QPSK-modulated signals for both signal and interference and sends them to their respective USRPs for upconversion and transmission. Fig. 3.13 shows the main blocks for the initial GNU radio flowgraph setup on the Tx-Interferer side.

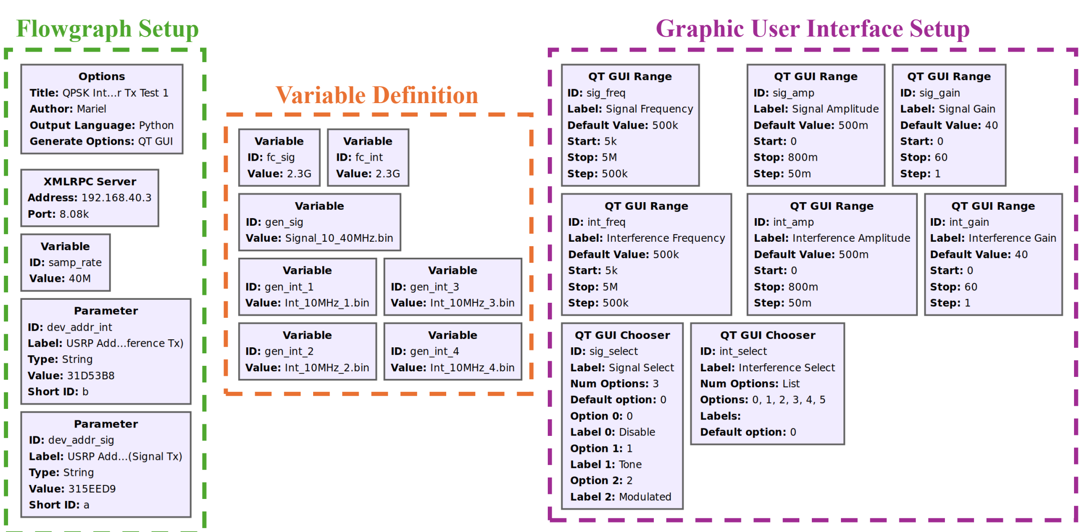

Figure 3.13: Main blocks of the Tx-Interferer-side GNU Radio flowgraph setup. The flowgraph configuration is done in the flowgraph setup section (XMLRPC Server IP address, sampling rate, USRP device address). The variable definition section integrates the proposed congested spectrum scenario parameters. The graphic user interface section was implemented for an easier test and debug process.

First, the basic configuration parameters, such as the XMLRPC server IP address, sampling rate, and USRP device addresses. The XMLRPC server allows running, starting, and stopping the flowgraph remotely, as well as providing access to variable callbacks, i.e. updating variable values remotely [80]. In this flowgraph, set variables only available through remote access are the signal carrier frequency 'fc_sig' (f_{sig}), the interferer carrier frequency 'fc_int' (f_{int}), and the data files of the modulated data for the different BW values for a QPSK-modulated signal. The rest of the variables were defined within the graphic user interface (GUI), although they are still accessible from the XMLRPC server, for easier testing and debugging of different scenarios. These variables include 'sig_gain' (G_{Tx}), 'int_gain' (G_{int}), 'sig_select' and 'int_select'.

The 'sig_select variable' is used to switch the status of the signal node between three states: not transmitting or off (0), a continuous sinusoidal waveform or tone (1), and a 10-MHz QPSK-modulated signal (2), through a selector block. Figure 3.14 shows the implementation of this block in the GNU Radio flowgraph. It can be seen that the output of the selector block connects to two destinations. The first is the GUI Frequency Sink, which allows the visualization of the signal in the time domain, while the second is the USRP Sink, which transmits the information to the USRP hardware at the specified address.

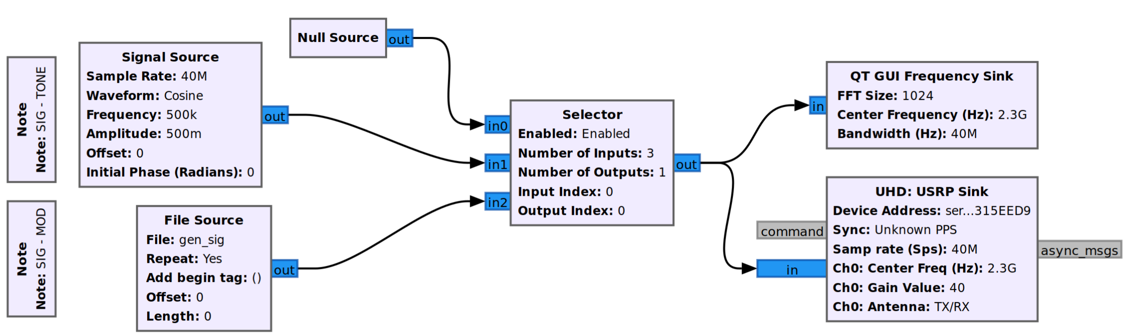

Figure 3.14: Selector block for the Tx signal transmission options: (0) Off, (1) Tone, and (3) 10-MHz QPSK modulated signal.

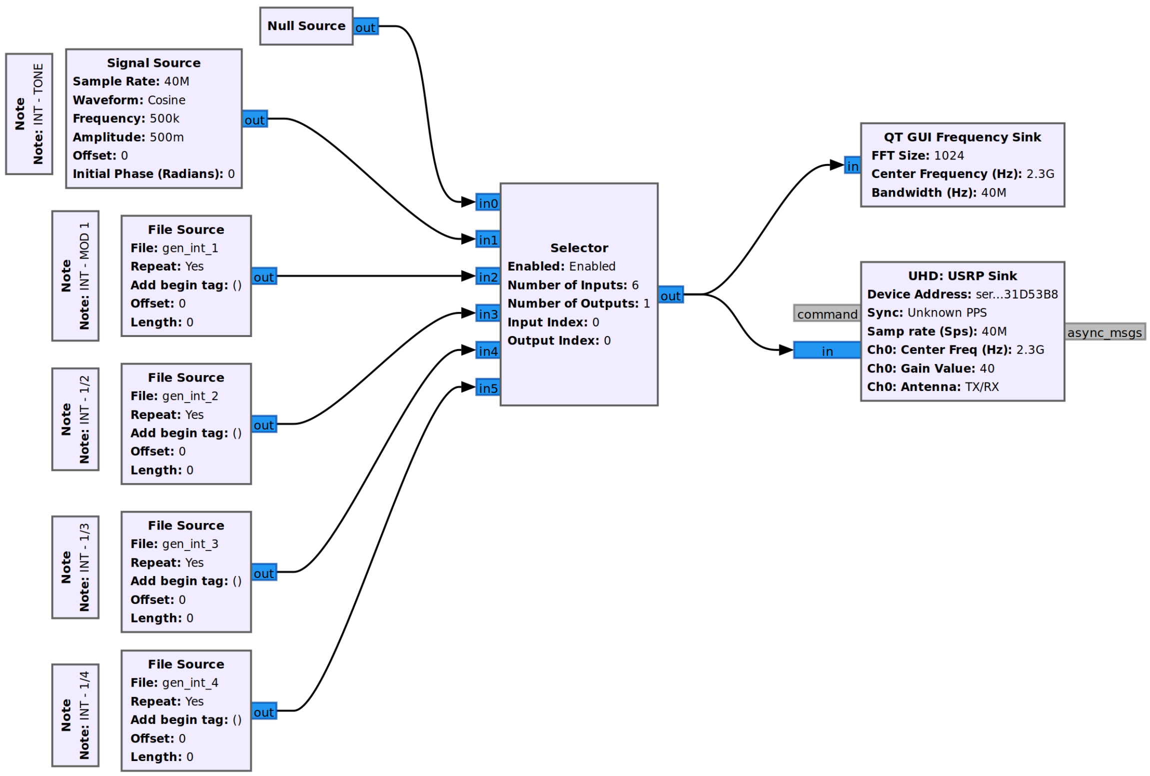

Figure 3.15: elector block for the interferer signal transmission options: (0) Off, (1) tone, QPSK-modulated signals with (2) BWR = 1, (3) BWR = 1/2, (4) BWR = 1/3, and (5) BWR = 1/4.

Similarly, the interference signal transmission is done with a USRP Sink block connected to a selector block. Fig. 3.15 shows the six possible options for the interference signal: (0) Off, (1) tone, QPSK-modulated signals with (2) BWR = 1, (3) BWR = 1/2, (4) BWR = 1/3, and (5) BWR = 1/4. Note that all QPSK-modulated signal data for the Tx and interference options has been previously stored in local files, for easier access and lower computational cost at the selected sampling rate.

The Rx GNU Radio flowgraphs focus on receiving data and calculating the average received power for each case. For remote reconfigurability and data transfer, the XMLRPC server IP address is defined, and the same sampling rate as the transmitters is used. In this setup, the USRP X310 is employed with its corresponding device address. However, a carrier frequency and gain value must be specified for each channel. Figure 3.16 shows these variables as 'fc_1' and 'fc_2' for the carrier frequencies, and 'sig_gain_1' and 'sig_gain_2' for their respective gains. A USRP Source block is used to access the data received by both channels of the USRP X310, as shown in Figure 3.17. The USRP receives and downconverts the signal, followed by a Remove DC Spike block to ensure consistency at the center frequency.

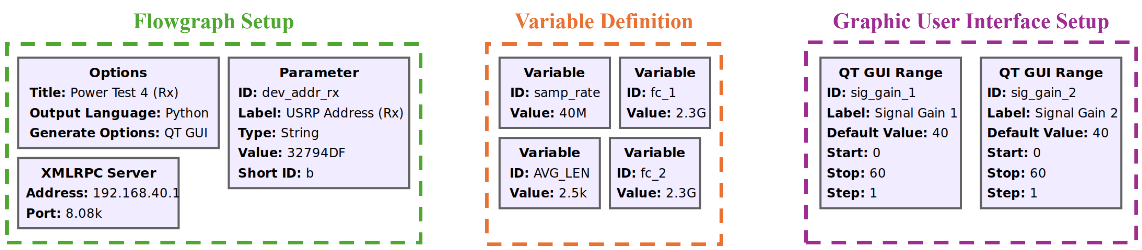

Figure 3.16: Main blocks of the Rx GNU Radio flowgraph setup. In the variable definition section, the carrier frequencies for each channel and the number of samples to average are defined.

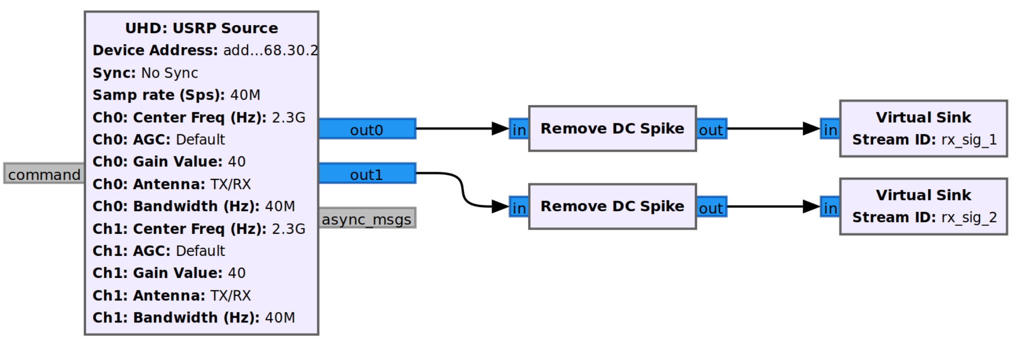

Figure 3.17: USRP Source block in its two-channel configuration followed by a removed DC spike block for consistent power calculations at the center frequency.

Once the data have been downconverted, the complex values of the signal are converted to magnitude, and the average of a specified number of samples is calculated. This value is then sent to a ZMQ PUB Sink, which transmits data that can be received by one or more subscribers [81]. Different ports are used for each channel. Figure 3.18 shows the process, along with additional GUI blocks used to visualize the received signal in real-time.

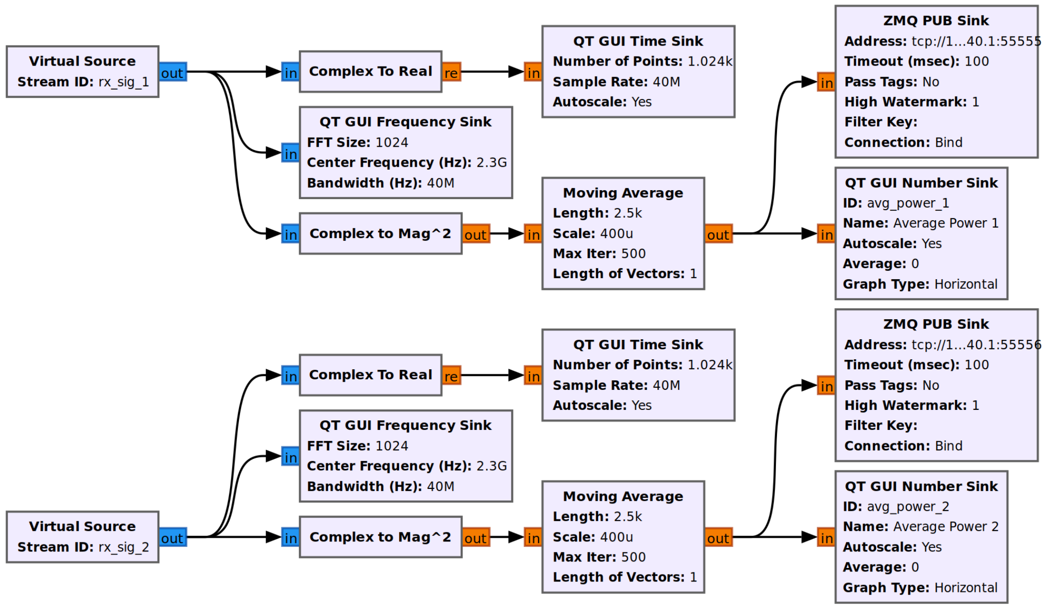

Figure 3.18: Received signal average power calculation in the Rx GNU radio flowgraph. The ZMQ PUB sink allows for the transmission of data to a remote subscriber.

These flowgraphs are set up and run on each of the computers on the Tx-interferer and Rx sides and were developed in collaboration with Dr. Michael B. Rahaim from the University of Massachusetts Boston, MA. The controller Windows computer runs a Python script that determines the sequence of measurements, controlling the flowgraphs through an XMLRPC connection and reading the data through a ZMQ subscription. Figure 3.19 shows the initial section of the flow diagram that the Python script follows to automate the power measurements. The first steps involve defining the XMLRPC and ZMQ connections. Then, the desired interference cases must be specified, i.e., β_T and N to define the discrete carrier frequency points, BWR, and/or G_{int}. Additionally, a number of iterations, N_m, per scenario need to be set to obtain an additional average.

The noise power, P_n, was first measured by turning off both the Tx and interference signals, setting both 'int_select' and 'sig_select' to 0. Next, the received Tx signal power, P_{sig}, was measured by activating the signal node with 'sig_select' = 2, corresponding to a 10-MHz QPSK-modulated signal. Both P_n and P_{sig} values were recorded for later use.

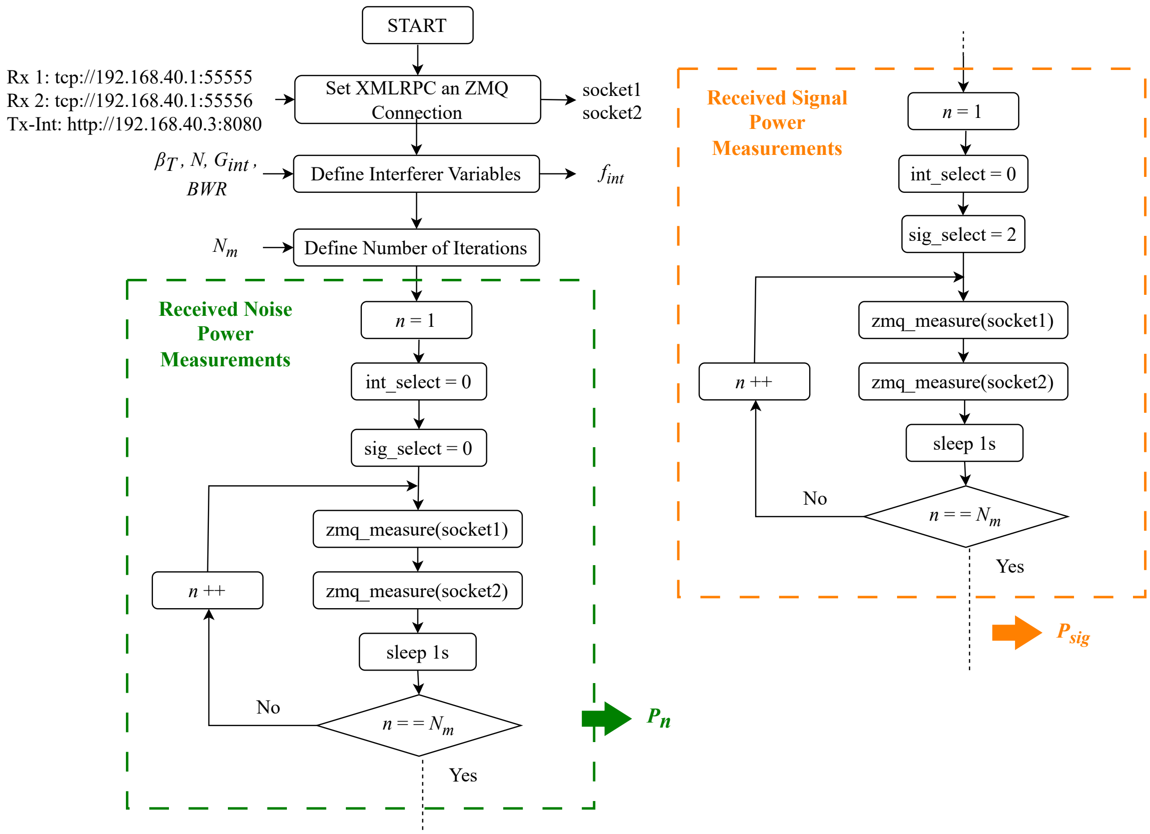

Figure 3.19: Python script flow diagram for the automation of power measurements with the proposed SDR-based testbed. Part 1.

Subsequently, the Tx signal was turned off, and the interference node began transmitting. For each combination of G_{int} and β_{int}, the interferer swept across the defined β_T frequency range. These parameters were updated by the Python script via the XMLRPC connection with the Tx-Interferer flowgraph. For each unique set of parameters, the script ran N_m iterations, averaging the received interference power. The averaged interference power, $P_{int(i)}$, was then saved in a CSV file, along with the parameter combinations and the previously recorded P_n and P_{sig} values. Further analysis was conducted to extract wireless system performance metrics, such as SINR, which will be discussed in Chapter 4.

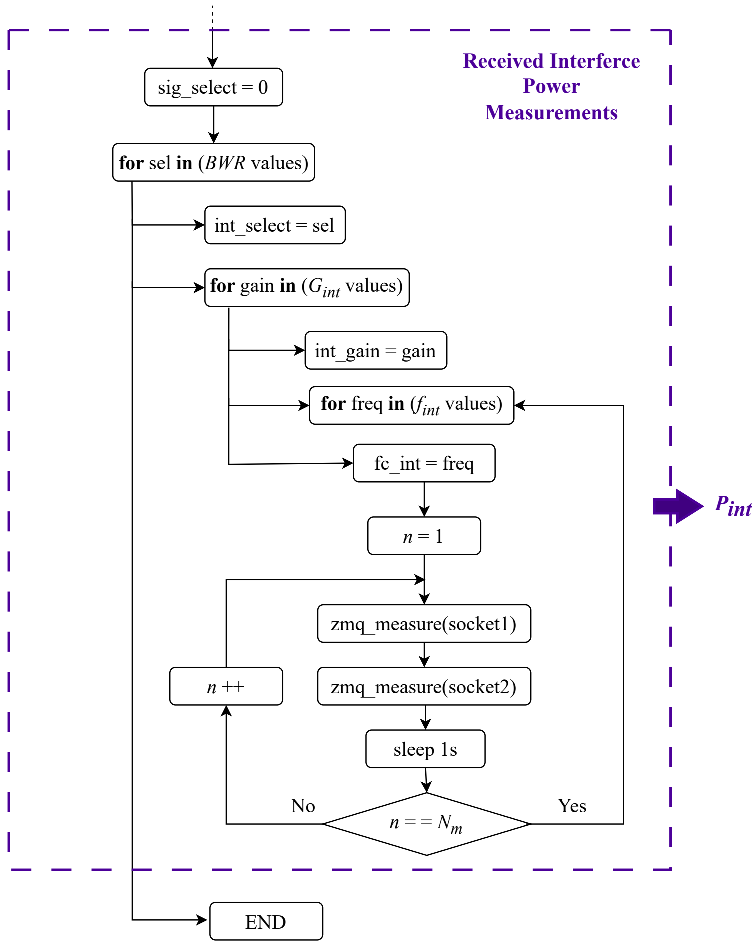

Figure 3.20: Python script flow diagram for the automation of power measurements with the proposed SDR-based testbed. Part 2.

3.3 Measurement Setup

All equipment was placed inside an anechoic far-field chamber designed for a 0.3–18 GHz frequency range. The Tx-Interferer and Rx sides were set 7.2 meters apart, ensuring the far-field region for all antennas under test at the selected center frequency (2.3 GHz). Due to the chamber's configuration, only two of the four available receiving antennas could be measured at a time. The Tx antenna was aligned between them for a fair comparison, as shown in the top-view miniature of Figure 3.21.

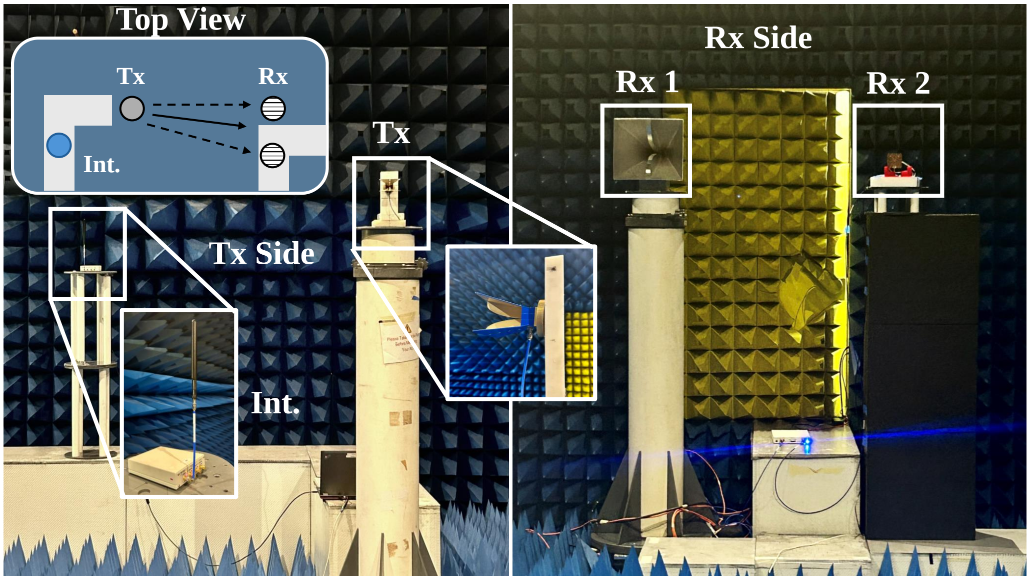

Figure 3.21: Tx-Interfer (left) and Rx (right) side anechoic far-field chamber setup for the proposed SDR-testbed system. The top view (left-top) shows the antenna alignment.

As previously discussed, the Rx 1 antenna remained the “Horn” antenna throughout all measurements and was used as the reference. To ensure consistency in comparing performance, measurements were conducted three times, each time replacing Rx 2 with one of three antennas: the “Vertical” antenna, the “Reconfigurable” antenna, and the “Filtenna.” Since the “Reconfigurable” and “Filtenna” antennas were characterized with a specific setup [33], the same support structure was used for each measurement regardless of the Rx 2 antenna type. This support structure includes a Rohacell block and a custom 3D-printed holder designed to securely position the selected antenna.

Figure 3.22 shows the described support structure in use with the ”Reconfigurable” antenna. The antenna was mounted in vertical polarization, with the SMA connector positioned at the bottom to avoid placing stress on the board. Additionally, the reconfigurable antennas require a USB serial connection for controlling their actuators, as shown in Figure 3.22(b).

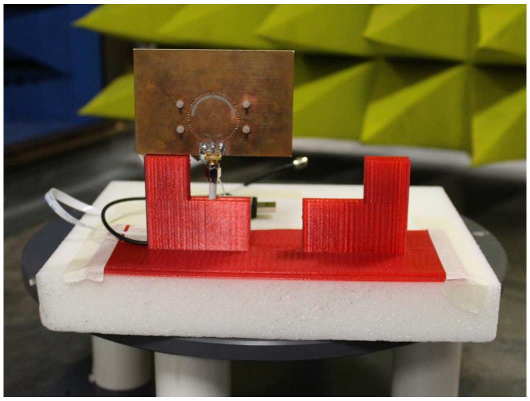

(a)

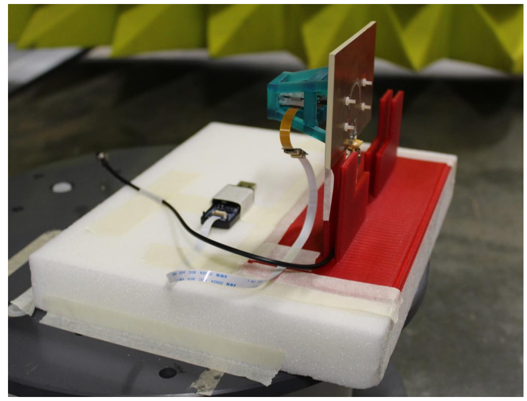

(b)

Figure 3.22: 3D-printed support for Rx 2 antenna, configured as presented in [33]. (a) Front and (b) side view. The example shows the "Reconfigurable" antenna with a small SMA flex cable and the required USB serial connection for the actuators.

3.4 Summary

This chapter introduces the spectrum-congested environment model used to design an SDR-based testbed for comparing antenna system performance. Three main nodes are considered: Tx, Rx, and Interference, with control over the variables listed in Table 3.1. The congested environment is emulated by introducing frequency-variant interference into the main communication network (Tx and Rx nodes). The SDR testbed consists of three computers, two USRP SDR platforms, and four antenna nodes. This study focuses on evaluating different receiving antenna types: "Horn," "Vertical," "Reconfigurable," and "Filtenna," which cover a broad range of characteristics, allowing a more comprehensive analysis of system trade-offs.

The SDR-testbed architecture is divided into two main sections: the Tx-Interferer side and the Rx side. Each side has a dedicated computer running GNU Radio flowgraphs to enable SDR functionality on the USRP hardware. These computers are part of the same network, allowing a third computer to remotely control the flowgraphs through a Python script for automated measurements. The entire system is set in an anechoic chamber to prevent uncontrolled external interference.

Chapter 4

Results

In this section, the performance results for each receiving antenna type in the congested spectrum environment, as defined in Table 3.1, are presented. First, the filtering capabilities of the SDR alone are discussed to assess how much each antenna type improves the overall receiver's (antenna + SDR) filtering. Next, the general received power for each antenna-SDR configuration is presented and analyzed. Following this, a new comparison method is proposed for evaluating out-of-band (OOB) suppression among the antennas. Lastly, these findings are connected with the SINR metrics. This chapter discusses the system-level implications of antenna choice at the aperture level and examines the trade-offs observed in the antennas under test.

4.1 Receiver characterization

The first step in the receiver characterization process was to independently characterize the SDR's filtering capabilities. As previously discussed, the selected receiver SDR, the USRP X310, adjusts the receiver bandwidth using the anti-aliasing filter once a sampling rate is specified. Therefore, for a β_R of 40 MHz, clear rejection around 2.28 GHz and 2.32 GHz is expected.

A USRP B210 was used to transmit a signal with varying gain and bandwidth values. In this setup, the output port of the USRP B210 was directly connected to the input port of the X310 using an SMA cable and two 20-dB attenuators, as shown in Fig. 4.1(a). The power when receiving at the center frequency of 2.3 GHz was calculated and the SDR response over frequency was reconstructed. The SDR-only filtering response does not exhibit a sharp cutoff at the band edges, resembling a window-like response. Instead, a gradual transition is observed.

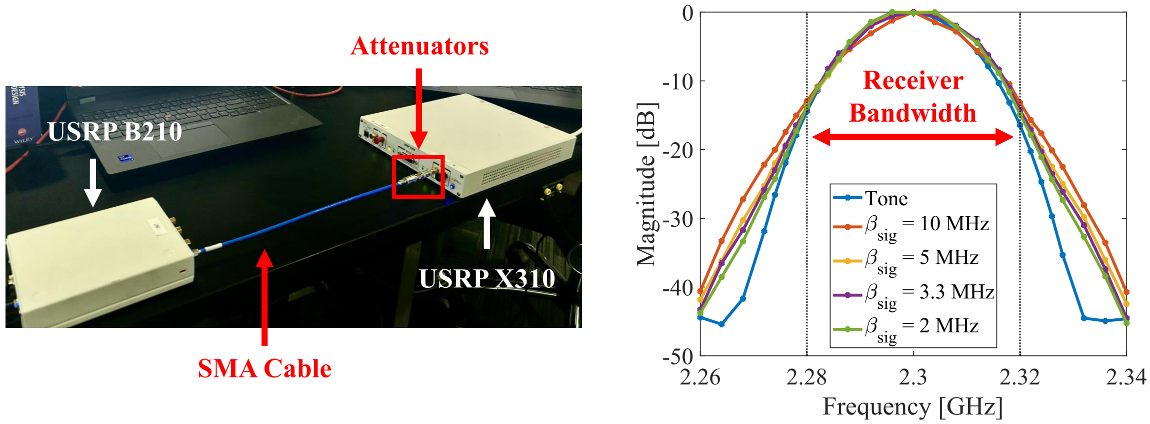

(a) (b)

Figure 4.1: SDR-only filtering characterization (a) measurement setup and (b) normalized frequency response for a 40-MHz receiver bandwidth and a 50-dB gain transmitted signal of varying signal bandwidth. The test setup shows the direct connection between the USRP B210 and USRP X310 with an SMA cable and two 20-dB attenuators.

Fig. 4.1(b) shows that as the transmitted signal bandwidth increases, the filter response broadens over frequency, resulting in reduced rejection at the band edges. The other parameter varied was transmitter gain. Each bandwidth case was tested with four gain values: 30, 40, 50, and 60 dB. Fig. 4.2 shows that the filter shape across frequency remains roughly the same for all gain settings, between 2.27 and 2.33 GHz. Deviations at more distant frequencies are related to the gain level. Lower gain values reach the minimum detectable power earlier than higher-gain signals, thereby exhibiting less dynamic range.

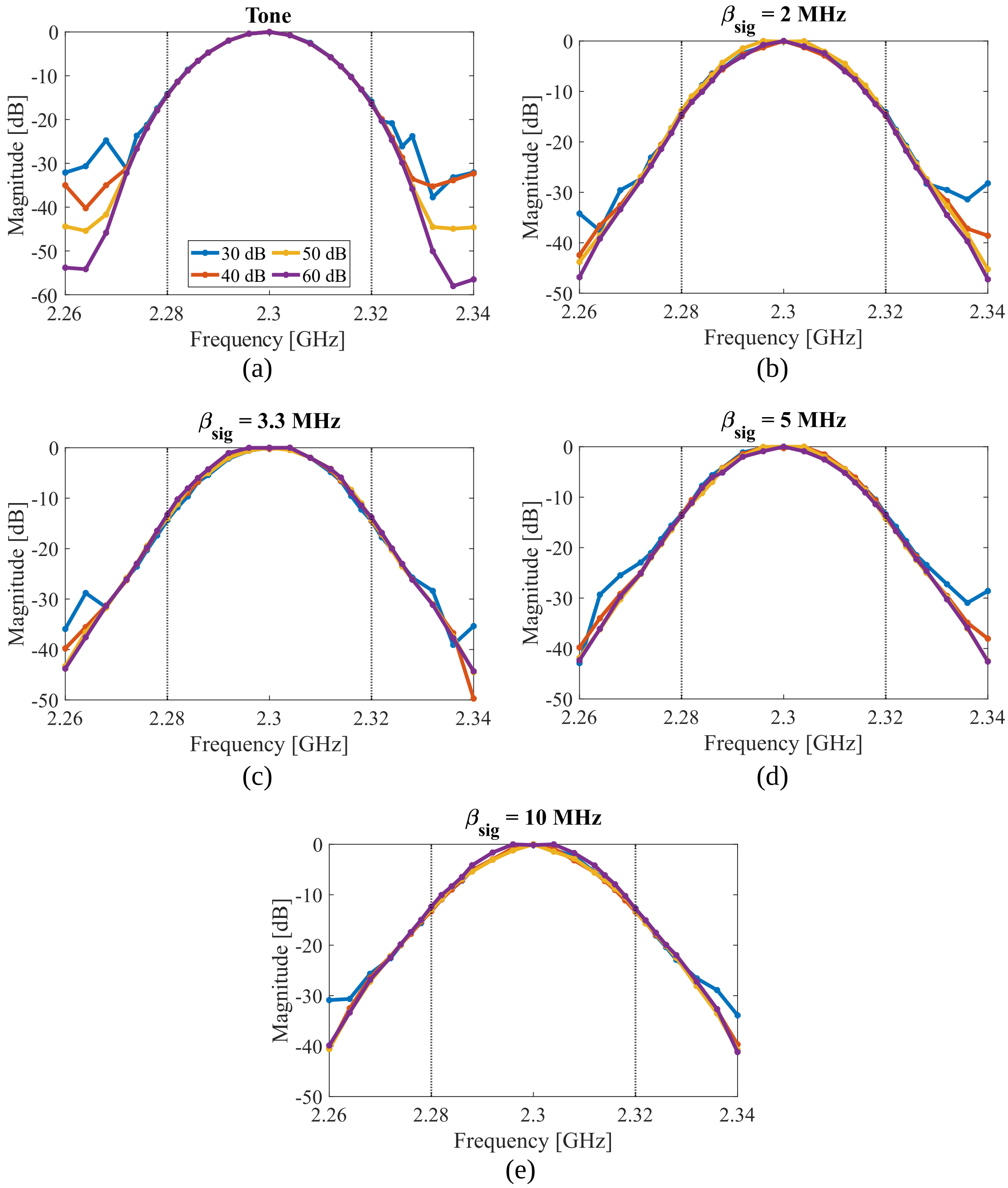

Figure 4.2: SDR-only filtering response for a 40-MHz receiver bandwidth and a gain-variant transmitted signal according to the signal bandwidth: (a) Tone, QPSK-modulated signal with a (b) 2 MHz, (c) 3.3 MHz, (d) 5 MHz and (e) 10 MHz bandwidth.

For example, in Fig. 4.2(a), the normalized response for a 30-dB gain signal shows a 30 dB range variation, whereas for the 60-dB gain case, it is about 55 dB. The disagreement also reduces as the signal bandwidth increases, since the overall received power for a modulated broader signal will be higher. This data was saved for later comparison with each antenna-SDR configuration for each scenario.

The overall receiver filtering capability is defined by the combined response of the SDR-only filter and the realized gain over the frequency characteristic of each receiver antenna type. Both have been characterized individually, as shown in Fig. 4.3(a) and (b), respectively. Therefore, the receiver filtering capabilities can be estimated by multiplying these individual responses in the frequency domain. Fig. 4.3(c) shows the receiver filtering response for the four selected antenna types. The "Horn" antenna has the highest gain and the broadest response, followed by the "Reconfigurable" and "Filtenna" cases, which have the second-highest gain. The "Vertical" antenna, despite being as broadband as the "Horn" in this frequency range, has x-axis intersection points similar to the narrowband antenna cases due to its lower gain.

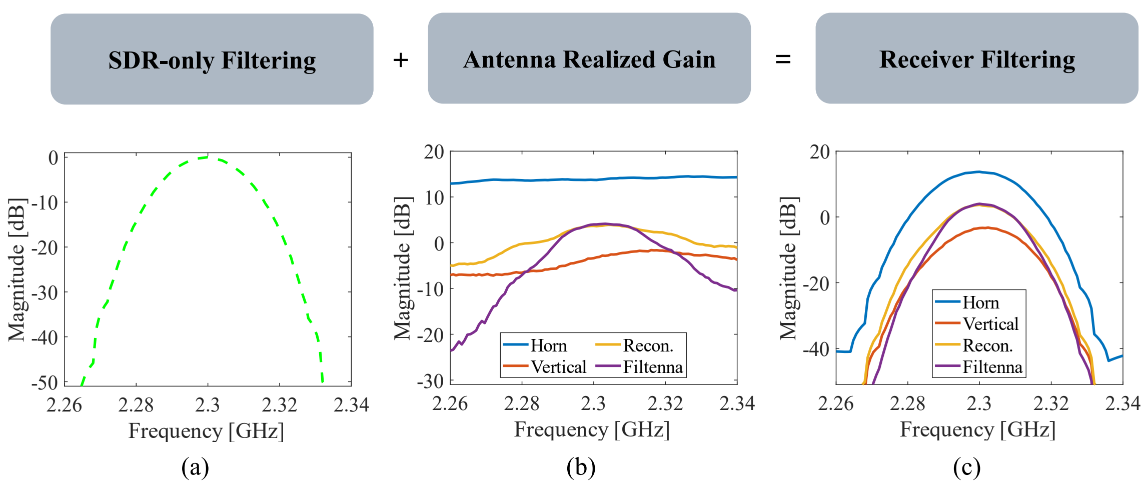

Figure 4.3: Receiver filtering components: (a) SDR-only filtering response, in addition to the (b) realized gain over frequency for each antenna type, results in the (c) final receiver filtering response.

Once each block (SDR and antenna) was characterized and the receiver filtering performance was estimated, the next step involved implementing the proposed SDR-based testbed inside the anechoic chamber and testing the four antenna-SDR configurations. As previously discussed, the Tx and interference nodes used the same antenna types (dual ridge horn and vertical antenna, respectively), while the Rx node allowed for the comparison of two receiver antennas at a time, keeping Rx 1 as the “Horn” as a control. In this initial set of results, only the interference node was transmitting, and the main objective was to compare the received power for each antenna-SDR configuration across the defined test frequency range of 2.26 to 2.34 GHz for a 40-MHz receiver bandwidth. Figure 4.4 shows the received power at 2.3 GHz for both OOB and in-band transmitter carrier frequencies.

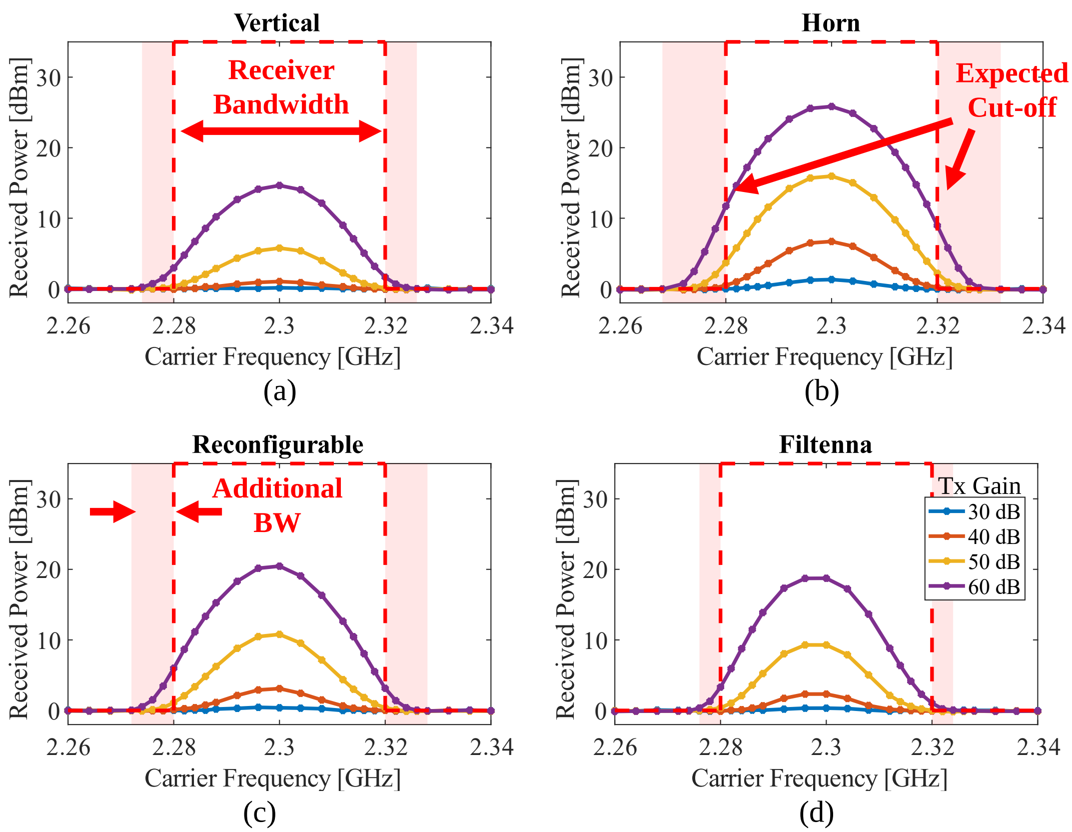

Figure 4.4: Received power in dBm for a gain and frequency-variant transmitter, according to receiver antenna type: (a) “Vertical”, (b) “Horn”, (c) “Reconfigurable”, and (d) “Filtenna”.

As observed in the SDR-only filtering response, Fig. 4.4 shows gradual transitions at the edges rather than a sharp cut-off for specific receiver bandwidths. High-gain OOB interferers across all antenna cases exhibit aliased power at the center frequency at varying levels, thereby increasing each antenna's effective receiver bandwidth differently. The "Vertical" receiver antenna case shows the lowest received power for carrier frequencies both within and outside the receiver bandwidth due to its low-gain characteristic and it is shown in Fig. 4.4(a). In contrast, the "Horn" antenna demonstrates the opposite behavior, with Fig. 4.4(b) showing the highest received power within and outside the band, leading to a larger effective bandwidth than in the other cases. This behavior aligns with the estimations shown in Fig. 4.3(c).

In the narrowband antenna cases, the "Reconfigurable" antenna shows higher received power for in-band carrier frequencies, while receiving lower power for OOB signals. However, its effective bandwidth remains comparable to the "Vertical" case, as illustrated in Fig. 4.4(c). The "Filtenna" case maintains in-band received power similar to the "Reconfigurable" antenna case, but provides better OOB suppression, resulting in a smaller effective bandwidth.

4.2 Out-of-Band (OOB) Interference Rejection

Each receiver antenna exhibits different gains, which can be linked to its ability to efficiently filter interference. Lower-gain antennas are less likely to capture low-gain interference. Therefore, to properly assess their OOB rejection capabilities, the received interference power for each antenna was normalized. The normalization process involved isolating the interference received power P_{int}, over frequency and dividing it by the maximum P_{int} value, which in most cases occurs at f_{int} = 2.3 GHz for each parameter set or scenario.

The normalization allows for a comparison of the OOB suppression of each antenna relative to the maximum received power detected in each case, reducing the gain level differences in the analysis. Fig. 4.5(a) shows the normalized plot for all antenna cases and the SDR-only response for a 60-dB tone interferer.

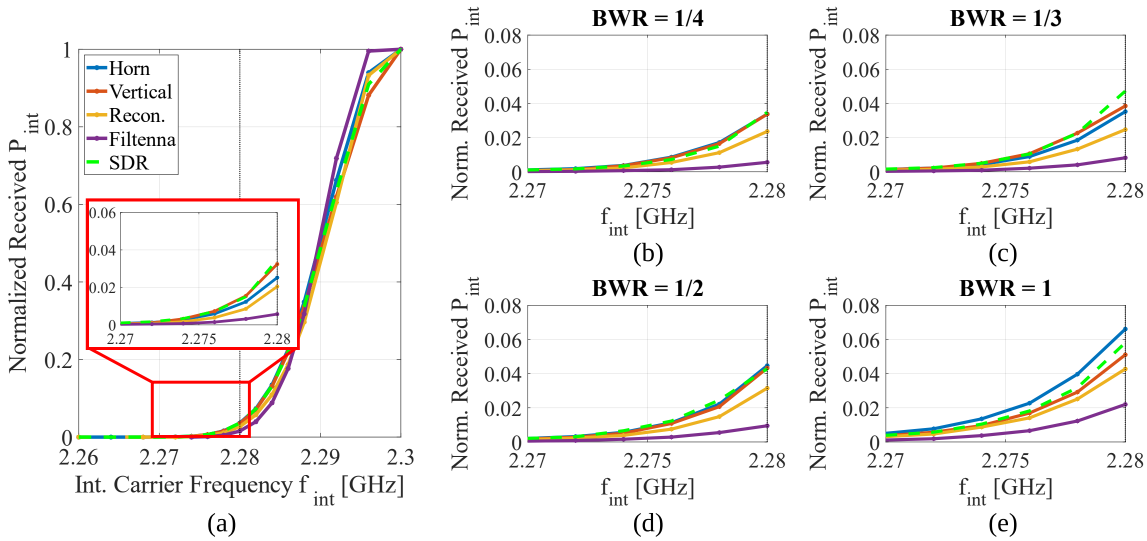

Figure 4.5: Normalized received interference power for each receiver antenna type according to BWR for a 60-dB gain interferer. (a) Normalization done to the 2.3 GHz peak value for each antenna, and zoomed-in values for (b) $BWR = 1/4$, (c) $BWR = 1/3$, (d) $BWR = 1/2$, and (e) $BWR = 1$.

Wireless systems utilize adjacent channels to enhance spectral efficiency, making adjacent channel interference (ACI) a prevalent issue [82].To assess the OOB rejection under ACI conditions, the normalized plots were zoomed in on the range from 2.27 to 2.28 GHz, excluding cases where the interferer is either too far from the intended receiver bandwidth or within the band. Fig. 4.5(b-e) presents the resulting plots.

The broadband “Vertical” and “Horn” antennas closely match the SDR filtering-only response, reducing the received interference power received by the SDR at the edge of the receiver band by 0.87% and 0.58%, respectively. The narrowband “Reconfigurable” antenna reduces 1.70%. Meanwhile, despite having a broader bandwidth than the “Reconfigurable” antenna (approximately +4.6 MHz), the “Filtenna” exhibits the best OOB filtering, reducing by 3.15% of the power received by the SDR. Note that as the BWR increases, the OOB rejection worsens for all receiver antennas, since broader band interference signals result in more transmitted power and higher sidelobe levels in frequency.

Each antenna-SDR configuration exhibits distinct OOB suppression characteristics, and when analyzing only the received power, these differences appear to be related to gain level. However, after removing the gain component, the ratio between the maximum accepted power and the received interferer power at the edge does not exhibit a straightforward relationship with gain. Furthermore, the SDR's filtering capabilities cannot ensure a consistent rejection level, as they vary according to the interferer bandwidth.

Figure 4.6 presents the normalized received interference power in dB, allowing a clearer comparison of the frequency cut-off for each receiving antenna type, with a minimum value of -35 dB.

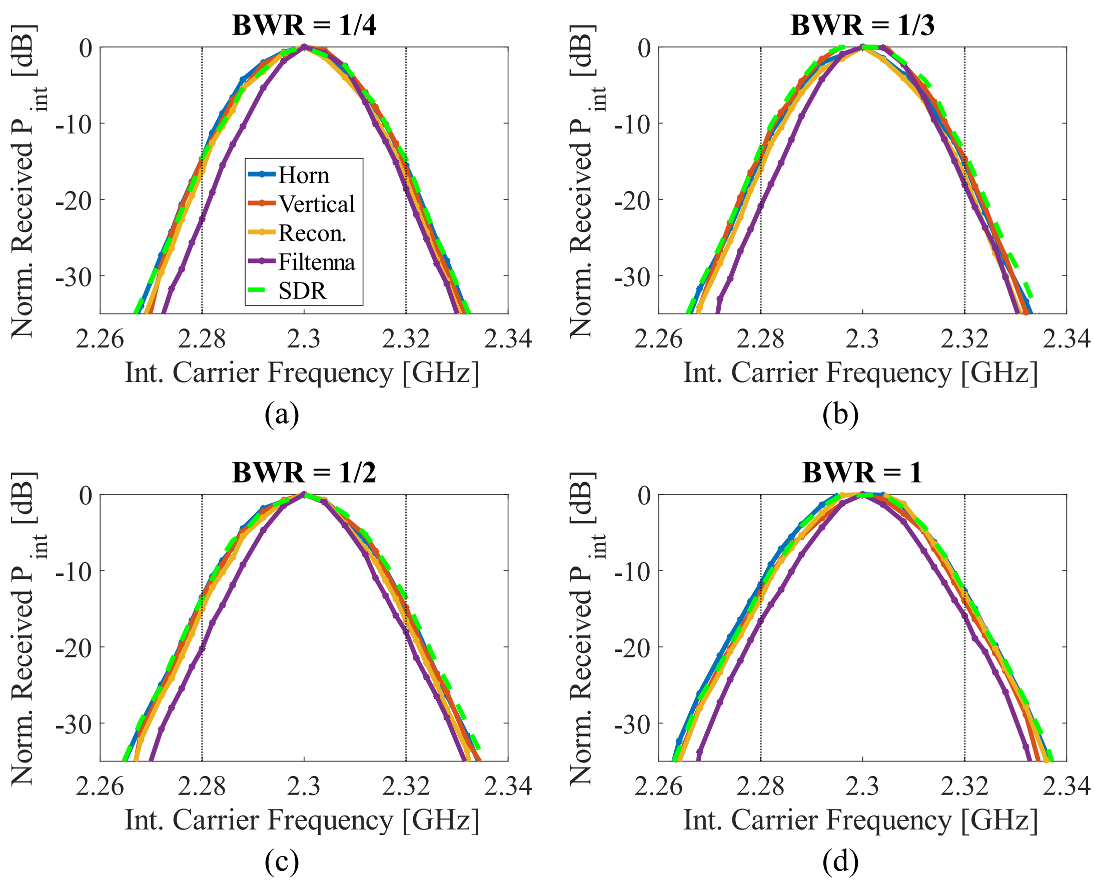

Figure 4.6: Normalized received interference power in dB for each receiver antenna type according to BWR for a 60-dB gain interferer. (a) $BWR = 1/4$, (b) $BWR = 1/3$, (c) $BWR = 1/2$, and (d) $BWR = 1$.

In these plots, the received power values at the edge of the band demonstrate the same OOB rejection properties for each antenna as those shown in Fig. 4.5. Similarly, for broader bandwidth interferers, these values increase. Across all interferer bandwidth cases, the "Filtenna" exhibits the highest OOB rejection, despite its asymmetric frequency response. In addition to the received power values at the band edge, the x-axis indicates an earlier cut-off for the "Filtenna", whereas the "Horn" and "Vertical" antennas align more closely with the SDR frequency response, followed by the "Reconfigurable" antenna.

4.3 Signal-to-Interferer Plus Noise Ratio (SINR) Analysis

Now that the received interference power has been characterized for different interference node and antenna-SDR configurations, the corresponding SINR levels can be calculated using Eq. (2.5). As with the OOB rejection analysis plots, the x-axis in the following plots represents the interferer's carrier frequency. Thus, an SINR value at $f_{int(i)}$ represents the system's SINR level when the receiving center frequency is 2.3 GHz, with an interferer transmitting at $f_{int(i)}$. These plots enable a system-level performance analysis in a congested spectrum environment and assess which antenna-SDR configuration is more robust under these conditions.

Each antenna is expected to exhibit different SINR characteristics across frequency, based on the received power results in Fig. 4.4 and the OOB suppression analysis in Fig. 4.5. This subsection focuses on the OOB SINR levels to assess the advantage that aperture-level filtering, in addition to SDR filtering, can achieve at system-level performance. The key characteristics to observe in these plots are: (i) the frequency at which interferer power begins to alias outside the band, indicating a larger-than-intended receiver bandwidth, and (ii) the extent of SINR degradation at the edge of the receiver band caused by this aliased power. These concepts are illustrated in Fig. 4.7, using a 2.5 MHz QPSK-modulated interferer ($BWR = 1/4$) with varying gain.

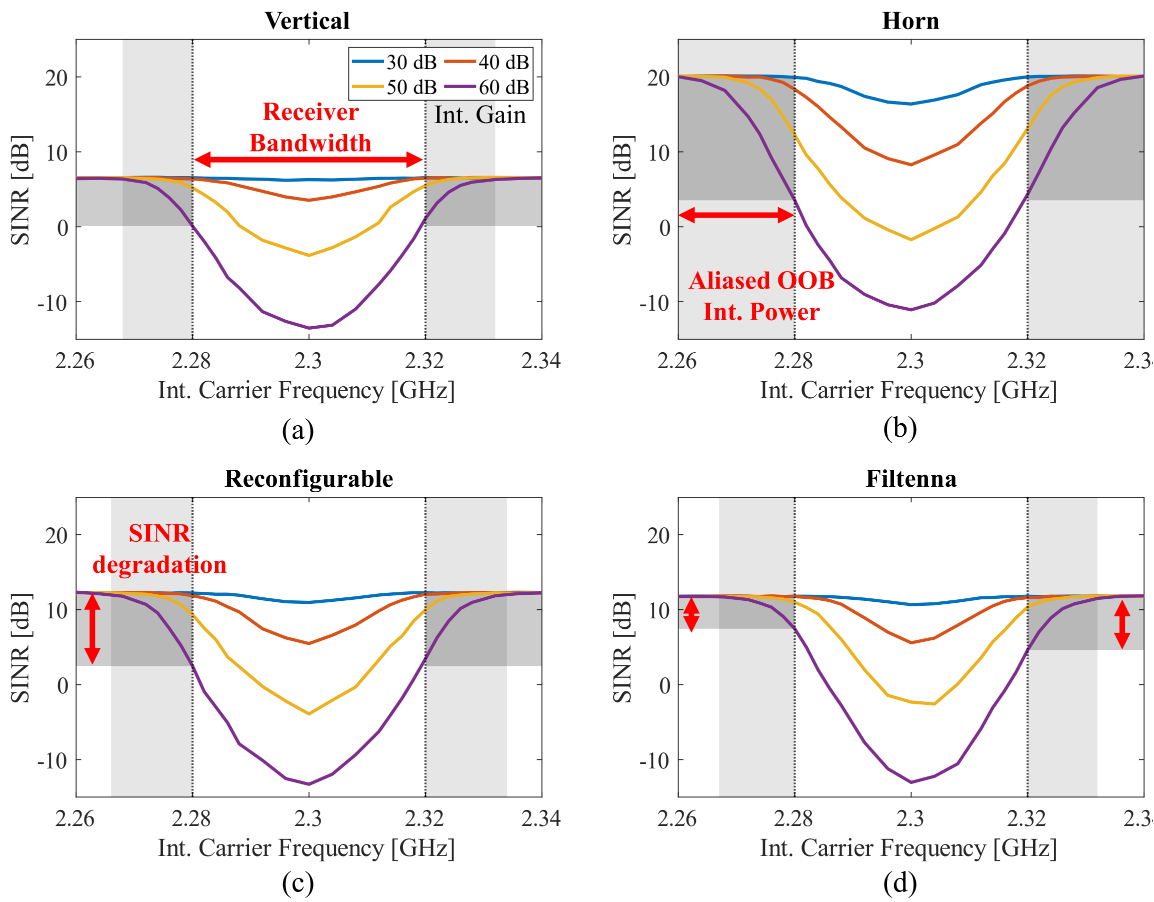

Figure 4.7: SINR levels for a frequency and gain variant QPSK-modulated interferer (BWR = 1/4) according to the antenna-SDR receiver configuration: (a) "Vertical", (b) "Horn", (c) "Reconfigurable", and (c) "Filtenna".

Fig. 4.7(a) shows that the highest SINR level is achieved by the "Horn" with 20.12 dB, followed by the "Reconfigurable" and "Filtenna" cases with 12.34 and 11.76 dB in Fig. 4.7(b) and (d), respectively. Lastly, the "Vertical" antenna reaches a peak SINR level of 6.45 dB as seen in Fig. 4.7(b). These results align with their gain values (see Table 3.2); however, the rate of SINR degradation and how early it occurs vary among the antennas and interference gain. It is important to note that the "Filtenna" has a slight asymmetrical response, therefore the average between both sides was and will be used in the results discussions.

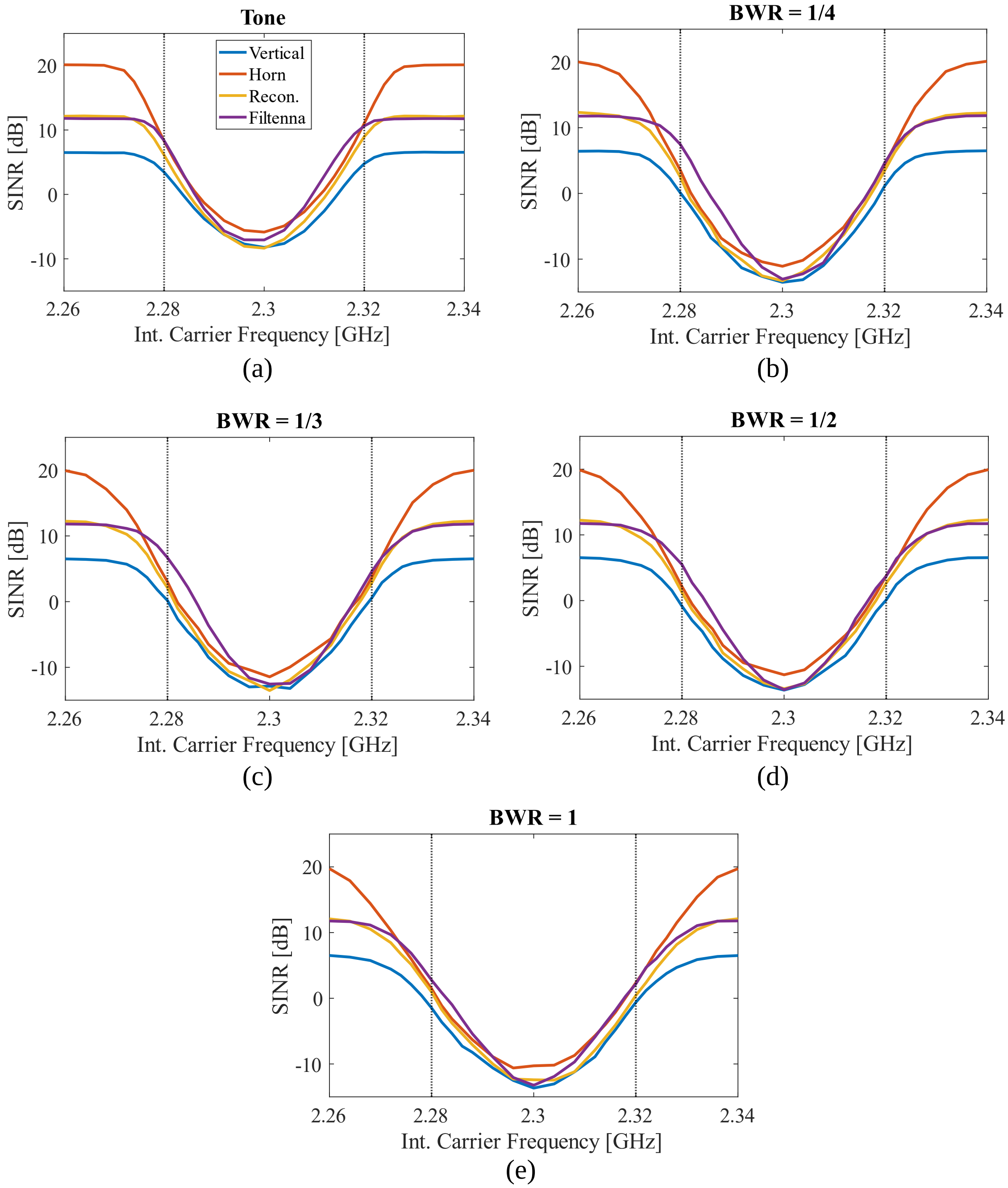

Figure 4.8: SINR levels comparison for a frequency variant QPSK-modulated interferer (G_{int} = 60 dB) according to the interferer-bandwidth-to-signal-bandwidth ratio BWR: (a) Tone, (b) BWR = 1/4, (c) BWR = 1/3, (d) BWR = 1/2, and (e) BWR = 1.

Fig. 4.8 shows the SINR level as a function of the interferer carrier frequency for different interference bandwidths, with a G_{int} of 60 dB. Fig. 4.8(a) shows the SINR values for the narrowest interferer case, a tone interferer, with SINR degradation beginning closer to the band edge. The interferer-bandwidth-to-signal-bandwidth ratio (BWR) then increases from Fig. 4.8(b) to (e). Regardless of antenna type, SINR degradation increases as the interferer bandwidth widens; however, the frequency at which this degradation begins varies by antenna. The rate and extent of this degradation determine the SINR value at the band edge.

ACI power aliased into the main receiver bandwidth causes SINR degradation at the band edges. Fig. 4.9 shows the frequency characteristics for each antenna-SDR configuration, along with the corresponding SINR for a 60 dB tone interferer case. These plots allow for a detailed comparison between receiver antennas and illustrate the impact of SINR degradation.

First, the receiver filtering capabilities (realized antenna gain and SDR-only filter) discussed earlier will be analyzed in more detail. Fig. 4.9(a) and (b) show that for both broadband antenna cases, the drop in OOB gain is primarily determined by the SDR-only filtering characteristics. The average peak-to-band-edge gain ratios (PBR) for the "Vertical" and "Horn" antennas are 44:1 and 27:1, respectively. As a narrowband antenna, the "Reconfigurable" antenna achieves a slightly better ratio of 66:1, as shown in Fig. 4.9(c). However, Fig. 4.9(d) shows that, since the "Filtenna" already exhibits OOB gain suppression, combined with SDR filtering, it reaches a ratio of 248:1.

High PBR ratios correspond to less SINR degradation, while low PBR ratios indicate more SINR degradation. Therefore, a high-gain broadband antenna like the "Horn" achieves a higher peak SINR. However, due to its low PBR ratio, the SINR value at the receiver band edge is comparable to that of the "Filtenna," as shown in Fig. 4.9(b) and (d).

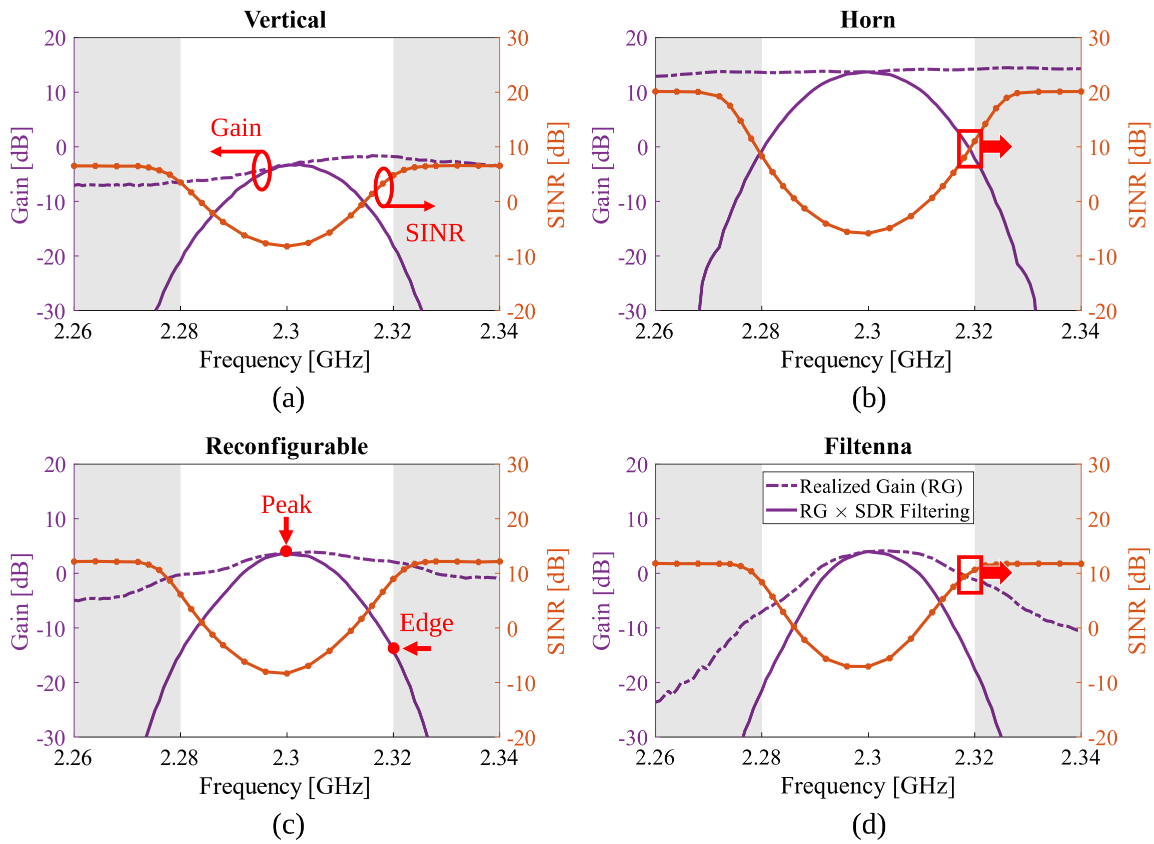

Figure 4.9: Measured realized antenna gain compared to the effective receiver gain (left axis) and its respective signal-to-interferer-plus-noise ratio (SINR) in dB (right axis) for each antenna under test: (a) "Vertical", (b) "Horn", (c) "Reconfigurable", and (d) "Filtenna". The SINR for each antenna was calculated using a single-tone interferer with 60 dB gain.

It has been established that SINR degradation depends on interference gain, bandwidth, and antenna-SDR characteristics, such as the PBR. One additional variation that the proposed SDR-based testbed allows for is the consideration of the antenna characteristics of the Tx and interference nodes, as well as their relative positions to the receiver antennas.

In the original setup, the Tx node has a moderately directive horn antenna aligned with the Rx antennas, while the interferer node uses a vertical omnidirectional antenna positioned to the right of the Tx node. Switching these nodes at the software level, i.e. without moving the antenna position, results in a directive interferer antenna and an omnidirectional Tx antenna. Fig. 4.10 shows the SINR values at the band edge for both scenarios, considering a gain and bandwidth-variant interferer.

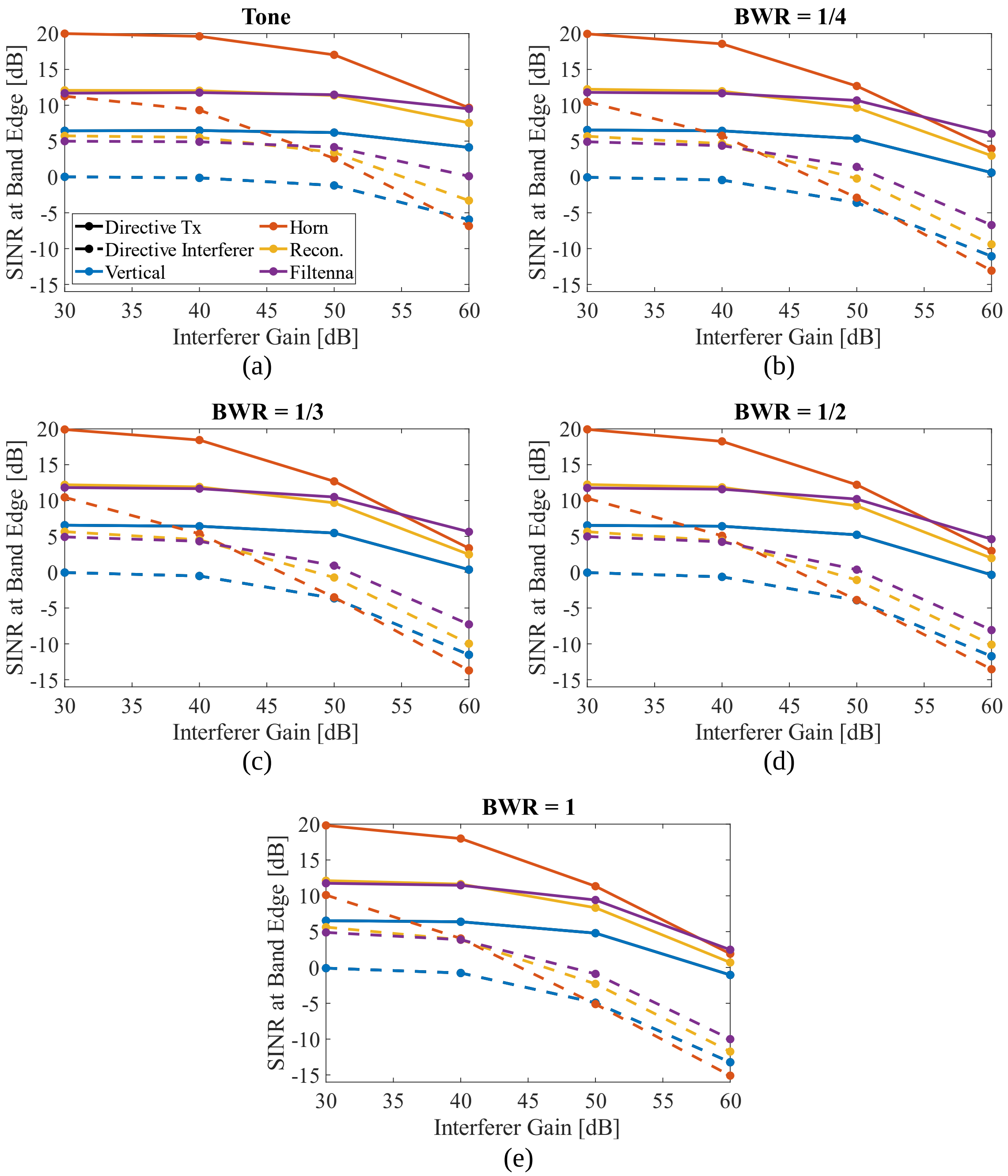

Figure 4.10: SINR level at the receiver band edge for each receiver antenna according to interferer gain and the interferer-bandwidth-to-signal-bandwidth ratio BWR: (a) Tone, (b) BWR = 1/4, (c) BWR = 1/3, (d) BWR = 1/2, and (e) BWR = 1. For both Tx-Interferer antenna variations: (–) directive Tx and (- -) directive interferer.

The SINR level when the interferer gain G_{int} is 30 dB is approximately the same as the peak SINR value identified for each receiver antenna case, regardless of BWR for the directive Tx case. Therefore, low-gain interferers with narrow bandwidths do not significantly affect system performance from the SINR perspective. As the gain of the interferer increases, so does the SINR degradation. The maximum SINR degradation case occurs when the interference gain and bandwidth are the highest (G_{int} = 60 dB and BWR = 1), as shown in Fig. 4.10(e).

Comparing the peak SINR levels to the maximum SINR degradation case, the "Horn" presents the most degradation at -18.09 dB, followed by the "Reconfigurable" antenna with -11.42 dB, and the "Filtenna" with -9.22 dB. Lastly, the Vertical" presents -7.57 dB of degradation. Note that even though the "Vertical" antenna presents less degradation, it still has the lowest overall SINR level due to its low gain and broadband characteristics.

The "Filtenna" and "Reconfigurable" antennas exhibit similar characteristics across different interferer gains. However, as the bandwidth of the interferer increases, the two begin to diverge, highlighting the superior filtering capabilities of the "Filtenna". This distinction is also important when comparing the "Horn" and "Filtenna," as the "Horn" is more susceptible to high-gain interferers. For QPSK-modulated interferer cases, the "Filtenna" shows the lowest SINR degradation for a 60 dB interferer gain.

In the second case (directive interferer), the "Filtenna" demonstrates greater resilience in SINR degradation even for lower interferer gains. In contrast, the "Horn" loses its directivity advantage and experiences more rapid SINR degradation. Additionally, the peak SINR level for this case is approximately 9.32 dB lower than that of the directive Tx case for the "Horn," while the other receiver antenna types exhibit a drop of less than 7 dB.

4.4 Reconfigurability Capability Analysis

SDR-based systems are often preferred for their flexibility, and reconfigurable narrowband antennas are designed to support this flexibility without compromising channel selectivity, unlike broadband antenna solutions. In this subsection, the center frequency f_{sig} is adjusted to evaluate the potential SINR improvement when interference is detected at a specific frequency and the SDR cognitive engine selects an optimal center frequency. Fig. 4.11 presents the reconfigurability test results for all receiver antenna types. The new center frequency was set to 2.32 GHz, while the test frequency span was maintained from 2.26 to 2.34 GHz.

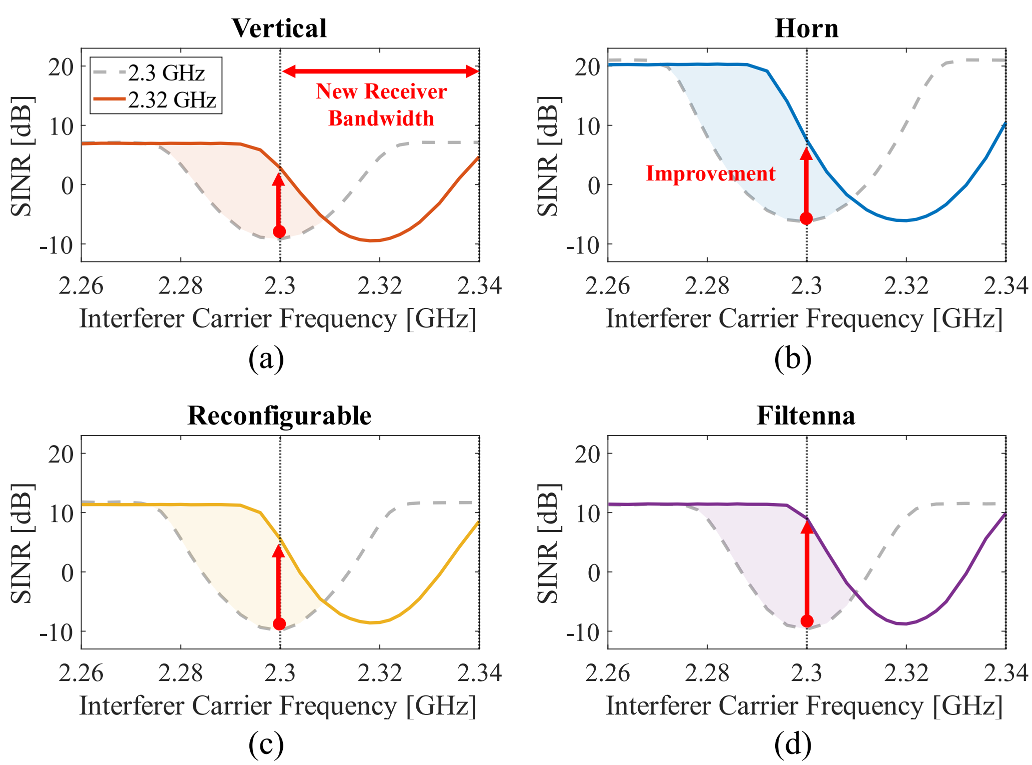

Figure 4.11: SINR comparison for a 60-dB tone interferer when reconfiguring the system's center carrier frequency to 2.32 GHz according to receiver antenna type: (a) "Vertical", (b) "Horn", (c) "Reconfigurable", and (d) "Filtenna". Original 2.3 GHz center frequency case (- -) and new 2.32 GHz center frequency (–).

Similar to previous tests, these plots display the SINR level considering a 60-dB gain tone interferer sweeping across the test frequency span, but for a 40-MHz receiver bandwidth around 2.32 GHz instead of 2.3 GHz (20 MHz shift). Both the "Vertical" and "Horn" antennas cover the new center frequency; however, the "Reconfigurable" and "Filtenna" antennas had to be tuned to that frequency. Considering the worst SINR case for each antenna, i.e., an interference carrier frequency at 2.3 GHz, the SINR level improves by 12.24 dB for the "Vertical" antenna, 14.2 dB for the "Horn" antenna, 15.93 dB for the "Reconfigurable" antenna, and 18.74 dB for the "Filtenna." Despite an initially lower peak SINR level, the "Filtenna" outperforms the "Horn" due to its higher selectivity around the band.

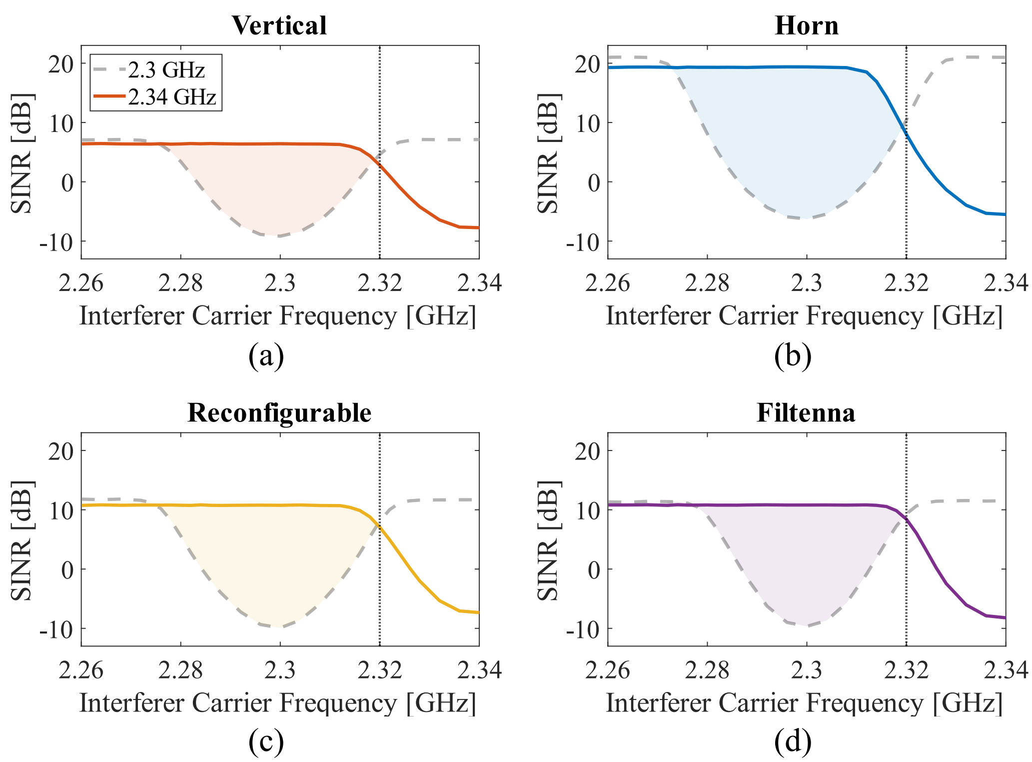

Figure 4.12: SINR comparison for a 60-dB tone interferer when reconfiguring the system's center carrier frequency to 2.34 GHz according to receiver antenna type: (a) "Vertical", (b) "Horn", (c) "Reconfigurable", and (d) "Filtenna". Original 2.3 GHz center frequency case (- -) and new 2.34 GHz center frequency (–).

Fig. 4.12 shows the results if the center frequency is changed to 2.24 GHz (40 MHz) instead. The SINR improvement, considering a 2.3 GHz interferer carrier frequency, is 15.59 dB for the "Vertical" antenna, 25.67 dB for the "Horn", 20.64 dB for the "Reconfigurable" antenna, and 20.44 dB for the "Filtenna". Now, most of the interferer carrier frequencies are outside of the band and the specific 2.3 GHz case is far away enough to not fall under the SDR filtering or the "Filtenna" aperture-filtering capabilities. Therefore, the SINR level will mostly correlate to the antenna peak gain. Still, the "Filtenna" case shows less degradation at the band edges which will still provide better OOB interference suppression for tight channel selection applications.

4.5 Packet Error Rate (PER) Initial Measurements

In this section, a 10-MHz OFDM signal was transmitted from the Tx node at a 2.3 GHz center frequency. Similar to previous cases, a frequency-variant interferer was introduced with a variable bandwidth (tone, 2.5 MHz, and 10 MHz). For these initial measurements, a single interference gain of $G_{int} = 50$ dB was considered. The objective of these measurements is to evaluate how OOB interference affects the overall PER percentage at the center frequency due to aliased power, considering a receiver bandwidth β_{Rx} of 20 MHz.

Fig. 4.13 presents the results for the described scenario using a "Horn" as the receiver antenna. Fig. 4.13(a) illustrates the PER percentage as a function of the interferer carrier frequency. For interferer carrier frequencies further from the center frequency, the average PER is 27.36%. However, as the interference carrier frequency approaches the receiver bandwidth range (2.29 to 2.31 GHz), the PER increases. Interference with larger bandwidths results in higher PER percentages. Alternatively, Fig. 4.13(b) maps the PER percentages to the received interference power, demonstrating that the SDR-based testbed is capable of performing further PER and SINR analyses using both functions.

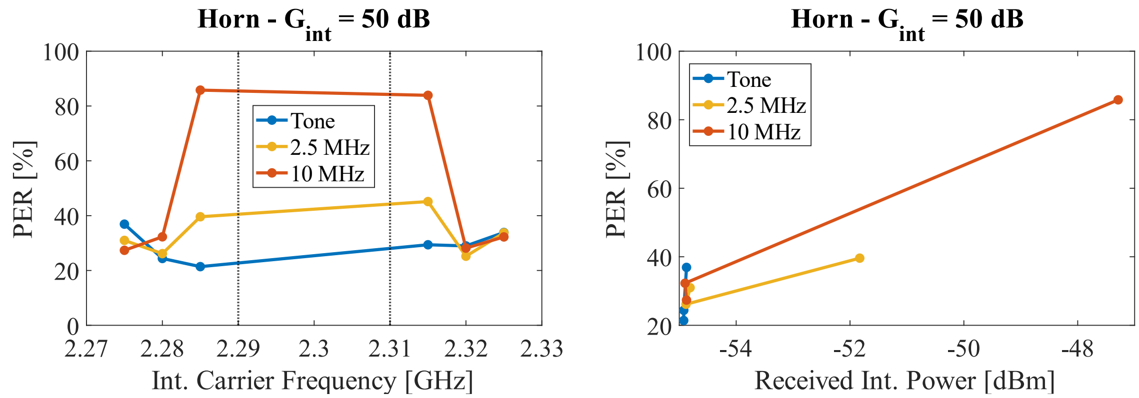

(a) (b)

Figure 4.13: Packet error rate (PER) percentage for an OFDM transmitted signal and a frequency-variant QPSK-modulated 50-dB interferer for a receiving "Horn" antenna. Subplots show PER percentage according to (a) interferer carrier frequency and (b) received interference power in dBm.

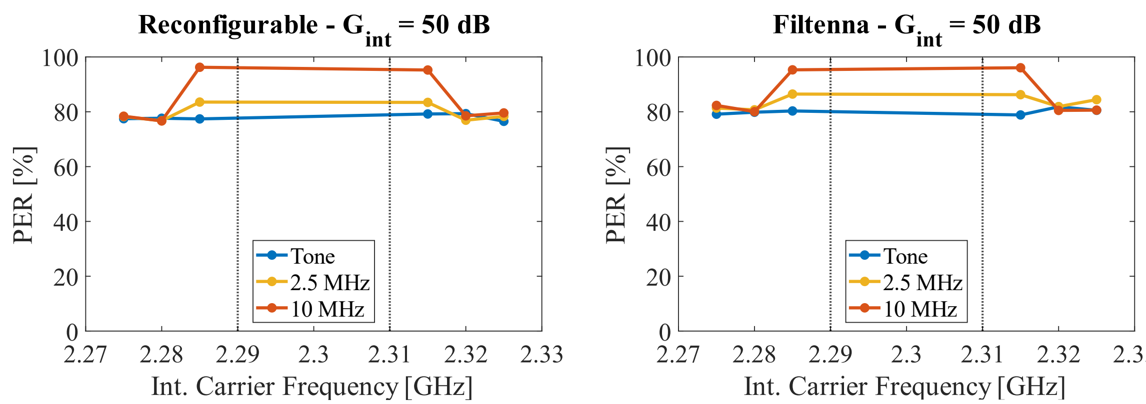

(a) (b)

Figure 4.14: Packet error rate (PER) percentage for an OFDM transmitted signal and a frequency-variant QPSK-modulated 50-dB interferer for (a) the "Reconfigurable" antenna and (b) "Filtenna" as receiver antennas.

Further measurements were conducted with the remaining antenna types. The "Reconfigurable" and "Filtenna" cases exhibit a higher initial PER percentage, approximately 80% for both, as shown in Fig. 4.14. Given that the setup is in a far-field anechoic chamber, these values are significantly higher than expected, indicating room for improvement in these measurements. Similarly, the "Vertical" antenna achieved a 100% PER for all interference cases. Despite this, both subplots in Fig. 4.14 demonstrate the same PER trend: higher PER percentages occur as the interference approaches the receiver bandwidth. This confirms that OOB interference also affects center frequency connection performance.

4.6 Conclusions

This chapter presents an analysis of SDR-integrated antenna types in a congested spectrum environment, focusing on filtering capabilities, received power, and SINR performance. Initial SDR-only characterization revealed gradual frequency transitions without sharp band-edge cutoffs, allowing OOB interference to couple into the center frequency. Each antenna-SDR configuration was then evaluated for received power, demonstrating how antenna characteristics affect receiver response. For OOB rejection, normalized interference power results showed that the "Filtenna" achieved superior suppression due to its selectivity, reducing by 3.15% the power received by the SDR alone at the band edge.

The SINR analysis showed performance differences, with the "Horn" achieving the highest peak SINR (20.12 dB) but experiencing more edge degradation than the other antennas. The "Reconfigurable" and "Filtenna" followed with 12.34 and 11.76 dB, while the "Vertical" antenna reached 6.45 dB. Reconfigurability testing demonstrated the advantages of narrowband antennas in SDR systems, particularly for SINR optimization under interference, with SINR improvements up to 18.74 dB in the "Filtenna." These findings highlight trade-offs in gain, selectivity, and reconfigurability, each affecting receiver bandwidth and interference resilience.

Initial PER results show that OOB interference significantly impacts PER, with higher percentages as interference approaches the receiver bandwidth. While trends are evident, the unexpectedly high values indicate room for improvement. Nonetheless, the system demonstrates basic capabilities for analyzing interference effects and implementing further measurements.

Chapter 5

Conclusions and Future Work

5.1 Summary of Work

The objective of this thesis is to investigate how antenna selection impacts system performance in spectrum-congested scenarios, with a focus on trade-offs related to aperture-level frequency filtering and reconfigurability. The literature review on antenna-SDR performance analysis highlighted a need for rigorous evaluation under controlled, congested conditions to accurately assess reconfigurable antennas' capabilities in CR systems.

A congested spectrum environment was defined to emulate real-world conditions, using three main nodes: transmitter (Tx), receiver (Rx), and interference, each with controlled parameters. This environment was implemented using an SDR-based testbed comprising three computers, two USRP SDR platforms, and four antenna nodes to allow for diverse antenna comparisons.

The testbed is organized into Tx-Interferer and Rx sections, with all three computers connected to the same network. GNU Radio flowgraphs were developed for SDR functionality on the USRP platforms at both the Tx-Interferer and Rx sides, and implemented on their respective computers. A third computer controls the setup remotely, automating measurements with a custom Python script. Three primary measurements are taken for each configuration: (i) received noise power, (ii) received signal power, and (iii) received interference power at the center frequency. The entire system was placed inside an anechoic chamber to isolate it from external interference, ensuring accurate, reliable results and controlled observation of antenna performance.

Test parameters were set around a 2.3 GHz center frequency, and four key antenna types were evaluated using the SDR-based testbed: “Horn,” “Vertical,” “Reconfigurable,” and “Filtenna.” These antennas were chosen for their diverse characteristics (gain, bandwidth, size) and tested under various interference conditions, with measurements repeated to ensure accuracy. The collected data enabled the calculation of SINR and comparative analysis across antenna types.

Results indicate that antenna-SDR configurations display distinct behaviors in filtering and SINR performance. SDR-only tests showed gradual transitions without sharp band-edge cutoffs, allowing out-of-band interference to affect the center frequency. The “Filtenna” provided the highest out-of-band rejection, reducing by 3.15% the interference power received by the SDR-only. SINR analysis revealed that the “Horn” antenna achieved the highest peak SINR (20.12 dB) but experienced greater degradation near band edges, while the “Reconfigurable” and “Filtenna” followed with SINR levels of 12.34 dB and 11.76 dB, respectively.

Under ACI conditions, high-gain broadband antennas and narrowband filtering antennas present comparable SINR performance but very different SWaP characteristics. However, aperture-level tunable filtering shows higher SINR performance for spectral-efficient adjacent channels. These findings highlight the trade-offs between gain, selectivity, and reconfigurability, demonstrating how antenna choice influences bandwidth and interference resilience in SDR-based systems.

5.2 Contributions

The work presented in this thesis has contributed to the reconfigurable antenna, filtering antenna, and cognitive radio state-of-the-art as follows:

- Development of an SDR-based testbed to emulate a controlled, spectrum-congested environment, enabling the automated comparison of multiple antenna types.
- Characterization of reconfigurable and frequency-filtering antennas with an SDR platform as a receiver unit, assessing their out-of-band rejection and SINR performance based on aperture-level filtering.
- Proposition of key parameters and metrics to facilitate comprehensive antenna performance comparisons under spectrum-congested environments.
- Identification of SDR-based system trade-offs at the system level, impacted by antenna gain, selectivity, and reconfigurability at the aperture level.
- Initial work was conducted on PER and received interference power joint analysis using the proposed SDR-based testbed.

5.3 Future Work

Spatial Filtering Analysis in Spectrum Congested Environments

Based on the characteristics of the current antenna under test, the ”Horn” has the most directive pattern, enabling additional filtering in the spatial domain.

The current results focus on the frequency-filtering capabilities of the receiver, with the interference node position remaining constant across all measurements. However, changing the interference node position could place the interferer within the “Horn” main beam, near the main beam, or entirely outside of it. This analysis would enable a comparison in interference rejection between a spatial-filtering broadband antenna and an omnidirectional-pattern frequency-filtering antenna.

In future work, the exploration of pattern and polarization reconfigurability will be crucial. By implementing reconfigurable antennas that can adapt their radiation patterns and polarization states, it may be possible to further optimize interference rejection. For instance, adjusting the polarization of the receiving antenna could enhance the system's ability to mitigate co-polarized interference while maintaining signal integrity. Additionally, reconfigurable patterns could allow for dynamic adjustment to interference conditions, maximizing performance in real time. Such advancements would provide valuable insights into the interplay between spatial and frequency filtering techniques in complex wireless environments.

Final PER Measurements

As highlighted in Chapter 4, the PER percentages obtained were significantly higher than the expected values for measurements conducted inside the anechoic chamber, particularly given the calculated SINR measurements. Therefore, modifications to the PER measurement process and the signal characteristics used are necessary.

During the measurement process, some underflow and overflow errors were observed in the Tx and Rx computer terminals, which might be causing issues in how the data is generated and received at the software level. Optimizing the data generation process, particularly on the Tx-Interferer computer side, which handles output data for two USRPs, could help reduce these errors.

There are several OFDM parameters that can be modified to achieve a more robust signal across measurements, such as FFT, occupied carriers, etc. Additionally, other equipment is available that can be used as a reference for a specific OFDM signal configuration and later compared to the results obtained with this system. This will help rule out changes in the antennas or other far-field chamber setups as the source of the issue.

Appendix A

X-band Reflector Antenna for Sea Clutter Rejection

A.1 Introduction

Radar systems detect and track small targets over large distances and at low elevation angles, often close to the horizon. Achieving such precision necessitates high radiated power and increased receiver sensitivity [83]. However, these operational requirements introduce significant challenges, particularly in the form of unwanted signal reflections from the surrounding environment, often called clutter. These undesired signals usually enter through sidelobes for tracking antennas, further complicating target acquisition.

Sea clutter poses an especially challenging problem in radar applications. Its average reflectivity, defined as the radar cross-section per unit surface area illuminated by the radar, depends on various parameters such as sea state, grazing angle, polarization, and radar frequency [84]. The critical analysis by Nathanson [85] highlights the complexity of sea clutter, providing engineers with vital data on reflectivity under diverse conditions. This data forms the foundation for radar specification and performance assessments. Effective sea clutter models are, therefore, essential for radar system design and development [86].

Reflector antennas are a prevalent choice in radar applications due to their ability to deliver high gain, wide bandwidth, and excellent angular resolution with cost efficiency [87]. These antennas, which include configurations such as paraboloids, are engineered to focus or radiate electromagnetic energy efficiently over their aperture. Their capability to achieve precise beam shaping and energy confinement makes them particularly suitable for mitigating some of the challenges posed by clutter in radar systems.

In this work, an X-band reflector antenna for overseas deployment was designed and optimized to mitigate sea clutter. The radar system is intended to identify birds from a buoy, needing careful consideration of size constraints, beamwidth, and scanning requirements. This material is based on work supported in part by the U.S. Geological Survey under Grant/Cooperative Agreement No. G23AC00569-00. The following sections detail the design and optimization of a paraboloid reflector antenna, exploring various sizes, focal points and feed configurations. Subsequently, the resulting radiation patterns were used as inputs for a MATLAB sea clutter simulation to analyze the initial returned power. Different scanning angles were simulated, and their results were evaluated. Finally, the findings and trade-offs identified are summarized in the conclusions section.

A.2 Radiation Pattern Optimization

Parabolic reflectors operate on the principle that when a point source is positioned at the focal point of a parabola, the rays reflected by the parabolic surface emerge as a parallel beam. That is, a parabolic reflector transforms a spherical wave radiated by the feed located at its focus into a plane wave [1, 2]. Since the transmitter or receiver is located at the parabola's focal point, this configuration is commonly referred to as front-fed.

Fig. A.1 shows the side view of a parabolic reflector antenna model built in HFFS. This figure illustrates a source feed radiating energy toward the reflector, with the field being reflected back into space. The reflector curvature can be modeled as

$$x^2 = 4f_p(f_p + z) \tag{A.1}$$

where f_p is the focal point, and x and z represent coordinate points in the x-z plane.

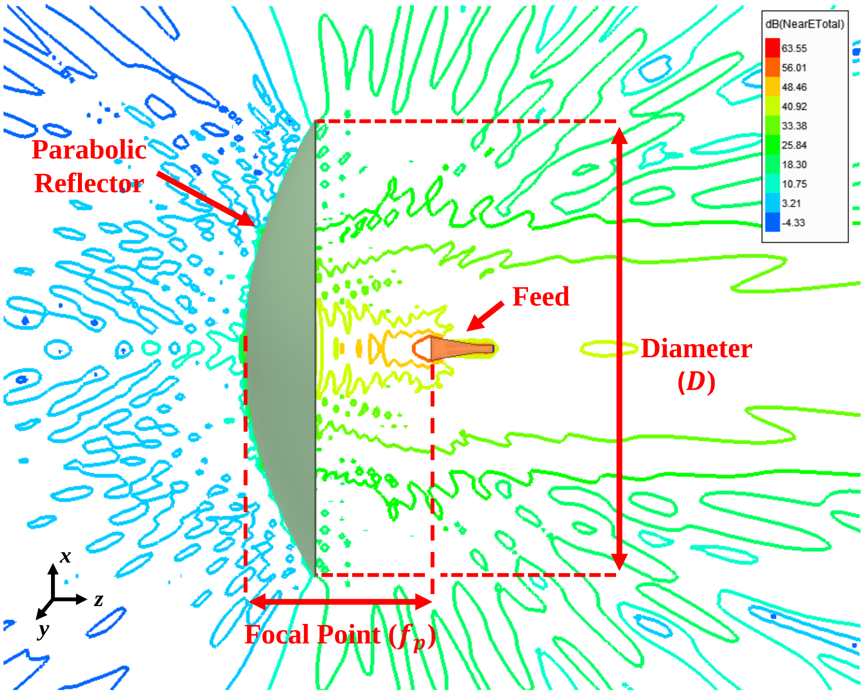

Figure A.1: Parabolic reflector antenna near-field electric field behavior and antenna components for optimization.

For radiation pattern optimization, three main characteristics of the reflector antenna will be analyzed: (i) the feed antenna illuminating the reflector, (ii) the focal point f_p, and (iii) the diameter (D) of the parabolic reflector. Each configuration aims to achieve the lowest sea clutter return power within the size constraints of the buoy. The center frequency of the radar system is 9.41 GHz, and horizontal polarization is desired.

A.2.1 Size Analysis

Reflector antennas tend to exploit the reflector's aperture to obtain narrower beam widths. However, in this work, one of the main concerns is the size and weight of the antenna, as it will be deployed on a buoy with limited space. Consequently, an analysis of the reflector's diameters, i.e. size, was performed while maintaining the same feed and focal point. Fig. A.2 shows the 3D model built in HFSS, using a pyramidal horn antenna based on a WR-90 waveguide as the feed, with a focal point f_p of 32.5 cm. The reflector's diameter was varied from 0.6 m to 1.2 m in 0.2 m increments.

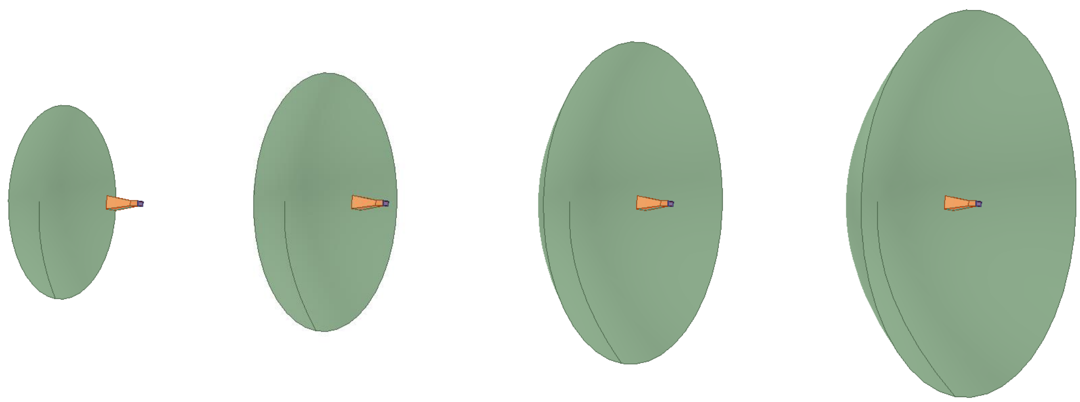

D = 0.6 m D = 0.8 m D = 1.0 m D = 1.2 m

Figure A.2: Parabolic reflector 3D HFSS model for varying diameters. The reflector's diameter D was varied from 0.6 to 1.2 m.

Then, the E-plane corresponding to the vertical polarization was plotted for each case and compared in Fig. A.3. The 1.2 m-diameter case shows the narrowest 3-dB beamwidth at 2.92 degrees, followed by the 1 m-diameter case at 3.06 degrees, and the 0.8 m- and 0.6 m-diameter cases at 3.34 and 3.84 degrees, respectively. Additionally, the gain decreases as the reflector size decreases, going from a maximum of 33.58 dB for the 1.2 m-diameter case to 32.90 dB for the smallest reflector case.

Another important aspect of the analysis is the backplane radiation, since the reflector antenna is surrounded by other structures in the buoy that can contribute to undesired power returns. Fig. A.3 shows that the 0.6 m-diameter case presents high backplane radiation. The front-to-back ratio for each dimension is 41.4 dB, 46.90 dB, 49.0 dB, and 50.27 dB for the smallest to largest case, respectively. Therefore, in this work, the 0.8 m-diameter reflector is considered the most compact option with the least performance degradation.

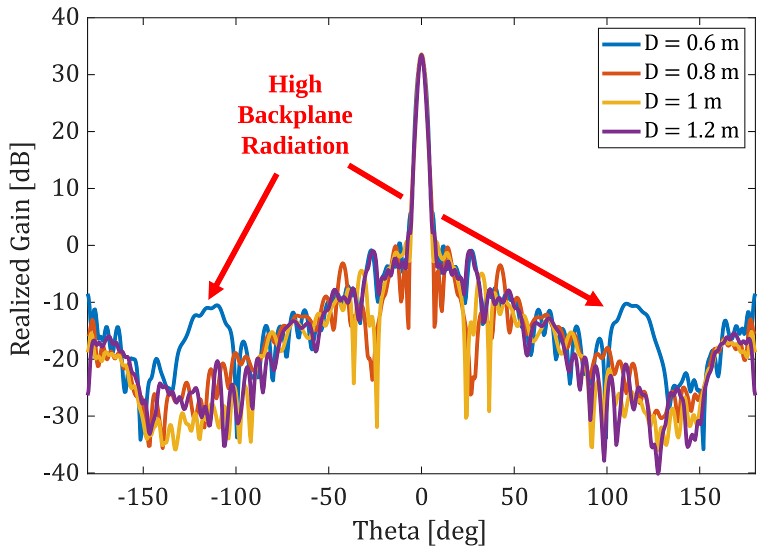

Figure A.3: E-plane cut for a parabolic reflector of diameter D fed by a pyramidal horn antenna at a 32.5-cm focal point. The reflector's diameter D was varied from 0.6 to 1.2 m.

A.2.2 Feed Comparison

Next, the feed type was varied for the selected 0.8-meter diameter reflector while maintaining a 32.5 cm focal point. Fig. A.4 shows the four main feeds that were tested: (i) open-ended WR-90 waveguide, (ii) pyramidal horn antenna, (iii) E-sectoral horn antenna, and (iv) rear-fed waveguide, also referred to as the clutter feed.

All feeds are excited through a WR-90 waveguide. The open-ended waveguide shown in Fig. A.4(a) simply radiates energy toward the reflector. On the other hand, Fig. A.4(d) is fed from the reflector's side and uses two slots at its end to radiate energy back to the reflector. Fig. A.4(b) and (c) are similar in overall dimensions and principle of operation; however, the E-plane sectoral horn is tapered to obtain the narrowest beamwidth in the E-plane, as its name suggests.

The radiation patterns in the E and H planes for each feed can be seen in Fig. A.5. Fig. A.5(a) shows that the waveguide and rear-fed waveguide options present the broadest patterns in the E-field. However, the rear-fed waveguide, or clutter feed, presents certain ripples. Both feed types present similar gains. The pyramidal horn presents the broadest beam between the two horn options but also has a higher gain. The E-plane sectoral horn produces the narrowest beam in the E-plane. In contrast, in the H-plane, the E-plane sectoral horn beam is the broadest, whereas the other feed characteristics remain proportional to its E-plane counterparts.

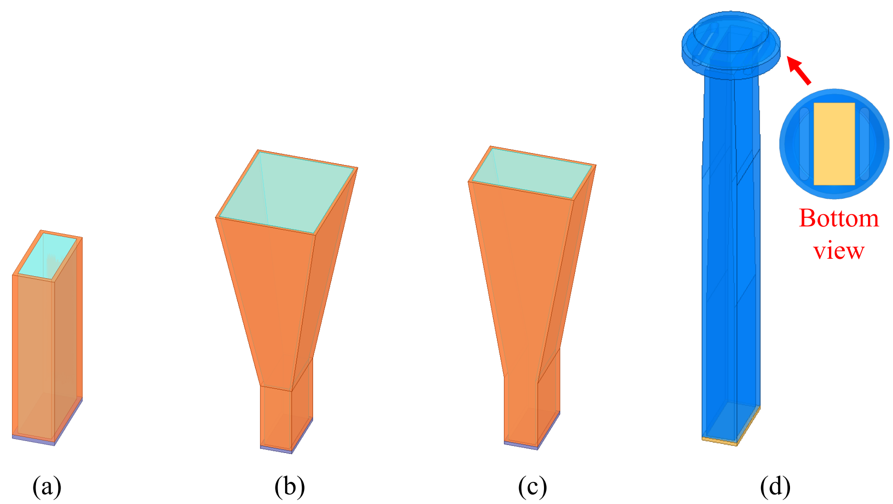

Figure A.4: Reflector antenna feed types: (a) Open-ended WR-90 waveguide, (b) pyramidal horn, (c) E-plane sectoral horn, and (d) rear-fed waveguide, also referred as clutter feed.

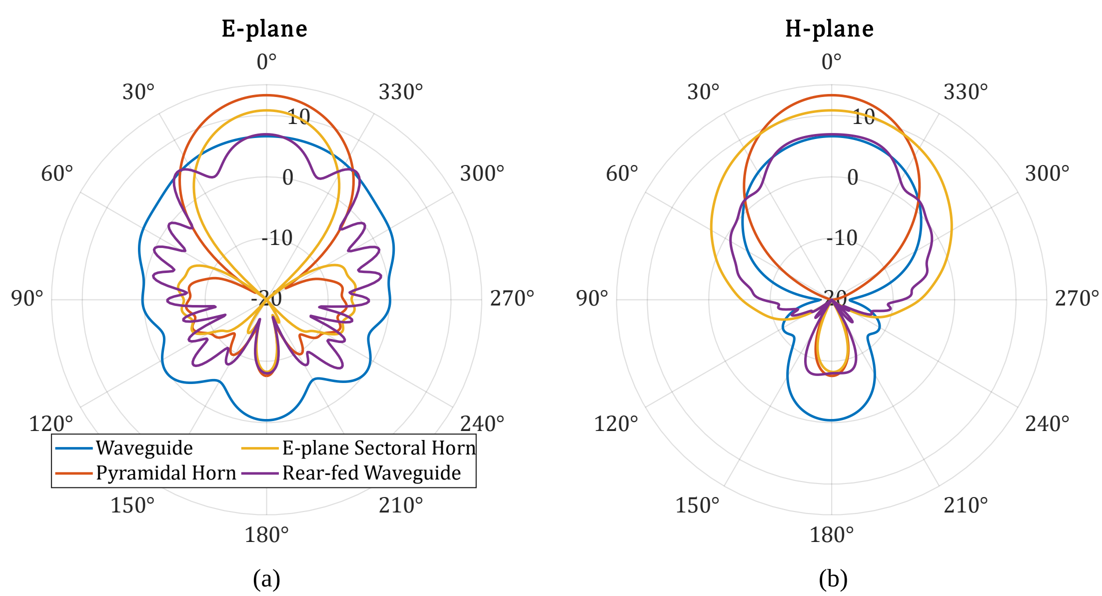

Figure A.5: Radiation patterns for the selected antenna feed types in (a) E-plane and (b) H-plane.

After each feed had been characterized, an HFSS model for a reflector fed by each of these feeds was simulated. Fig. A.6 shows the E- and H-plane cuts for each case. It can be seen that the broader the beamwidth of the feed in a particular plane, the higher the average sidelobe level (SLL_{ave}) will be in that plane. Gain variations are also proportional to the feed gain. Broader feeds also present higher backplane radiation in both planes. An interesting finding was that, due to the ripples present in the rear-fed waveguide feed, the reflector radiation pattern in this case actually presents a narrower beam from the peak to 13 dB lower than that of the E-plane sectoral antenna.

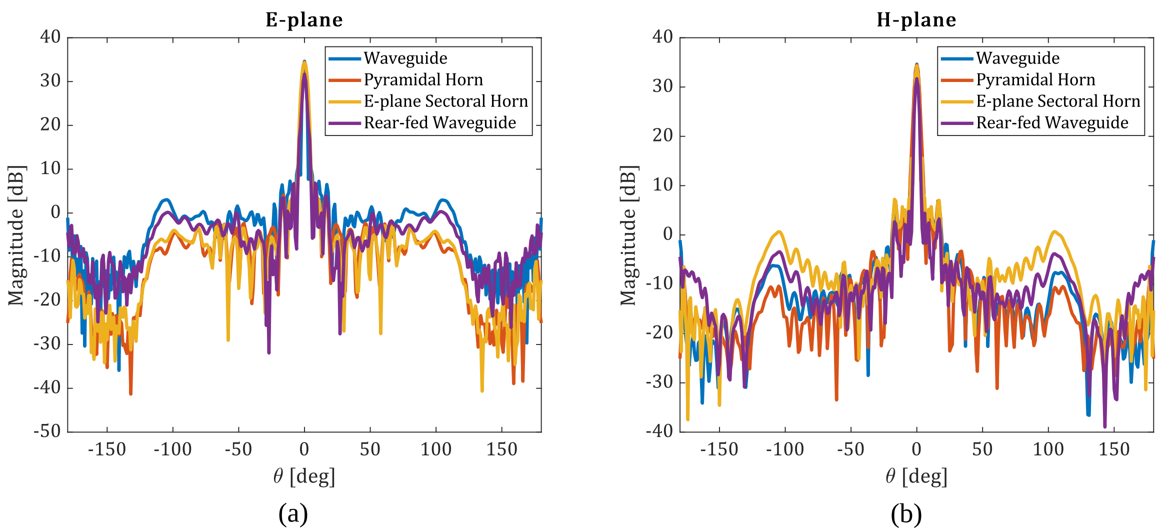

Figure A.6: Radiation pattern comparison for a 0.8m-diameter reflector according to the selected feed types in the (a) E-plane and (b) H-plane cuts.

For the following sections, the performance comparison will primarily be between the E-plane sectoral horn and the rear-fed waveguide (or clutter feed), since they present the best performance among both waveguide and horn cases. Additionally, the feed support structure required for both will be considerably different and will be analyzed in future sections, along with their cross-polarization levels.

A.2.3 Focal Point Analysis

Using the described feed cases, a focal point f_p analysis was performed with a 0.8 m-diameter reflector. The focal point value was varied between 26.5 cm and 36.5 cm. Fig. A.7 shows the radiation pattern in the E-plane cut for both the E-plane sectoral horn and the rear-fed waveguide, according to the focal point.

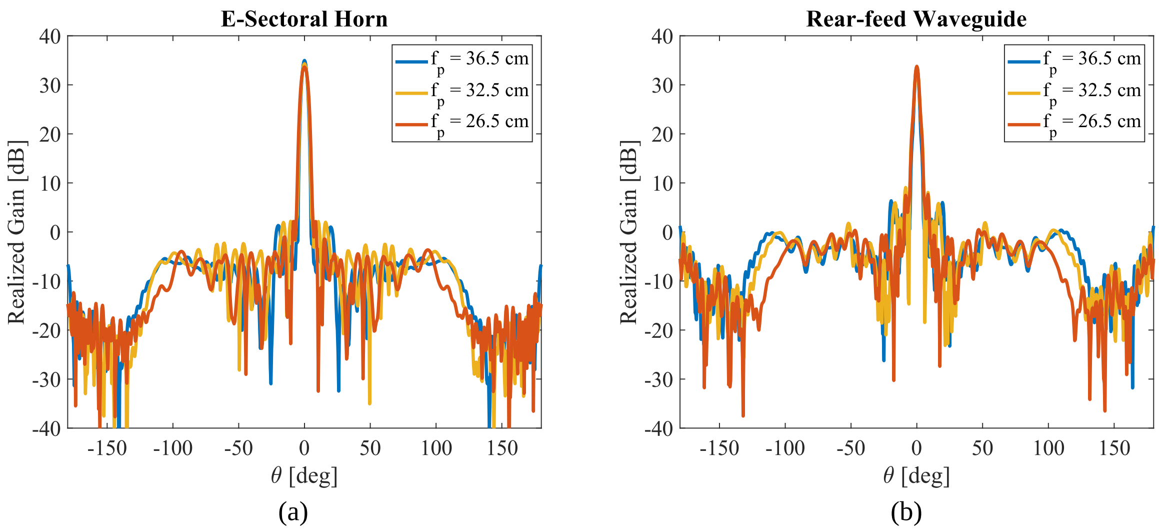

Figure A.7: Radiation patterns in the E-plane cut for a 0.8m-diameter reflector according to focal point f_p for a (a) E-plane sectoral horn feed and a (b) rear-fed waveguide feed.

Smaller focal points result in a higher concentration of reflected energy in both feed cases, reducing backplane radiation and the peak sidelobe level (SLL_{peak}). Nevertheless, smaller focal lengths also require more precise reflector shaping and feed placement. Fig. A.7(a) shows that there is a gain variance for the E-plane sectoral horn case according to the focal length value, which can indicate that the energy is not being focused optimally for this particular feed.

A.3 Sea Clutter Simulation Results

The MATLAB sea clutter simulation used in this section was developed and provided by Brian Stade. The simulation allows for the calculation of sea clutter return power according to wind direction and sea state conditions for a radar transmitting N_p pulses with a particular waveform: rectangular, linear frequency modulation (LFM), and pulse code (PC) modulation. The radar has a maximum observable range, and the return sea clutter power is calculated for a specified antenna radiation pattern, polarization, and elevation angle.

A.3.1 Input Models

The input radiation patterns used for the sea clutter simulation were based on the following models. Both have a 0.8 m-diameter reflector with a 32.5 cm focal point. The E-plane sectoral horn antenna was attached to the reflector surface through a 'buttonhook' support structure. On the other hand, the rear-fed waveguide was attached to the reflector by extending the WR-90 waveguide toward the reflector itself.

The support structures are included to properly assess the cross-polarization levels and to add more detail to the simulation, bringing it closer to the real deployment scenario. Fig. A.8 and Fig. A.9 show both reflector antenna models and their corresponding co-polarization (co-polar) and cross-polarization (cross-polar) 3D radiation patterns, considering vertical polarization. These radiation patterns will be used as inputs for the MATLAB sea clutter simulation. Co-polar patterns are specified as vertical ('V') polarization, whereas the cross-polar patterns are specified as horizontal ('H') polarization.

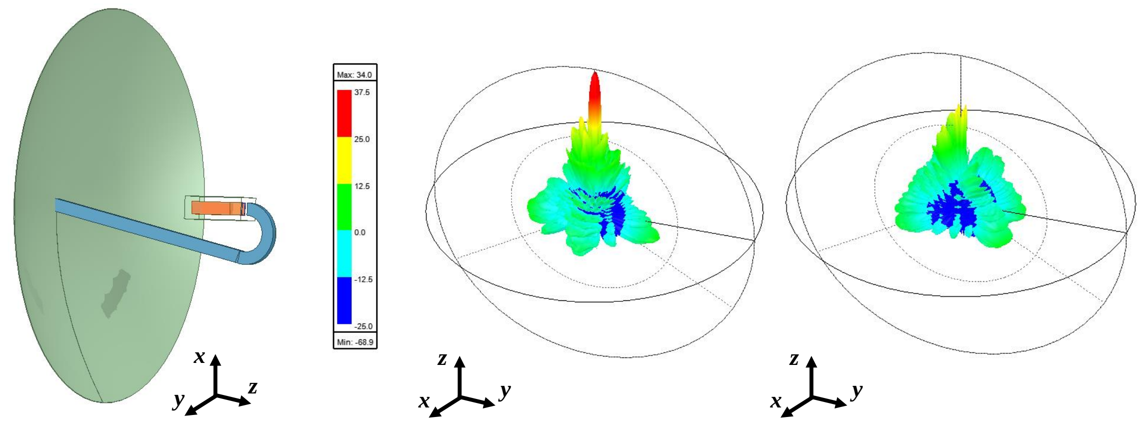

(a) (b) (c)

Figure A.8: Reflector antenna with E-plane sectoral horn feed model with its respective co-polarization and cross-polarization 3D radiation patterns. (a) HFSS model, (b) co-polarization 3D radiation pattern, and (c) cross-polarization 3D radiation pattern.

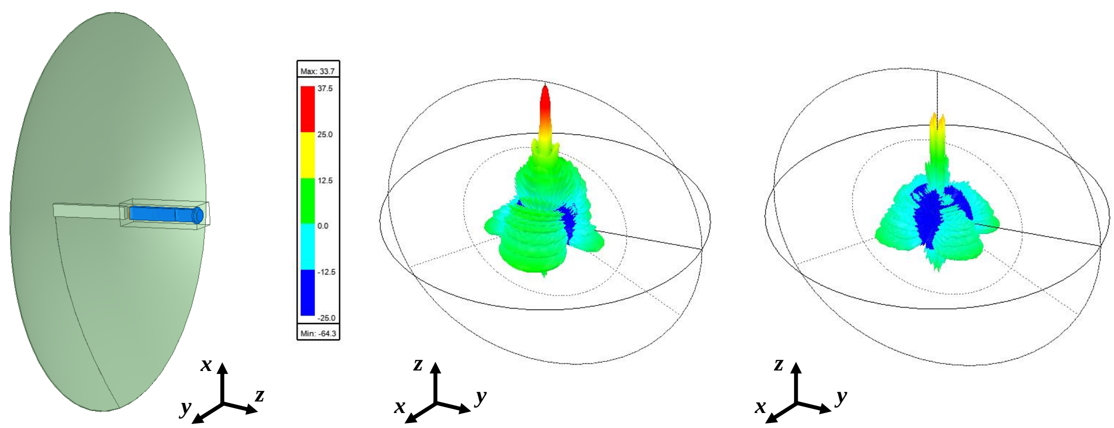

(a) (b) (c)

Figure A.9: Reflector antenna with rear-fed waveguide feed model with its respective co-polarization and cross-polarization 3D radiation patterns. (a) HFSS model, (b) co-polarization 3D radiation pattern, and (c) cross-polarization 3D radiation pattern.

A detailed comparison of both reflector antenna models is presented in Table A.1. Both antennas show similar gain values, with only an approximately 0.3 dB difference in favor of the E-plane sectoral horn antenna feed. Likewise, the sectoral horn feed exhibits lower SLL and a higher front-to-back ratio. However, the clutter feed demonstrates better cross-polarization levels, with a peak cross-pol 4.73 dB lower than the horn feed, and an average cross-pol level 11.75 dB lower.

Table A.1: Selected Reflector Antenna Models Comparison

Variable	**E-plane Sectoral Horn 'Buttonhook'**	**Rear-fed Waveguide 'Cuttler Feed'**
Realized Gain [dB]	34.03	33.70
SLL_{peak} [dB]	-32.93	-26.32
SLL_{ave} [dB]	-38.82	-31.95
Front-to-Back Ratio [dB]	47.37	34.29
Cross-pol Peak [dB]	-41.88	-46.61
Cross-pol Average [dB]	-48.78	-60.53

A.3.2 Range-Doppler Map Results

Range-Doppler maps (RDM) are graphical representations used in radar and communication systems to show the relationship between the range (distance – y-axis) and the Doppler shift (relative velocity – x-axis) of targets. The third dimension of these plots is a color scale that represents the return power in dB.

In this section, range-Doppler maps for sea clutter power returns are presented, considering a radar with a maximum range of 400 m. The sea state and wind direction were both 0. The waveform used was LFM, and a total of 64 N_p pulses were transmitted. Two sets of plots are presented in Fig. A.10 and Fig. A.11, corresponding to the buttonhook and clutter feed options, respectively. Co-polar and cross-polar results are presented for 0° and 10° elevation angles.

Fig. A.10(a) and (c) show that, for a buttonhook feed reflector antenna, the co-polar radiation pattern receives high sea clutter returns, which diminish as the elevation angle increases. For the cross-polar pattern returns shown in Fig. A.10(b) and (d), the trend is the opposite, probably due to the fact that the cross-pol pattern is minimal at the broadside.

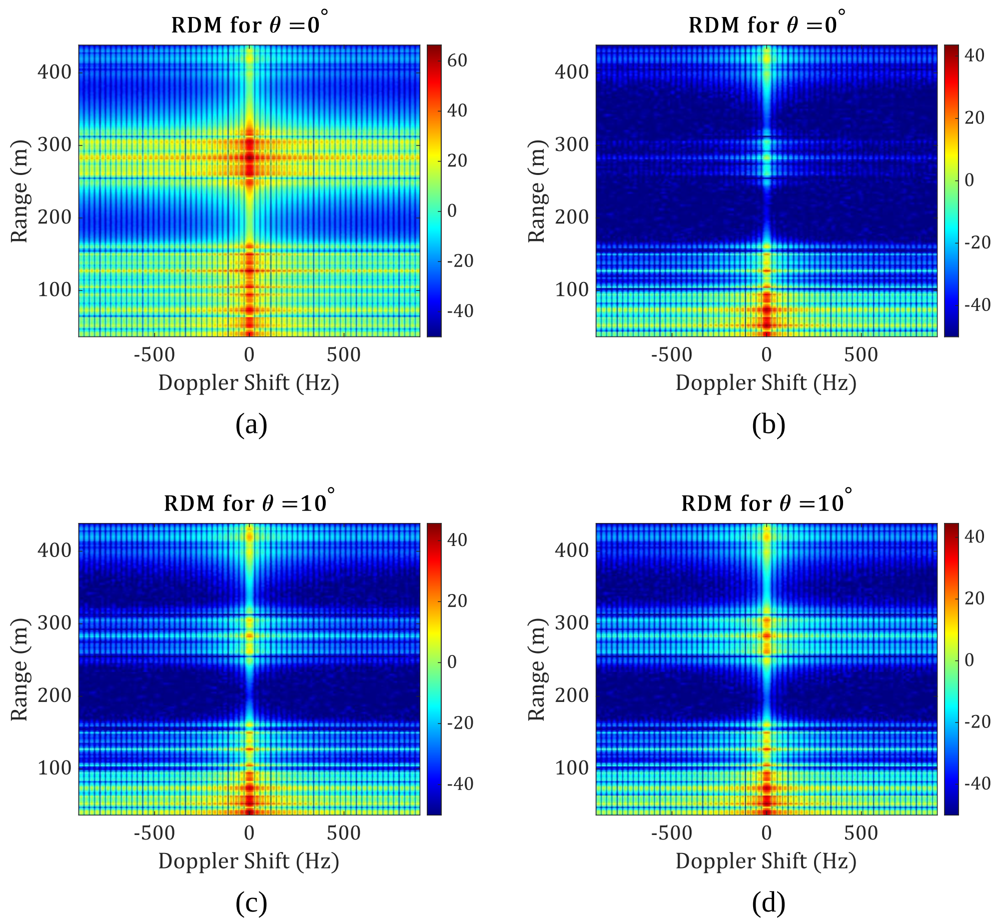

Figure A.10: Rangle-Doppler maps for sea clutter returns considering a buttonhook feed reflector antenna. RDMs for co-polar radiation pattern at (a) 0° and (c) 10° elevation angles. RDMs for cross-polar radiation pattern at (b) 0° and (d) 10° elevation angles.

When comparing the results from the clutter feed presented in Fig. A.11, the co-polar pattern RDMs show that the return power peaks in the same range areas. For instance, at a 0° elevation angle, both cases present high sea clutter return power between 0 and 160 meters, and again at 260 to 310 meters. The same behavior is observed at a 10° elevation angle but with lower power. A peak of return power around 400 meters is also observed.

The cross-polar pattern sea clutter RDMs show similar trends; however, the Cuttler feed case shows significantly lower return power. Considering a target in those ranges, these cross-pol returns might be important, as the color map indicates that they are comparable to the co-polar return power values.

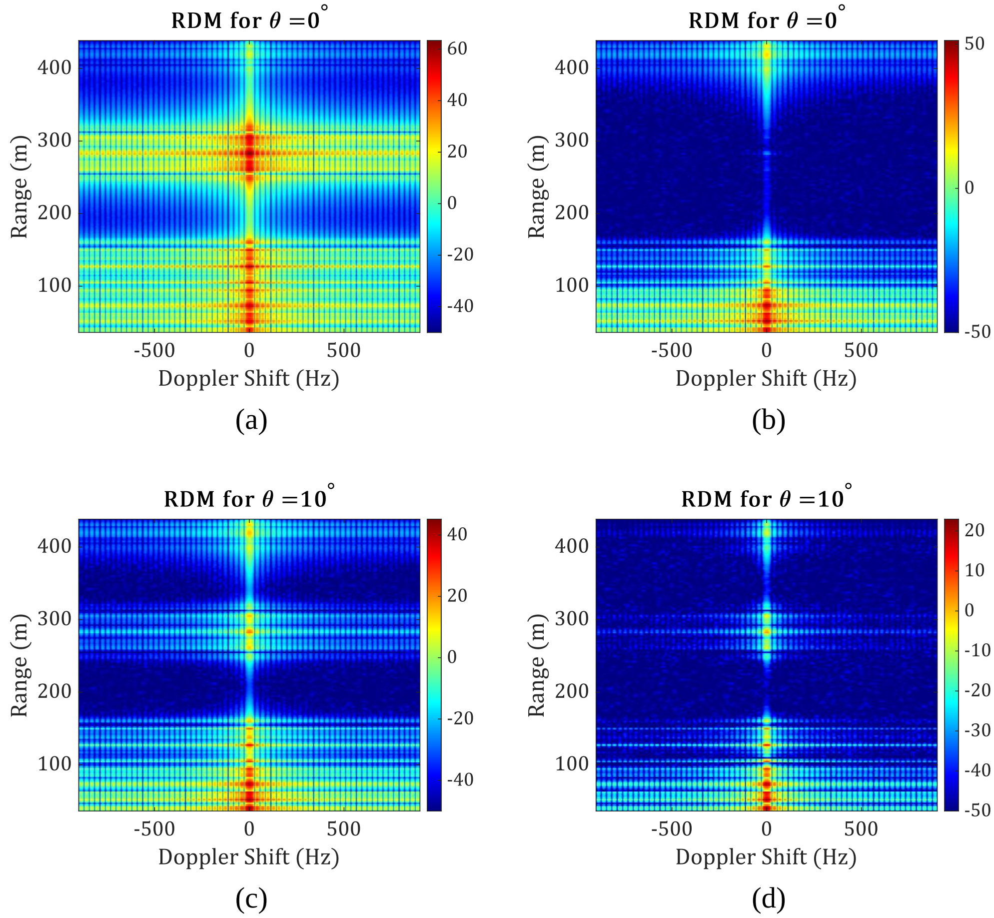

Figure A.11: Rangle-Doppler maps for sea clutter returns considering a cuttler feed reflector antenna. RDMs for co-polar radiation pattern at (a) 0° and (c) 10° elevation angles. RDMs for cross-polar radiation pattern at (b) 0° and (d) 10° elevation angles.

A.4 Conclusions and Future Work

In this work, a detailed analysis of reflector antenna models, including the E-plane sectoral horn and the rear-fed clutter feed, was conducted to evaluate their performance in sea-clutter environments. The study involved simulating radiation patterns, optimizing reflector sizes, and analyzing the impact of feed types, focal points, and support structures on the antenna's performance. Results showed that both feed types presented similar gain values, with the E-plane sectoral horn offering a higher front-to-back ratio and lower sidelobe levels, while the rear-fed feed demonstrated better cross-polarization performance.

Additionally, range-Doppler maps were generated to assess the sea clutter returns, revealing that both co-polar and cross-polar patterns displayed distinct trends with varying elevation angles, with the rear-fed clutter feed showing significantly lower cross-polar return power compared to the sectoral horn. Overall, the findings highlight the trade-offs between performance and structural complexity in choosing the most suitable reflector antenna for sea clutter radar applications, with the rear-fed feed showing advantages in cross-polarization and the sectoral horn in co-polarization.

Future work will focus on further optimizing the reflector antenna design by exploring additional edge treatments, absorber use, and cassegrain feed configurations, analyzing their effect on sea clutter rejection, particularly in environments with varying sea states and wind conditions. An in-depth investigation into the impact of reflector shape and material properties on performance could also provide valuable insights, especially for applications requiring more compact and lightweight antenna solutions.

References

[1] T. A. Milligan, *Modern Antenna Design*. John Wiley Sons, Jul. 2005.

[2] C. A. Balanis, *Antenna Theory: Analysis and Design*. John Wiley Sons, Dec. 2015.

[3] J. D. Díaz, D. Schvartzman, J. L. Salazar-Cerreño, T.-Y. Yu, R. D. Palmer, and M. S. McCord, "Polarimetric Atmospheric Imaging radar (PAIR): Antenna Design, Testing, and Validation," in *2022 IEEE Radar Conference (RadarConf22)*, Mar. 2022, p. 1–5. [Online]. Available: https://ieeexplore.ieee.org/document/9763907

[4] P. Dhande, "Antennas and its Applications," *DRDO Science Spectrum*, pp. 66–78, 2009.

[5] B. Farhang-Boroujeny, H. Moradi, and T. V. Holschuh, "Filter Bank UWB Communications," *IEEE Communications Magazine*, vol. 62, no. 1, p. 120–125, Jan. 2024.

[6] P. S. Hall, P. Gardner, and A. Faraone, "Antenna Requirements for Software Defined and Cognitive Radios," *Proceedings of the IEEE*, vol. 100, no. 7, p. 2262–2270, Jul. 2012.

[7] M. Feng, S.-C. Shen, D. Caruth, and J.-J. Huang, "Device technologies for RF front-end circuits in next-generation wireless communications," *Proceedings of the IEEE*, vol. 92, no. 2, p. 354–375, Feb. 2004.

[8] A. Iqbal, J. J. Tiang, S. K. Wong, M. Alibakhshikenari, F. Falcone, and E. Limiti, "Miniaturization Trends in Substrate Integrated Waveguide (SIW) Filters: A Review," *IEEE Access*, vol. 8, p. 223287–223305, 2020.

[9] J. Liner, "SWaP: The RF Solution That Can Mean the Difference Between Flying High and Being Grounded," 2015, accessed on July 29, 2024. [Online]. Available: https://www.analog.com/en/resources/technical-articles/swap-the-rf-solution.html

[10] K. H. Jones and J. N. Gross, “Reducing Size, Weight, and Power (SWaP) of Perception Systems in Small Autonomous Aerial Systems,” in *14th AIAA Aviation Technology, Integration, and Operations Conference*. Atlanta, GA: American Institute of Aeronautics and Astronautics, Jun. 2014. [Online]. Available: https://arc.aiaa.org/doi/10.2514/6.2014-2705

[11] J. H. Reed, J. T. Bernhard, and J.-M. Park, “Spectrum Access Technologies: The Past, the Present, and the Future,” *Proceedings of the IEEE*, vol. 100, no. Special Centennial Issue, p. 1676–1684, May 2012.

[12] M. Song, C. Xin, Y. Zhao, and X. Cheng, “Dynamic Spectrum Access: from Cognitive Radio to Network Radio,” *IEEE Wireless Communications*, vol. 19, no. 1, p. 23–29, Feb. 2012.

[13] S. Bhattarai, J.-M. J. Park, B. Gao, K. Bian, and W. Lehr, “An Overview of Dynamic Spectrum Sharing: Ongoing Initiatives, Challenges, and a Roadmap for Future Research,” *IEEE Transactions on Cognitive Communications and Networking*, vol. 2, no. 2, p. 110–128, Jun. 2016.

[14] Q. Zhao and B. M. Sadler, “A Survey of Dynamic Spectrum Access,” *IEEE Signal Processing Magazine*, vol. 24, no. 3, p. 79–89, May 2007.

[15] H. Arslan, *Cognitive Radio, Software Defined Radio, and Adaptive Wireless Systems*, 1st ed., ser. Signals and Communication Technology, Dordrecht, 2007.

[16] F. C. Commission, “3.5 ghz band overview,” Apr. 2024. [Online]. Available: https://www.fcc.gov/wireless/bureau-divisions/mobility-division/35-ghz-band/35-ghz-band-overview

[17] Y. Tawk, J. Costantine, and C. G. Christodoulou, “Reconfigurable Filtennas and MIMO in Cognitive Radio Applications,” *IEEE Transactions on Antennas and Propagation*, vol. 62, no. 3, p. 1074–1083, Mar. 2014.

[18] A. Kantemur, J. Tak, P. Siyari, A. H. Abdelrahman, M. Krunz, and H. Xin, “A Novel Compact Reconfigurable Broadband Antenna for Cognitive Radio Applications,” *IEEE Transactions on Antennas and Propagation*, vol. 68, no. 9, p. 6538–6547, Sep. 2020.

[19] A. A. Ibrahim, H. A. Mohamed, A. R. D. Rizo, R. Parra-Michel, and H. Aboushady, "Tunable Filtenna With DGS Loaded Resonators for a Cognitive Radio System Based on an SDR Transceiver," *IEEE Access*, vol. 10, p. 32123–32131, 2022.

[20] S. Henthorn, K. L. Ford, and T. O'Farrell, "A system-level performance evaluation of a reconfigurable filtenna in the presence of in- and out-of-band blockers," *IET Communications*, vol. 16, no. 20, p. 2492–2500, 2022.

[21] R. Agasti, E. Kim, J. Ruyle, C. C. Onwuchekwa, S. Azizi, and M. Rahaim, "Implementation of Software-Defined Antenna and Radio Test System for Congested Spectral Environments," 2023.

[22] J. Costantine, Y. Tawk, S. E. Barbin, and C. G. Christodoulou, "Reconfigurable Antennas: Design and Applications," *Proceedings of the IEEE*, vol. 103, no. 3, p. 424–437, Mar. 2015.

[23] J. Kumar and P. Ranjan, "An overview of reconfigurable dielectric resonator antenna-based cognitive radio energy harvesting for wireless communication," https://www.microwavejournal.com/articles/41604-an-overview-of-reconfigurable-dielectric-resonator-antenna-based-cognitive-radio-energy-harvesting-for-wireless-communication, Mar. 2024.

[24] C. G. Christodoulou, Y. Tawk, S. A. Lane, and S. R. Erwin, "Reconfigurable Antennas for Wireless and Space Applications," *Proceedings of the IEEE*, vol. 100, no. 7, p. 2250–2261, Jul. 2012.

[25] N. Ojaroudi Parchin, H. Jahanbakhsh Basherlou, Y. I. A. Al-Yasir, A. M. Abdulkhaleq, and R. A. Abd-Alhameed, "Reconfigurable Antennas: Switching Techniques—A Survey," *Electronics*, vol. 9, no. 22, p. 336, Feb. 2020.

[26] B. A. Cetiner, G. Roqueta Crusats, L. Jofre, and N. Biyikli, "Rf mems integrated frequency reconfigurable annular slot antenna," *IEEE Transactions on Antennas and Propagation*, vol. 58, no. 3, p. 626–632, Mar. 2010.

[27] S. Goel and N. Gupta, "Design, optimization and analysis of reconfigurable antenna using rf mems switch," *Microsystem Technologies*, vol. 26, no. 9, p. 2829–2837, Sep. 2020.

[28] R. Alhamad, E. Almajali, and S. Mahmoud, "Electrical reconfigurability in modern 4g, 4g/5g and 5g antennas: A critical review of polarization and frequency reconfigurable designs," *IEEE Access*, vol. 11, p. 29215–29233, 2023.

[29] Y. I. Abdulraheem, G. A. Oguntala, A. S. Abdullah, H. J. Mohammed, R. A. Ali, R. A. Abd-Alhameed, and J. M. Noras, "Design of frequency reconfigurable multiband compact antenna using two pin diodes for wlan/wimax applications," *IET Microwaves, Antennas Propagation*, vol. 11, no. 8, p. 1098–1105, 2017.

[30] Y. Tawk, J. Costantine, and C. G. Christodoulou, "Reconfiguring the frequency and directive behavior of a printed v–shaped structure," *IEEE Transactions on Antennas and Propagation*, vol. 65, no. 5, p. 2655–2660, May 2017.

[31] Y. Tawk, J. Constantine, and C. G. Christodoulou, "A varactor-based reconfigurable filtenna," *IEEE Antennas and Wireless Propagation Letters*, vol. 11, p. 716–719, 2012.

[32] Y. Tawk, J. Costantine, S. Hemmady, G. Balakrishnan, K. Avery, and C. G. Christodoulou, "Demonstration of a cognitive radio front end using an optically pumped reconfigurable antenna system (opras)," *IEEE Transactions on Antennas and Propagation*, vol. 60, no. 2, p. 1075–1083, Feb. 2012.

[33] R. Agasti, "Frequency-agile filtering antennas for s-band and x-band applications," May 2023, accepted: 2023-05-16T14:52:03Z. [Online]. Available: https://shareok.org/handle/11244/337698

[34] I. T. McMichael, "A mechanically reconfigurable patch antenna with polarization diversity," *IEEE Antennas and Wireless Propagation Letters*, vol. 17, no. 7, p. 1186–1189, Jul. 2018.

[35] H. Pablo Zapata Cano, Z. D. Zaharis, T. V. Yioultsis, N. V. Kantartzis, and P. I. Lazaridis, "Pattern reconfigurable antennas at millimeter-wave frequencies: A comprehensive survey," *IEEE Access*, vol. 10, p. 83029–83042, 2022.

[36] A. C. Polycarpou, M. A. Christou, and N. C. Papanicolaou, "Tunable patch antenna printed on a biased nematic liquid crystal cell," *IEEE Transactions on Antennas and Propagation*, vol. 62, no. 10, p. 4980–4987, Oct. 2014.

[37] P. P. Shome, T. Khan, S. K. Koul, and Y. M. Antar, “Filtenna designs for radio-frequency front-end systems: A structural-oriented review,” *IEEE Antennas and Propagation Magazine*, vol. 63, no. 5, p. 72–84, Oct. 2021.

[38] C. X. Mao, Y. Zhang, X. Y. Zhang, P. Xiao, Y. Wang, and S. Gao, “Filtering antennas: Design methods and recent developments,” *IEEE Microwave Magazine*, vol. 22, no. 11, p. 52–63, Nov. 2021.

[39] G. Mansour, M. J. Lancaster, P. S. Hall, P. Gardner, and E. Nugoolcharoenlap, “Design of Filtering Microstrip Antenna Using Filter Synthesis Approach,” *Progress In Electromagnetics Research*, vol. 145, p. 59–67, 2014.

[40] Q. Wu, L. Zhu, and X. Zhang, “Filtering patch antenna on λ/4-resonator filtering topology: synthesis design and implementation,” *IET Microwaves, Antennas Propagation*, vol. 11, no. 15, p. 2241–2246, 2017.

[41] T. L. Wu, Y. M. Pan, P. F. Hu, and S. Y. Zheng, “Design of a low profile and compact omnidirectional filtering patch antenna,” *IEEE Access*, vol. 5, p. 1083–1089, 2017.

[42] J. Gavan and M. Shulman, “Effects of densensitization on mobile radio system performance, part i: Qualitative analysis,” *Vehicular Technology, IEEE Transactions on*, vol. 33, p. 285–290, Dec. 1984.

[43] B. A. Culver, *Modern Co-Site RF Interference Issues and Mitigation Techniques*, 2016.

[44] R. Akeela and B. Dezfouli, “Software-defined Radios: Architecture, state-of-the-art, and challenges,” vol. 128, p. 106–125, Sep. 2018.

[45] F. K. Jondral, “Software-Defined Radio—Basics and Evolution to Cognitive Radio,” *EURASIP Journal on Wireless Communications and Networking*, vol. 2005, no. 3, p. 652784, Aug. 2005.

[46] N. Vun and A. Premkumar, “Adc systems for sdr digital front-end,” in *Proceedings of the Ninth International Symposium on Consumer Electronics, 2005. (ISCE 2005).*, Jun. 2005, p. 359–363. [Online]. Available: https://ieeexplore.ieee.org/document/1502403

[47] N. Instruments, “Advantages of direct rf sampling architectures,” Sep. 2024. [Online]. Available: https://www.ni.com/en/solutions/aerospace-defense/radar-electronic-warfare-sigint/advantages-of-direct-rf-sampling-architectures.html

[48] T. Neu, “Direct rf conversion: From vision to reality,” 2015.

[49] K. Tan, J. Zhang, J. Fang, H. Liu, Y. Ye, S. Wang, Y. Zhang, H. Wu, W. Wang, and G. M. Voelker, “Sora: High performance software radio using general purpose multi-core processors,” in *USENIX NSDI’09*. USENIX, Apr. 2009. [Online]. Available: https://www.microsoft.com/en-us/research/publication/sora-high-performance-software-radio-using-general-purpose-multi-core-processors-best-paper-award/

[50] N. Instruments, “Ni ettus usrp software defined radios,” 2023. [Online]. Available: https://www.ni.com/pdf/product-flyers/usrp-software-defined-radio.pdf

[51] T. Instruments, “Tms320c6670: Multicore fixed and floating-point system-on-chip,” 2012. [Online]. Available: https://www.ti.com/lit/ds/symlink/tms320c6670.pdf?ts=1733085148489&ref_url=https%253A%252F%252Fwww.ti.com%252Fproduct%252FTMS320C6670

[52] M. C. Ng, K. E. Fleming, M. Vutukuru, S. Gross, Arvind, and H. Balakrishnan, “Airblue: A system for cross-layer wireless protocol development,” in *2010 ACM/IEEE Symposium on Architectures for Networking and Communications Systems (ANCS)*, Oct. 2010, p. 1–11. [Online]. Available: https://ieeexplore.ieee.org/document/5623848

[53] A. M. Devices, “Zynq 7000 soc.” [Online]. Available: https://www.xilinx.com/products/boards-and-kits/device-family/nav-zynq-7000.html

[54] S. Popescu, A. Gontean, and D. Ianchis, “Qpsk modulator on fpga,” in *2011 IEEE 9th International Symposium on Intelligent Systems and Informatics*, Sep. 2011, p. 359–364. [Online]. Available: https://ieeexplore.ieee.org/abstract/document/6034353

[55] M. N. Chowdhury, M. R. Ullah Mahfuz, S. H. Chowdhury, and M. M. Kabir, “Design of an improved qpsk modulation technique in wireless communication systems,” in *2017 3rd International Conference on Electrical Information and Communication Technology (EICT)*, Dec. 2017, p. 1–6. [Online]. Available: https://ieeexplore.ieee.org/abstract/document/8275196

[56] F. Xiong, *Digital modulation techniques*, ser. Artech House. Boston, Mass.: Artech House, 2000.

[57] L. Camuñas-Mesa and J. Rosa, "Combining software-defined radio learning modules and neural networks for teaching communication systems courses," *Information*, vol. 14, p. 599, Nov. 2023.

[58] L. Litwin and M. Pugel, "The principles of ofdm," *RF Signal Processing*, Jan. 2001. [Online]. Available: https://citeseerx.ist.psu.edu/document?repid=rep1&type=pdf&doi=219c68521dc18995db46c8e68f689fa11a24c489

[59] K. Technologies, "Concepts of orthogonal frequency division multiplexing (ofdm) and 802.11 wlan." [Online]. Available: https://helpfiles.keysight.com/csg/89600B/Webhelp/Subsystems/wlan-ofdm/content/ofdm_basicprinciplesoverview.htm

[60] Mini-Circuits, "The basics of orthogonal frequency-division multiplexing (ofdm)," Feb. 2024. [Online]. Available: https://blog.minicircuits.com/the-basics-of-orthogonal-frequency-division-multiplexing-ofdm/

[61] P. Banelli, S. Buzzi, G. Colavolpe, A. Modenini, F. Rusek, and A. Ugolini, "Modulation formats and waveforms for 5g networks: Who will be the heir of ofdm?: An overview of alternative modulation schemes for improved spectral efficiency," *IEEE Signal Processing Magazine*, vol. 31, no. 6, p. 80–93, Nov. 2014.

[62] "Top kpis to measure for optimal wireless network performance." [Online]. Available: https://wlanprofessionals.com/top-kpis-to-measure-for-optimal-wireless-network-performance/

[63] D. H. Johnson, "Signal-to-noise ratio," *Scholarpedia*, vol. 1, no. 12, p. 2088, Dec. 2006.

[64] V. Petrov, D. Moltchanov, and Y. Koucheryavy, "Interference and sinr in dense terahertz networks," in *2015 IEEE 82nd Vehicular Technology Conference (VTC2015-Fall)*, Sep. 2015, p. 1–5. [Online]. Available: https://ieeexplore.ieee.org/abstract/document/7390991

[65] I. International, "What is sinr (signal to interference noise ratio)?" [Online]. Available: https://iscointl.com/sinr-optimization/

[66] M. Pundir and J. K. Sandhu, "A systematic review of quality of service in wireless sensor networks using machine learning: Recent trend and future vision," *Journal of Network and Computer Applications*, vol. 188, p. 103084, Aug. 2021.

[67] EttusResearch, "USRP Hardware Driver and USRP Manual: General Application Notes." [Online]. Available: https://files.ettus.com/manual_archive/v3.15.0.0/html/page_general.html

[68] F. C. Commission, "Wireless communications service (wcs)." [Online]. Available: https://www.fcc.gov/wireless/bureau-divisions/mobility-division/wireless-communications-service-wcs

[69] B. Bencivenga and L. Scialacqua, "2-32 GHz dual ridge horn Satimo test report," 2011.

[70] L. Hai, "Molex LTE GNSS antenna hinged application specification," 2021.

[71] everythingRF, "150-441EM-NF," accessed on July 21, 2024. [Online]. Available: https://www.everythingrf.com/products/waveguide-horn-antennas/atm-inc/617-249-150-441em-nf

[72] R. Agasti, C. G. Blosser, J. E. Ruyle, and H. H. Sigmarsson, "Tunable siw-based evanescent-mode cavity-backed slot antenna with contactless tuning," *IEEE Access*, vol. 11, p. 42670–42678, 2023.

[73] R. Agasti, A. Bauer, J. E. Ruyle, and H. H. Sigmarsson, "Frequency-agile siw-based filtenna using evanescent-mode cavity resonators," *IEEE Antennas and Wireless Propagation Letters*, vol. 22, no. 10, p. 2600–2604, Oct. 2023.

[74] N. Technologies, "M3-l linear actuator," 2023. [Online]. Available: https://www.newscaletech.com/wp-content/uploads/M3-L_datasheet.pdf

[75] ——, "New Scale Pathway Software Guide," 2021. [Online]. Available: https://www.newscaletech.com/wp-content/uploads/cad/Newscale_PathwaySoftwareManual.pdf

[76] EttusResearch, "USRP B200/B210 Bus Series." [Online]. Available: https://www.ettus.com/wp-content/uploads/2019/01/b200-b210_spec_sheet.pdf

[77] ——, "USRP X300 and X310 X Series." [Online]. Available: https://www.ettus.com/wp-content/uploads/2024/01/X300_X310_Spec_Sheet_2024-01-23.pdf

[78] [Online]. Available: https://www.lenovo.com/us/outletus/en/p/laptops/thinkpad/thinkpadp/thinkpad-p16-16-inch-intel/21d6007xus

[79] E. Blossom, "GNU Radio: Tools for Exploring the Radio Frequency Spectrum," 2004, accessed on July 22, 2024. [Online]. Available: https://www.linuxjournal.com/article/7319

[80] "Xmlrpc server," 2021. [Online]. Available: https://wiki.gnuradio.org/index.php/XMLRPC_Server

[81] "Understanding zmq blocks." [Online]. Available: https://wiki.gnuradio.org/index.php/Understanding_ZMQ_Blocks

[82] T. Renk, C. Kloeck, C. Koerner, and F. K. Jondral, "Increasing spectral efficiency by managing adjacent channel interference," in *Proceedings of the first international workshop on Technology and policy for accessing spectrum - TAPAS '06*. Boston, Massachusetts: ACM Press, 2006, pp. 16–es. [Online]. Available: http://portal.acm.org/citation.cfm?doid=1234388.1234404

[83] J. Becker and J.-C. Sureau, "Control of radar site environment by use of fences," *IEEE Transactions on Antennas and Propagation*, vol. 14, no. 6, p. 768–773, Nov. 1966.

[84] V. Gregers-Hansen and R. Mital, "An improved empirical model for radar sea clutter reflectivity," *IEEE Transactions on Aerospace and Electronic Systems*, vol. 48, no. 4, p. 3512–3524, Oct. 2012.

[85] F. Nathanson, J. Reilly, and M. Cohen, *Radar Design Principles: Signal Processing and the Environment*, ser. The SciTech radar and defense series. SciTech Publishing, Incorporated, 1999. [Online]. Available: https://books.google.com/books?id=9IKI0egWkPgC

[86] S. Watts, "Modeling and simulation of coherent sea clutter," *IEEE Transactions on Aerospace and Electronic Systems*, vol. 48, no. 4, p. 3303–3317, Oct. 2012.

[87] Y. Rahmat-Samii and R. Haupt, "Reflector antenna developments: A perspective on the past, present and future," vol. 57, p. 85–95, Apr. 2015.